Universitat
de les Illes Balears

Characterization of the Hough all-sky search for continuous gravitational wave signals using LIGO data

Pep Blai Covas Vidal

Master's Thesis

Master's degree in Physics
(With a specialty/Itinerary in Astrophysics and Relativity)

at the

UNIVERSITAT DE LES ILLES BALEARS

Academic year 2015-16

Date: September, 2016

Author signature Pep Blai

UIB Master's Thesis Supervisor: Dra. Alicia M. Sintes Olives

Supervisor signature Alicia M. Sintes

ABSTRACT

For the first time, scientists have observed ripples in the fabric of space-time called gravitational waves, arriving at Earth from a cataclysmic event in the distant Universe. These gravitational waves were detected on September 14, 2015 at 9:51 a.m. UTC by both of the twin Laser Interferometer Gravitational-wave Observatory (LIGO) detectors. This confirms a major prediction of Albert Einstein's 1915 theory of general relativity and opens an unprecedented new window onto the cosmos.

Isolated spinning neutron stars in our galaxy are also among the targets of the ground-based interferometric gravitational wave detectors. If these stars are not perfectly symmetric about their axis of rotation, e.g. if they have a "mountain" on their surface, they are expected to emit continuous gravitational waves (CW). This thesis is devoted to the characterization of a search method for continuous gravitational wave signals from unknown sources - neutron stars that do not beam a radio signal in Earth's direction - using the Hough transform.

Unlike searches for gravitational waves from pulsars (whose locations, gravitational wave emission frequencies, and spin-down rates are well known), searches for electromagnetically quiet sources require algorithms which look at vastly larger parameter spaces: all sky directions, all frequencies, and all spin-down rates. In addition, the algorithms have to account for "rapid" modulation of the signal due to Earth's rotation (both Doppler modulation of the frequency and amplitude modulation due to the diurnal change in detector antenna pattern) and the slower modulation due to Earth's orbit around the sun. Unfortunately, this is a computationally intractable problem: there is not enough computing power available to search such a large and essentially continuous parameter space in sky position, frequency, and spin-down rate as well as in gravitational wave polarization. Using optimal search methods, the UIB Relativity and Gravitation group efforts focus on making all-sky CW searches computationally manageable, that is on the development of effective computational methods using limited computing power by taking a first pass at the data using computationally inexpensive methods, for identifying interesting candidates or regions in parameter space and then performing follow-up searches

with much more precise (and computationally expensive) methods over a much more restricted region. Although other methods exist, the UIB group has devised a clever technique based on the Hough transform that partially immunizes the computationally cheap search against instrumental artefacts that naturally pollute the experimental interferometer data. These methods have served as the basis for a number of continuous wave searches during initial LIGO.

Currently I am involved in a number of refinements using this Hough transform method that will allow to follow weaker signals without increasing the computational cost, and I have contributed to the Continuous Wave Mock Data Challenge - a chance to explore the capabilities of the search algorithms within the LIGO-Virgo Continuous Wave working group - as well as to the analysis of Advanced LIGO O1 data.

ACKNOWLEDGEMENTS

First of all, I would like to thank my thesis director Dra. Alicia Sintes. She has given me the opportunity to work with the Relativity and Gravitation group, and to be a member of the LIGO Scientific Collaboration, starting my journey into the scientific research world. She has taught me a lot of things about gravitational waves, statistics, writing and organising a scientific thesis, and many other subjects. She has also been very patient and helpful with all my questions during these two years of work and collaboration. I also want to thank Dr. Sascha Husa, for helping me with computer issues anytime and for teaching me lots of interesting physics.

Secondly, many thanks to Alfred and Rafel for the laughs and company of all the year. This year would been much boring without the two of you. Also, thanks to the other LIGO@UIB members for answering questions any time and being so kind.

Lastly, I want to say thanks to my family, for always supporting me and my career choices. I wouldn't be here without you.

LIST OF ABBREVIATIONS

CBC	Compact binary coalescence
CW	Continuous wave
ET	Einstein Telescope
GW	Gravitational wave
H1	LIGO Hanford 4 km interferometer
L1	LIGO Livingston 4 km interferometer
LIGO	Laser Interferometer Gravitational-wave Observatory
LSC	LIGO Scientific Collaboration
MC	Monte Carlo
MDC	Mock Data Challenge
O1	First Advanced LIGO science run
PSD	Power Spectral Density
S6	Initial LIGO science run 6
SFT	Short Fourier Transform
SNR	Signal to Noise Ratio
STD	Standard deviation

CONTENTS

Part I

Theoretical introduction

The first three chapters of the thesis are a general introduction. The first chapter describes gravitational waves, with a mathematical approximation of general relativity called linearized theory of general relativity. It also contains a summary of the current state of interferometric detectors and how they work. The second chapter gives an introduction to neutron stars and describes mathematically the continuous gravitational wave signals. It also discusses different types of searches for continuous waves. The third chapter describes the mathematical foundation of the Hough transform, and it explains its statistics and the constraints of the different parameters of the search.

CHAPTER 1

INTRODUCTION

In 1905, Einstein published his theory of special relativity [1]. In this theory, phenomenons like time dilation or conversion of mass into energy were explained. The two main principles of special relativity are:

- **Principle of relativity**: the results of any experiment performed by any observer do not depend on his speed relative to other observers who are not involved in the experiment.
- **Universality of the speed of light**: the speed of light in vacuum it's always equal to $c = 3 \times 10^8$ m/s, regardless of the motion of the light's source relative to the observer.

Ten years later, in 1915, Einstein published the theory of general relativity [2]. Special relativity did not take into account frames of reference with acceleration, so a generalisation of that theory had to be made. General relativity explains the interaction between energy distributions and the curvature of space-time, and it is a description of gravity as a geometric property of spacetime. The equation that explains this interaction is:

$$G_{\mu\nu} = \frac{8\pi G}{c^4} T_{\mu\nu}, \tag{1.1}$$

where $G_{\mu\nu}$ is the Einstein tensor, $T_{\mu\nu}$ is the stress-energy tensor, G is the gravitational constant (6.674×10^{-11} N·m^2/kg^2) and c is the speed of light in vacuum.

One year after the publication of the theory of general relativity (1916), Einstein published a paper describing what he called **gravitational waves** (GWs) [3].

Until a few months ago, the only indirect evidence of the existence of GWs was due to the observed inspiral of the binary pulsar PSR 1913+16, discovered by Hulse and Taylor in 1975 [4]. They showed that the binary neutron star system was spiralling inwards at the rate predicted by general relativity. The 14th of September 2015, the first direct detection of gravitational waves was made: waves coming from a binary black hole merger were detected [5]. Again, the 26th of

December 2015, another direct detection of gravitational waves from a binary black hole merger with lower masses was made. These two detections mark the beginning of gravitational wave astronomy, a completely new way to explore and understand the Universe.

In this chapter we will introduce the mathematical foundation of gravitational waves. Besides, we will describe the current state of gravitational wave detectors and how they work. We will also describe the different types of sources that can produce gravitational waves.

1.1 | Gravitational waves

Gravitational waves are "ripples" (perturbations) in the fabric of space-time caused by some of the most violent and energetic processes in the Universe. When any energy distribution that has an asymmetry is accelerated, the curvature of space-time is changed, and this change is emitted from the source in form of gravitational radiation. According to special relativity, this change cannot be felt instantaneously: it must propagate at a finite speed. In general relativity, this propagation travels at the speed of light, and it's called a gravitational wave. These GWs are vibrations of the space-time itself that are transported, in contrast with the electromagnetic waves which are vibrations being transported in the space-time. There are more differences with electromagnetic waves, and some similarities too, which are shown in table 1.1.

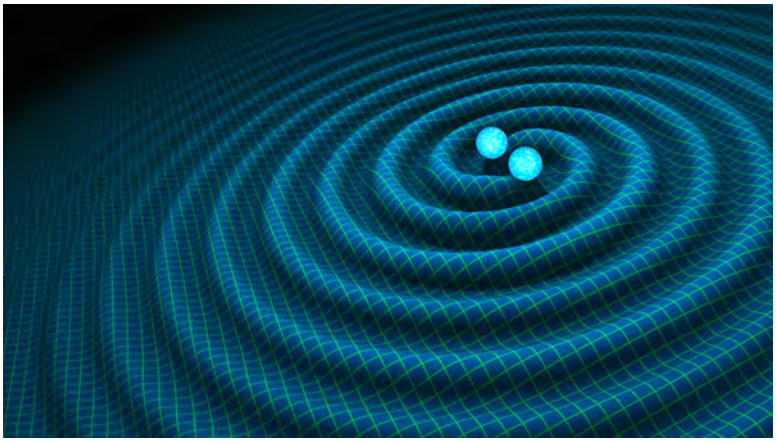

Fig. 1.1: Artistic impression of gravitational waves produced by an inspiralling binary system. Source: NASA.

Gravitational waves have an extremely small amplitude. This is related to the fact that gravitational interaction is the weakest of all known interactions. For this reason, we only expect to detect gravitational waves coming from the most violent and catastrophic events in the Universe: mergers of black holes or neutron stars, isolated spinning neutron stars, supernova explosions, etc. Figure 1.1 shows an artistic impression of gravitational waves coming from an inspiralling binary system.

Gravitational waves	**Electromagnetic waves**
Oscillations of space-time	Oscillations propagated through space-time
1 mass sign	2 charge signs
2 polarization states rotated by 45°	2 polarization states rotated by 90°
Direct detectable frequencies: $\sim 10^{-9}$ - 10^{11} Hz	Frequencies: $\sim 10^{4}$ - 10^{20} Hz
Hardly interact with matter	Strongly interact with matter
Propagate at speed of light	Propagate at speed of light
Amplitude decays with distance as $\propto 1/d$	Amplitude decays with distance as $\propto 1/d$

Table 1.1: Comparison between gravitational and electromagnetic waves.

Most of the sources of gravitational waves are located very far away from us. For this reason, a weak field approximation can be used to mathematically describe the propagation and detection of GWs. There are different mathematical descriptions of the weak field approximation, like:

- Small perturbations of a smooth, time-independent background metric.
- Post-Newtonian theory.
- Linearized theory.

We are going to use linearized theory to describe the propagation of gravitational waves.

1.1.1 | Linearized theory of general relativity

Linearized theory is a weak-field approximation to general relativity: we write and solve the Einstein equations in a nearly flat space-time. With this formulation, we can separate the "static" and the wave parts of the metric. We can do this because any likely source of GWs for the detectors at Earth will be very distant, and the amplitude of the GWs will be very small.

In linearized theory, the metric can be decomposed as[1] [6]:

$$g_{\mu\nu} = \eta_{\mu\nu} + h_{\mu\nu}, \tag{1.2}$$

where $g_{\mu\nu}$ is the metric of space-time, $\eta_{\mu\nu}$ is the metric of unperturbed Minkowski space-time (diag$[-1, 1, 1, 1]$) and $h_{\mu\nu}$ is a perturbation of the flat space-time ($|h_{\mu\nu}| << 1$). All these quantities are symmetric tensors, and, for this reason, they only have ten independent components. Linearized theory is an approximation to general relativity that is correct to first order in the size of the metric perturbation $h_{\mu\nu}$.

An example of a weak field situation is the solar system, where $|h_{\alpha\beta}| \sim |\Phi| \leq M_{\odot}/R_{\odot} \sim 10^{-6}$, where Φ is the gravitational potential for a point mass and $M_{\odot}$ and $R_{\odot}$ are the mass and the radii of the Sun respectively.

[1] A note on notation and conventions: we use units in which $G = c = 1$, Greek indices run from 0 to 3, repeated indices are summed (using Einstein's summation convention) and the comma indicates a partial derivative.

Now, we will derive the equation for the linearised Einstein equations. The Einstein tensor is defined as:

$$G_{\mu\nu} = R_{\mu\nu} - \frac{1}{2} g_{\mu\nu} R, \tag{1.3}$$

where $R_{\mu\nu}$ is the Ricci tensor, defined as the contraction of the Riemann tensor:

$$R_{\mu\nu} \equiv R^{\gamma}_{\mu\gamma\nu} \equiv \Gamma^{\gamma}_{\mu\nu,\gamma} - \Gamma^{\gamma}_{\mu\gamma,\nu} + \Gamma^{\sigma}_{\mu\nu}\Gamma^{\gamma}_{\sigma\gamma} - \Gamma^{\sigma}_{\mu\gamma}\Gamma^{\gamma}_{\sigma\mu}, \tag{1.4}$$

being $\Gamma^{\alpha}_{\beta\gamma}$ the Christoffel symbols, defined by:

$$\Gamma^{\alpha}_{\beta\gamma} = \frac{1}{2} g^{\alpha\mu}(g_{\mu\beta,\gamma} + g_{\mu\gamma,\beta} - g_{\beta\gamma,\mu}), \tag{1.5}$$

where $g_{\mu\nu}$ is the metric defined in equation (1.2). R is the Ricci curvature scalar, defined by:

$$R = g^{\mu\nu} R_{\mu\nu}. \tag{1.6}$$

We can linearise equation (1.5) using the metric defined in equation (1.2):

$$\begin{aligned}
\Gamma^{\mu}_{\alpha\beta} &= \frac{1}{2}(\eta^{\mu\nu} + h^{\mu\nu})(\eta_{\alpha\nu,\beta} + \eta_{\beta\nu,\gamma} - \eta_{\alpha\beta,\nu} + h_{\alpha\nu,\beta} + h_{\beta\nu,\gamma} - h_{\alpha\beta,\nu}) \\
&= \frac{1}{2}\eta^{\mu\nu}(h_{\alpha\nu,\beta} + h_{\beta\nu,\gamma} - h_{\alpha\beta,\nu}) \\
&= \frac{1}{2}(h^{\mu}_{\alpha,\beta} + h^{\mu}_{\beta,\alpha} - h^{,\mu}_{\alpha\beta}),
\end{aligned} \tag{1.7}$$

where in the first line we have used the fact that $|h_{\alpha\beta}| << 1$ and that the derivatives of the Minkowski metric $\eta_{\mu\nu}$ are zero. Also, we have used $\eta_{\mu\nu}$ instead of $g_{\mu\nu}$ to raise the indices of the components $h_{\mu\nu}$, because $h_{\mu\nu}$ behaves like a tensor defined on a flat spacetime, for which the metric is $\eta_{\mu\nu}$. From equations (1.4) and (1.7), we obtain:

$$R_{\mu\nu} = \Gamma^{\alpha}_{\mu\nu,\alpha} - \Gamma^{\alpha}_{\mu\alpha,\nu} = \frac{1}{2}(h^{\alpha}_{\mu,\nu\alpha} + h^{\alpha}_{\nu,\mu\alpha} - h^{\alpha}_{\mu\nu,\alpha} - h_{,\mu\nu}), \tag{1.8}$$

where the last term means $h \equiv h^{\alpha}_{\alpha} = \eta^{\alpha\beta} h_{\alpha\beta}$. If we contract $R_{\mu\nu}$ once more, we obtain the curvature scalar R. Now, we take all the objects that we have calculated and substitute them into (1.3), getting:

$$G_{\mu\nu} = \frac{1}{2}(h^{\alpha}_{\mu\alpha,\nu} + h^{\alpha}_{\nu\alpha,\mu} - h^{\alpha}_{\mu\nu,\alpha} - h_{,\mu\nu} - \eta_{\mu\nu}(h^{,\alpha\beta}_{\alpha\beta} - h^{\beta}_{,\beta})). \tag{1.9}$$

We can simplify the last equation by introducing a modified expression for the metric perturbation, called the trace-reversed metric perturbation:

$$\bar{h}_{\mu\nu} = h_{\mu\nu} - \frac{1}{2}\eta_{\mu\nu} h. \tag{1.10}$$

Now, we can rewrite the Einstein field equation:

$$-\bar{h}^{\alpha}_{\mu\nu,\alpha} - \eta_{\mu\nu}\bar{h}^{\alpha\beta}_{\alpha\beta} + \bar{h}^{\alpha}_{\mu\alpha,\nu} + \bar{h}^{\alpha}_{\nu\alpha,\mu} = 16\pi T_{\mu\nu}. \tag{1.11}$$

The coordinate freedom of general relativity gives the possibility of choosing any coordinate system. We will use the harmonic gauge (equivalent to the Lorentz gauge condition of electromagnetism) in which the following condition is true:

$$\bar{h}^{\mu}_{\mu\alpha,} = 0. \tag{1.12}$$

With this choice of gauge, all the terms on the left side of equation (1.11) become zero, except for the first one (that represents the d'Alembert operator), and the linearized Einstein field equation becomes:

$$-\Box\bar{h}_{\mu\nu} \equiv (-\frac{\delta^2}{\delta t^2} + \nabla^2)\bar{h}_{\mu\nu} = 16\pi T_{\mu\nu}, \tag{1.13}$$

which in vacuum (absence of any sources) is:

$$\Box\bar{h}_{\mu\nu} = 0, \tag{1.14}$$

which is the typical wave equation.

A gauge transformation is a suitable change of coordinates defined by [7]:

$$x'^{\mu} \equiv x^{\mu} + \xi^{\mu}, \tag{1.15}$$

which induces a redefinition of the gravitational field tensor:

$$\bar{h}'_{\mu\nu} = \bar{h}_{\mu\nu} - \xi_{\nu,\mu} - \xi_{\mu,\nu} + \eta_{\mu\nu}\xi^{\lambda}_{,\lambda}. \tag{1.16}$$

It can be easily proved that ξ^{μ} must satisfy:

$$\xi^{\mu,\nu}_{,\nu} = 0 \tag{1.17}$$

so that the new gravitational field is in agreement with the harmonic gauge condition. In general, gauge transformations correspond to symmetries of the field equations, which means that the field equations are invariant under such transformations. This implies that the field equations do not determine the field uniquely; however, this ambiguity in determining the field is devoid of any physical meaning.

The simplest solution to this equation is the plane wave solution:

$$\bar{h}_{\mu\nu} = \mathrm{Re}(A_{\mu\nu} \exp ik_{\alpha}x^{\alpha}), \tag{1.18}$$

where "Re" denotes the real part, and the components $A_{\mu\nu}$ and k_{μ} are the amplitude tensor and the wave vector ($k_{\mu} = (w, k_x, k_y, k_z)$) respectively, where w is the frequency of the wave. The amplitude gives the "strength" of the wave (the displacement of space-time that it can create), and it is related to the source of the gravitational waves. If we apply the harmonic gauge condition (equation (1.12)) to the plane wave solution, we find:

$$k_{\alpha}k^{\alpha} = 0, \tag{1.19}$$

$$A_{\mu\alpha}k^{\alpha} = 0. \tag{1.20}$$

The first equation leads to the condition $-w^2 + k_x^2 + k_y^2 + k_z^2 = 0$, which implies that the wave-vector is "light-like" (meaning that gravitational waves travel at the speed of light). The second equation implies that the amplitude tensor is orthogonal to the wave vector (the waves are transverse). This relation can be written as four equations that impose four conditions on $A_{\mu\alpha}$, and this reduces the independent components of the amplitude tensor to six. Due to the gauge freedom (the freedom in choosing the four components of the vector ξ_μ), the actual number of independent components of $A_{\mu\alpha}$ can be reduced to two. We will use the transverse-traceless (TT) gauge to reduce the independent components to only two. It consists on a choice of coordinates (t, x, y, z) corresponding to an inertial (Lorentz) frame in the unperturbed flat background, which makes explicit that the perturbation is transverse (orthogonal to the direction of propagation), and trace-less ($A^\alpha_\alpha = 0$), meaning that the perturbation does not "compress" or "expand" elements of spacetime, but induces a (volume-preserving) "strain" only. Assuming that the waves propagate in the z direction ($k_x = k_y = 0$) and making use of the TT gauge, we can write $A_{\mu\nu}$ as:

$$A^{TT}_{\mu\nu}(t, z) = \begin{pmatrix} 0 & 0 & 0 & 0 \\ 0 & A_{xx} & A_{xy} & 0 \\ 0 & A_{xy} & -A_{xx} & 0 \\ 0 & 0 & 0 & 0 \end{pmatrix}, \tag{1.21}$$

and:

$$h^{TT}_{\mu\nu}(t, z) = \begin{pmatrix} 0 & 0 & 0 & 0 \\ 0 & h_{xx} & h_{xy} & 0 \\ 0 & h_{xy} & -h_{xx} & 0 \\ 0 & 0 & 0 & 0 \end{pmatrix}, \tag{1.22}$$

where $\bar{h}^{TT}_{xx} = A^{TT}_{xx} \cos(w(t - z))$ and $\bar{h}^{TT}_{xy} = A^{TT}_{xy} \cos(w(t - z))$.

In general, any gravitational wave propagating along the z-axis can be expressed as a linear combination of the "+" and "×" polarizations (the two independent components of the amplitude tensor):

$$h = h_+ e_+ + h_\times e_\times, \tag{1.23}$$

where e_+ and $e_\times$ are the vector basis of the wave:

$$e_+ = \begin{pmatrix} 0 & 0 & 0 & 0 \\ 0 & 1 & 0 & 0 \\ 0 & 0 & -1 & 0 \\ 0 & 0 & 0 & 0 \end{pmatrix} \quad \text{and} \quad e_\times = \begin{pmatrix} 0 & 0 & 0 & 0 \\ 0 & 0 & 1 & 0 \\ 0 & 1 & 0 & 0 \\ 0 & 0 & 0 & 0 \end{pmatrix}, \tag{1.24}$$

with:

$$h_{\mu\nu}^{TT}(t,z) = \begin{pmatrix} 0 & 0 & 0 & 0 \\ 0 & h_+ & h_\times & 0 \\ 0 & h_\times & -h_+ & 0 \\ 0 & 0 & 0 & 0 \end{pmatrix}. \tag{1.25}$$

A typical example of the effect on matter of a passing gravitational wave is pictured in figure 1.2. It shows the effect of the passage of a plane gravitational wave, propagating along the z-axis, on a ring of test particles. This effect can be calculated using the geodesic equation. The upper panel of the figure shows the case where the metric perturbation has $A_{xx}^{TT} \neq 0$ and $A_{xy}^{TT} = 0$. Time goes from left to right. Every panel shows five different phases (different values of ωt) of the oscillation of the wave, the first and the last one being the same (finishing a full cycle). The lower panel shows the opposite case, where the metric perturbation has $A_{xx}^{TT} = 0$ and $A_{xy}^{TT} \neq 0$. The change in the proper distance between the test particles during the passage of the gravitational wave is the physical quantity which gravitational wave detectors aim to measure, called ΔL. Solutions with $A_{xx}^{TT} \neq 0$ are identical to solutions with $A_{xy}^{TT} \neq 0$, except for a rotation of $\pi/4$ radians. For this reason, these two solutions represent two independent gravitational wave polarization states, and these states are usually denoted by "+" and "×" respectively.

The measured scalar amplitude $h(t)$ by an interferometric-like detector due to a gravitational wave described by the tensor $h_{\mu\nu}^{TT}$ is given by:

$$h(t) = \frac{1}{2}(e_1^i e_1^j - e_2^i e_2^j) h_{ij}^{TT} = F_+(t)h_+(t) + F_\times(t)h_\times(t), \tag{1.26}$$

where e_1^i and e_2^i are unitary vectors in the detector arms direction, and $h_{+,\times}$ are the two polarisation states shown in equation (1.25). $F_{+,\times}(t, \psi, \vec{n})$ are the "antenna-pattern" functions, which take values between -1 and 1. They describe the detector sensitivity to each polarisation ($+$ and $\times$), depending on the relative orientation of the detector and the source $\vec{n}$, and the polarisation angle ψ of the wave. These functions will be described later in this chapter.

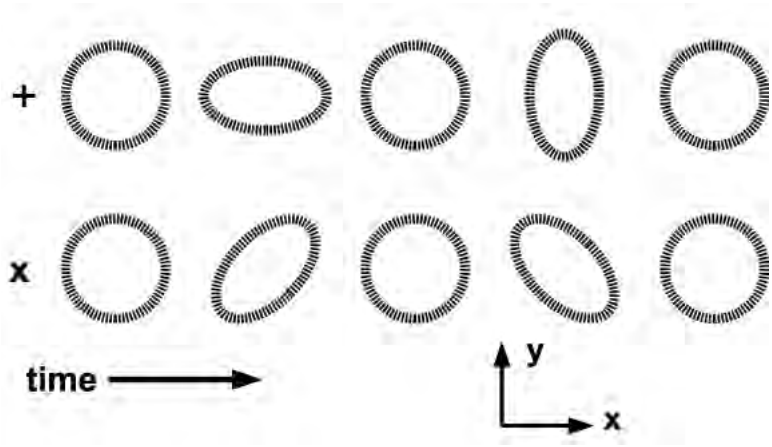

Fig. 1.2: Illustration of the effect of a gravitational wave travelling in the z direction on a ring of test particles. It shows the two polarisations, which are clearly translated by $\pi/4$ radians. Source: http://inspirehep.net/record/818927/plots

1.1.2 | The production of gravitational waves

The emission of gravitational waves is usually described by the quadrupolar formalism [7]:

$$h_{jk}^{TT}(t) = \frac{2G}{c^4}\frac{1}{d}[\ddot{\Gamma}_{jk}(t - \frac{d}{c})]^{TT}, \tag{1.27}$$

where d is the distance to the source and $[\Gamma_{jk}(t - \frac{d}{c})]^{TT}$ is the quadrupolar mass tensor of the source (the dots indicate derivatives in time). This formalism is only valid if the size of the source is small compared to the wavelength $\frac{\lambda}{2\pi}$ of the emitted wave. The mass-quadrupole moment Γ_{jk} of the source is defined as the coefficient of the $1/r^3$ term in an expansion in powers of $1/r$ of the Newtonian gravitational potential (far from the source). For sources with weak internal gravity, this can be directly expressed as:

$$\Gamma_{jk} = \int \rho(\vec{x})[x_j x_k - \frac{1}{3}r^2\delta_{jk}]d^3x, \tag{1.28}$$

where $\rho(\vec{x})$ is the mass density of the source. This is simply the Newtonian moment of inertia with the trace removed. The energy emission rate (also called gravitational wave luminosity) is given by:

$$L_{GW} = \frac{1}{5}\frac{G}{c^5}\langle\dddot{\Gamma}_{jk}\dddot{\Gamma}_{jk}\rangle, \tag{1.29}$$

where $\langle$ ... $\rangle$ denotes a temporal average over several periods. This quadrupolar formula shows that a gravitational wave only is created if the time derivative of a distribution of energy is not equal to zero.

To give an example, we can calculate the emission rate of a neutron star. If it is perfectly symmetric, the derivative of the quadrupolar mass tensor will be zero, but if it has a little asymmetry, characterised by the ellipticity parameter ϵ, the derivative will not be zero, and the emission rate will be approximately given by:

$$L_{GW} \propto \frac{G}{c^5}\epsilon^2 I_{zz}^2 \nu^6, \tag{1.30}$$

where $I_{zz} \sim MR^2$ is the inertia moment of the rotation axis, and ν is the frequency of rotation. Giving some values to these parameters, we can arrive at an estimate of the gravitational wave luminosity. We have $G/c^5 \sim 10^{-53}$ s/J, $I_{zz} \sim 10^{38}$ kg m^2 (the canonical moment of inertia for a neutron star), $\epsilon \sim 10^{-6}$, and $\nu \sim 100$ Hz, giving a value for the luminosity of $L_{GW} \sim 10^{23}$ W, which is a little lower than the luminosity of the Sun due to electromagnetic radiation ($L_\odot = 10^{26}$ W) [8].

1.2 | Gravitational wave detectors

Einstein published the paper about gravitational waves in 1916, but he thought that we would never be able to detect them. In the 1960s, Weber designed the first experiment to detect gravitational waves: a resonant bar detector [9]. These resonant bar detectors were metallic bars ($\sim$ 2 tones of aluminium), made to resonate at approximately 1500 Hz when a gravitational wave passed through them. These bars never detected any gravitational wave, because its sensitivity was too small ($\sim 10^{-13}$). Nowadays some bars are still operated, like NAUTILUS (Frascati, Italy), or AURIGA (Padova, Italy), but their narrow sensitivity band does not make them the best tool to detect gravitational waves. For this reason, a new instrument had to be developed. This instrument was the inferometric gravitational wave detector. The seeds of the idea for interferometric detectors date from the 50's [10], and the first detailed descriptions of these detectors were produced in the 70's [11]. The first interferometric detectors were constructed in the 90's.

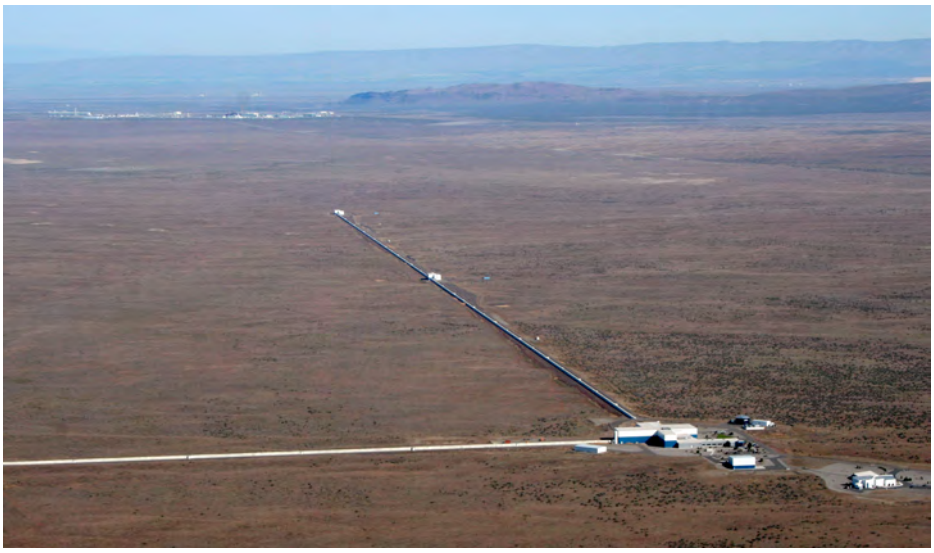

Fig. 1.3: Aerial image of the LIGO Hanford gravitational wave observatory, with 4 km arms. Source: LIGO.

Some of the ground-based interferometric gravitational wave detectors that exist are:

- **LIGO:** the Laser Interferometer Gravitational-wave Observatory (LIGO) is composed of two detectors, one of 4 km in Hanford (WA) called H1 and another 4 km detector in Liv-

ingston (LA) called L1 (Initial LIGO had another detector of 2 km called H2 inside the one of 4 km) [12]. The observatories are separated by ~ 3000 km. Figure 1.3 shows a picture of the Hanford interferometric detector from the outside. The Initial LIGO gravitational wave detectors were operating between 2002 and 2010, in six different science runs, not finding any gravitational wave signal. From $\sim 2010 - 2015$ the detectors underwent a series of major upgrades to enhance their sensitivity, becoming the first "second generation" gravitational-wave detectors, called Advanced LIGO. This enhancements will make LIGO an order of magnitude more sensitive than Initial LIGO (a 1000 factor in observable volume). It is expected that a third Advanced LIGO detector will be transported and built in India.

- **Virgo:** the Virgo detector is part of a collaboration between some european countries that are part of EGO (European Gravitational Observatory) [13]. It is a 3 km interferometer located in Cascina (Italy). In general, the sensitivity of this detector is a little bit worse than LIGO. At the current time, Virgo is being updated, like LIGO was, to become Advanced Virgo, a second generation gravitational-wave detector. During the last decade, the network LIGO-Virgo have tried to collaborate by having the science run periods at the same time. Some years ago, the two scientific collaborations joined efforts having common working groups, sharing data and publishing results together.

- **GEO:** GEO-600 is a 600 m detector built as a collaboration between the United Kingdom and Germany, located near Hannover (Germany) [14]. Its longitude makes it the least sensitive detector, and, because of this, it cannot compete with LIGO or Virgo, except at high frequencies. It has been used as a test bank for the technology that is implemented in Advanced LIGO and Virgo. It is still in operation in the so called astro-watch mode.

- **TAMA:** TAMA-300 was a 300 m interferometric japanese project built in the city of Tokyo. The aim of the project was to develop advanced techniques needed for building a future interferometer. TAMA was followed by CLIO, a 100 m cryogenic detector.

- **KAGRA:** a japanese detector located in the same place as the Kamioka neutrino observatory (at 200 meters beneath Earth) [15]. KAGRA did a test run in 2015, and it will join the science runs of LIGO and Virgo around 2018. KAGRA has arms of 3 km and it operates with cryogenic technology.

- **Einstein Telescope:** ET is the european project to build a third generation gravitational waves detector. Many institutions have joined efforts in designing what should be the first "third generation" gravitational wave detector. Currently, ET is in its design phase. It will be underground and it will use cryogenic techniques, with arms of 10 km [16].

A timeline of the periods (called "**science run**") in which the initial ground-based detectors have been operating is shown in figure 1.4. A science run is a period of time in which the detectors are active and taking data that will be analysed to search for astrophysical sources.

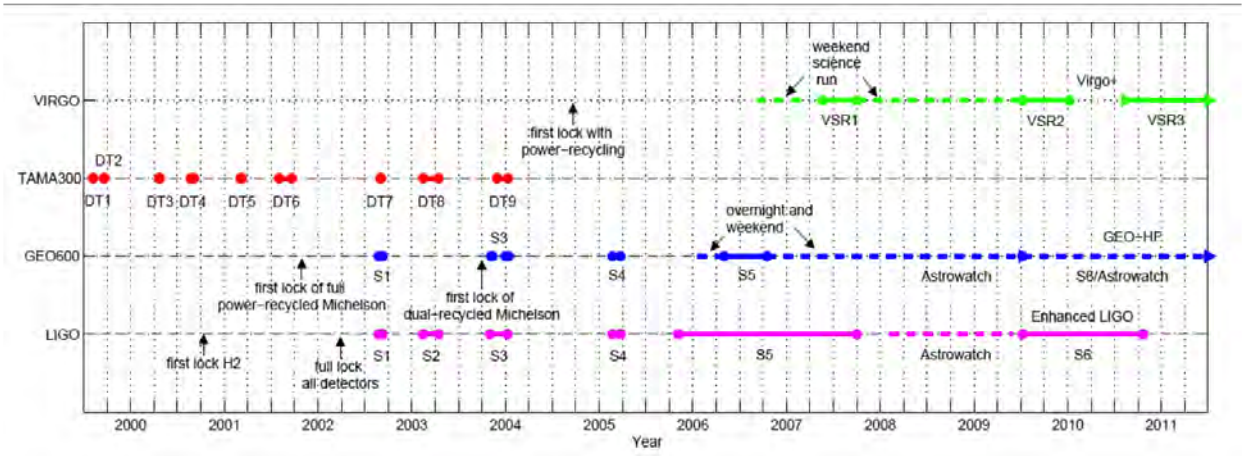

Fig. 1.4: Timeline of the different science runs of the ground-based gravitational wave detectors. Source: Alicia Sintes

The detectors are not always "online" (working in science mode): they take time between the science runs to make upgrades to the technology. Besides, due to seismic noise, equipment failures and other problems, the duty cycle of a science run (the fraction of time where the detectors are taking data) is generally less than 100%, varying for each detector an each science run, normally having values between $\sim 50\%$ and $\sim 90\%$. The last science run was called O1, which started on September 2015 and ended on January of 2016. This was the first science run of the Advanced LIGO detectors.

Besides these ground-based interferometric gravitational wave detectors, a project to send an interferometric detector to the outer space exists, called **LISA**, [18]. The Laser Interferometer Space Antenna is a proposed project to build a laser interferometer consisting of three spacecrafts in solar orbit, with near equilateral triangular configuration of at least 10^6 km baselines. Being outside Earth, this detector would not have the same noise sources as the terrestrial detectors, making it a perfect instrument to detect sources at other frequencies, complementing the work done by the ground-based interferometers.

In addition to the bars and the interferometric detectors, another technique to detect gravitational waves is used nowadays, called **pulsar timing array** [17]. It uses the precise arrival times of the pulsars electromagnetic signals as the tool to measure the waves. If a gravitational wave passes between the pulsar and the Earth, the time of arrival of the pulse will change. This is what the Pulsar Timing Array aims to detect.

Another possibility is the indirect detection of gravitational waves in the very low frequency band based on measurements of the B+ polarization modes of the cosmic microwave background. These indirect detections could give information of the early Universe.

1.3 | How does an interferometric gravitational wave detector work?

As we explained before, gravitational waves have two polarisations, rotated by 45°. A passing gravitational wave will stretch and squeeze space in the direction of every polarisation, and the proper distance between test masses will change. If we could detect this change of distance between the masses, we would be able to detect gravitational waves. We can achieve this with interferometric detectors. These detectors measure the difference of the light travel time of a laser beam travelling back and forth along the arms of a Michelson interferometer.

In figure 1.5 the composition of a Michelson interferometer is shown. Four masses (test masses) are hanging inside two perpendicular arms with an "L" shape (forming a 90° intersection). A laser shots a beam of light that reaches the beamsplitter - half of the laser light is transmitted into one arm while the other half is reflected into the second arm - and then travels through these two arms, reaching the end. The laser light travels back and forth many times: the arms are Fabry-Perot cavities (they are very reflective, increasing the power of the laser's light). After bouncing, the light returns to the beamsplitter, where it interferes with the beam coming from the other arm. If no gravitational wave passes through the detector during the time that the laser's light was travelling, the beams from the two arms will interfere and no light will be detected by the photodetector. On the contrary, if a gravitational wave passed through the detector, the beams will not interfere and the photodetector will detect some light. The pattern formed by the light received at the photodetector gives us information about the gravitational wave, like its amplitude, frequency, etc.

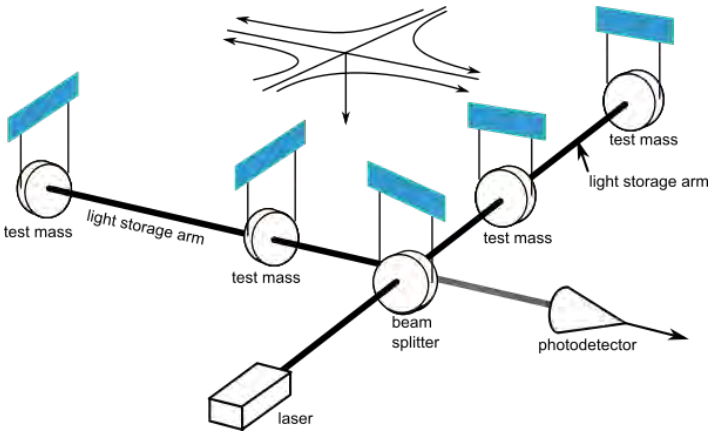

Fig. 1.5: Scheme of an interferometric detector: two masses located close together in the vertex of the "L" shaped structure and the other two at the end of each of the interferometer's arms. The laser shots a beam that is splitted in the beamsplitter, and travels down through both arms, reaching the end and returning to the beamsplitter. If a gravitational wave passes by, light reaches the photodetector.

One common misconception about detecting gravitational waves with an interferometric detector is that, just like the expansion of the Universe causes cosmological redshift (a change of

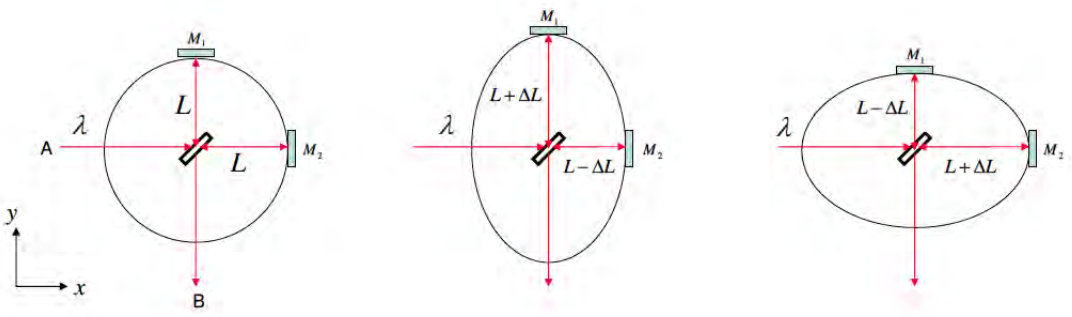

Fig. 1.6: Different stages of the length of the detector arms. When a gravitational wave passes through the detector, it stretches one arm and squeezes the other. After some time, it does the opposite: squeezes the arm that was stretched, and viceversa. Source: https://en.wikipedia.org/wiki/Gravitational-wave_observatory

the wavelength of light), gravitational waves should also cause an extension or shortening of the wavelength of the laser light that travels in the detector. If the wavelength of the light changes like the interferometer arm does, there should be no change in phase and therefore no detection. The solution of this misconception has to do with coordinate invariance and gauges: the gravitational wave affects differently the wavelength of light and the length of the interferometer's arm, because light is moving. The interferometer works by measuring the differential stretching of the two arms while the high frequency light wave essentially experiences no inhomogeneities in the medium in which it propagates (the gravitational wave) because the wavelength λ_{gw} of the gravitational wave is so much larger than the wavelength of light. A mathematical description of this issue can be found in [19].

A gravitational wave with an amplitude of $h = 10^{-21}$ will only produce a change in the length of the arms of $\Delta L \propto hL = 4 \times 10^{-21}$ km, with $L = 4$ km being the length of the detector arms. This is much shorter than the width of a proton, and we want to detect a change of this size with our inteferometers. This would be sufficiently difficult by itself, but besides that, the detector is not an ideal instrument: it has some sources of noise of instrumental and environmental origin that can mask the gravitational wave signals we are looking for. This makes the task more challenging: we have to identify this sources and understand how they behave in order to prevent confusions between noises and real gravitational wave signals. Some of this sources are:

- **Quantum noise:** due to the quantum properties of the photons of the laser. The shot noise comes from the randomness of the times of arrival of the photons at the photodetector, and this creates a fluctuation in the power received. Also, the photons of the laser inflict a pressure on the mirror surfaces. This generates an stochastic force that shakes the mirrors, which is called radiation pressure. The quantum noise is important beyond 100 Hz, being the main noise source at these frequencies.

- **Displacement noise:** due to the movements of the physical components of the detectors,

like the mirrors. The seismic noise comes from the motion of Earth's ground. The Newtonian noise comes from the gravitational force of objects that are moving. The thermal noise comes from the movements of the atoms of the mirror and the suspensions. If the light bounces back and forth many times, this noise can become large. The use of pendulums to isolate this noise can filter out the frequencies above the natural frequency of the pendulum. For a 0.5 m pendulum, one achieves filtering above a few Hertz. The seismic noise is the biggest source of noise in frequencies lower than $\sim$ 10 Hz, and the thermal noise is the main noise between frequencies of $\sim 10 - 100$ Hz.

- **Other noises:** there are more sources of noise, like environmental noise, due to the human activities in the nearby facilities, the traffic of the nearby roads, the tides, etc. Another source of noise comes from particles that are present in the arms of the detector: high technology for creating vacuum is used, but some particles remain inside the tubes.

Besides these noise sources that characterise the sensitivity of the detector, there are other contributions to the noise that appear in the spectrum as "lines". These lines come from different sources: the power harmonics of the electricity components (60 Hz and its harmonics); the violin modes, coming from the suspensions of the mirrors; and the calibration lines, coming from the calibration of the detector instrumentation. There are also many transient artefacts due to environmental noise.

With all these noise sources in mind, is easy to see that the real noise of the detector is far away from being Gaussian. Moreover, the noise has different behaviours in different frequency regions (for example, the noise at 50 Hz is very different from the noise at 1000 Hz).

To detect these lines and disturbances caused by the various noise sources, each of the LIGO detectors records over 200,000 auxiliary channels that monitor instrument behavior and environmental conditions [20]. These channels allow us to compare the gravitational wave strain with the other channels at the same time, and check if there any correlations - noise sources that could have produced the signal.

Periods of time in which there are significant problems with the quality of the data are vetoed. To signalise these vetoes, LIGO uses a system of flags and triggers to classify the data. Data quality flags typically exclude periods of data on the order of seconds to hours, for example, for periods when any of the photodiodes used to sense the laser field in the detector were overflowing their analog-to-digital converters. Data quality triggers are short duration vetoes generated by algorithms that identify significant statistical correlations between a transient in $h(t)$ and transient noise in auxiliary channels. There are three data quality categories, classifying the most and the least usable data.

1.3.1 | Antenna beam pattern functions of an interferometric detector

The gravitational wave will travel almost unaltered (because of the little interaction of gravitational waves with matter) from the source to the detector at the speed of light. In a coordinate system tied to the wave (x', y', z'), where z' is the propagation direction and perturbations are contained in the $x' - y'$ plane, the gravitational wave can be described by [44]:

$$H' = h_+(\hat{x}' \times \hat{x}' - \hat{y}' \times \hat{y}') + h_\times(\hat{x}' \times \hat{y}' + \hat{y}' \times \hat{x}'), \tag{1.31}$$

where $\times$ represents a tensorial product, and $\hat{x}'$ and $\hat{y}'$ are unit vectors parallel to x' and y'. We can transform this equation into:

$$H' = \begin{pmatrix} h_+ & h_\times & 0 \\ h_\times & -h_+ & 0 \\ 0 & 0 & 0 \end{pmatrix}. \tag{1.32}$$

As we said before, the effect of a gravitational wave on to the detector will consist on expanding and stretching its arms. If we want to calculate the strength of this effect, we have to change the system of coordinates of equation (1.32) from the propagation system to the detector one. The general equation of the response of an interferometric detector to a gravitational wave is:

$$h(t) = \frac{1}{2} n_1^T \cdot H \cdot n_1 - \frac{1}{2} n_2^T \cdot H \cdot n_2, \tag{1.33}$$

where n_1 and n_2 are the unit vectors parallel to the detector arms, and H is the expression in equation (1.32) in the detector coordinate system. To go from (x', y', z') to (x, y, z) (the coordinates of the detector, where x and y define the plane of the detector, and z points to the zenith), we must perform three Euler rotations:

1. Rotate the wave plane an angle -ϕ around axis z' so the planes $x' - y'$ and $x - z$ are the same.

2. Rotate the wave plane an angle $\pi - \theta$ (this is the angle that the z axis forms with z') around y axis so the axis z and z' are the same.

3. Rotate the wave plane an angle ψ around z axis so the planes (x', y') and (x, y) are the same.

We define the polarisation angle ψ as [7]:

$$\cos(\psi) = \hat{N} \cdot (\hat{L} \times \hat{z}) \quad \text{and} \quad \sin(\psi) = |\hat{L} \cdot \hat{z} - (\hat{L} \cdot \hat{N})(\hat{z} \cdot \hat{N})|, \tag{1.34}$$

where $\hat{N}$ is the unit vector pointing to the source from the detector and $\hat{L}$ is the unit angular momentum of the source. ψ can be defined as the angle between the direction $n \times Z$ and the x-axis of the TT wave-frame (corresponding to the "+" polarization), where $Z = (0, 0, 1)$ is the unit-vector pointing to the celestial north pole.

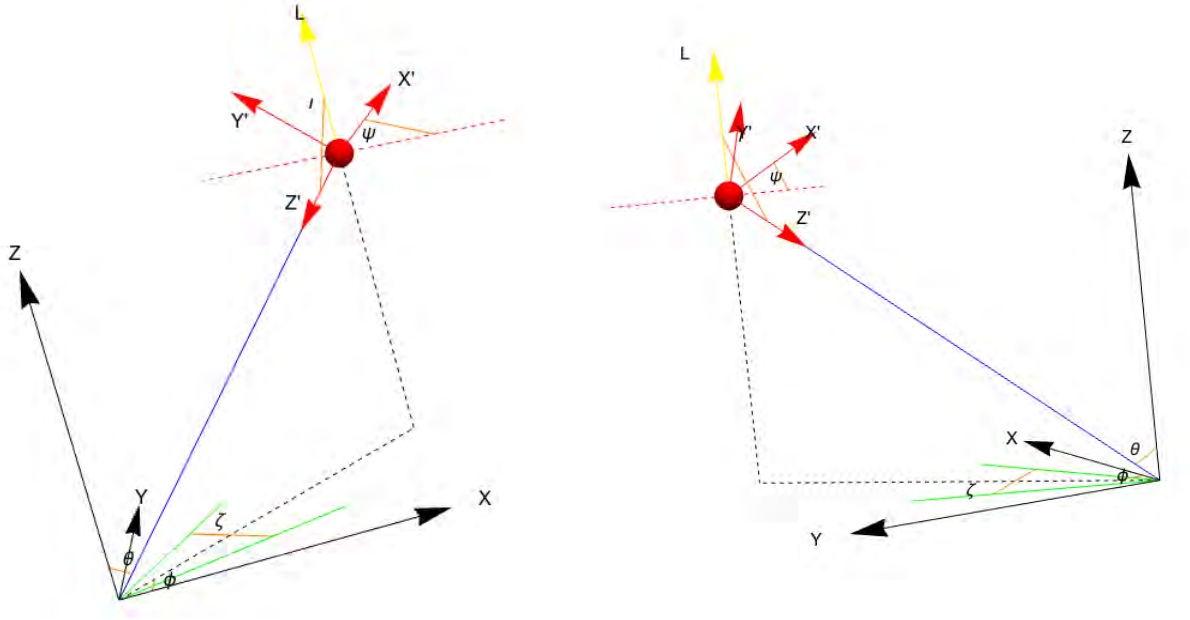

Fig. 1.7: Wave and the detector coordinate systems from two different angles. The angle ψ between the x' axis and the + polarisation of the wave is the polarization angle; ϕ is the angle between the detector's x axis and the line joining the origin of the x, y, z system and the projection of the source onto the $x-y$ plane; θ is the angle between the z axis and the line joining the origin of the x, y, z system with the source (the "line of sight"); ι is the angle between the angular momentum ($\vec{L}$) of the source and the line of sight; ζ is the angle between the two arms of the detector (90^o for the LIGO detectors).

After the three rotations, the wave and detector coordinate systems will be the same. The matrix of rotation M is:

$$M = R_z(-\phi) \cdot R_y(-\theta + \pi) \cdot R_z(\psi) =$$
$$\begin{pmatrix} \sin(\phi)\sin(\psi) - \cos(\theta)\cos(\phi)\cos(\psi) & \cos(\psi)\sin(\phi) + \cos(\theta)\cos(\phi)\sin(\psi) & \cos(\phi)\sin(\theta) \\ \cos(\theta)\cos(\psi)\sin(\phi) + \cos(\phi)\sin(\psi) & \cos(\phi)\cos(\psi) - \cos(\theta)\sin(\phi)\sin(\psi) & -\sin(\theta)\sin(\phi) \\ -\cos(\psi)\sin(\theta) & \sin(\theta)\sin(\psi) & -\cos(\theta) \end{pmatrix}. \tag{1.35}$$

The perturbation equation (1.32) can be written in the detector frame performing this operation:

$$H = M \cdot H' \cdot M^T, \tag{1.36}$$

and the unit vectors $\hat{n}$ parallel to the arms can be written as:

$$n_1 = \begin{pmatrix} \cos\left(\frac{\pi}{4} - \frac{\zeta}{2}\right) \\ \sin\left(\frac{\pi}{4} - \frac{\zeta}{2}\right) \\ 0 \end{pmatrix} \quad \text{and} \quad n_2 = \begin{pmatrix} \sin\left(\frac{\pi}{4} - \frac{\zeta}{2}\right) \\ \cos\left(\frac{\pi}{4} - \frac{\zeta}{2}\right) \\ 0 \end{pmatrix}, \tag{1.37}$$

where ζ describes the angle between the two detector arms, being 90^o the angle of the LIGO detectors.

With all these equations, the gravitational wave signal at the detector can be described like this:

$$h(t) = h_+(t)F_+(\theta,\phi) + h_\times(t)F_\times(\theta,\phi), \tag{1.38}$$

where $F_+(\theta,\phi,\psi,\zeta)$ and $F_\times(\theta,\phi,\psi,\zeta)$ are the antenna pattern functions. They depend on the sky position of the source, the polarisation angle and the angle between the detector arms. They can be expressed with these equations [7]:

$$\begin{aligned} F_+ &= \sin(\zeta)[\frac{1}{2}(1+\cos^2(\theta))\cos(2\psi)\cos(2\phi) - \cos(\theta)\sin(2\psi)\sin(2\phi)], \\ F_\times &= -\sin(\zeta)[\frac{1}{2}(1+\cos^2(\theta))\sin(2\psi)\cos(2\phi) + \cos(\theta)\cos(2\psi)\sin(2\phi)]. \end{aligned} \tag{1.39}$$

These functions make the gravitational wave amplitude depend on time, because the angles θ and ϕ, expressing the sky position of the source in the detector coordinates, are changing with time because of the Earth's motion around the Sun. When a source of gravitational waves is in a position of the sky that makes the antenna pattern functions equal to zero, the detector is unable to detect these waves - this makes the detector "blind" to some directions in the sky that depend on time.

1.4 | Sources of gravitational waves

We can classify gravitational waves according to the type of source that emits them. As we said before, any accelerated mass can emit gravitational waves, including humans, but the amplitude of such waves would be extremely weak ($h \sim 10^{-43}$) [35]. From the wide variety of objects that we find in the Universe, we will look for only those ones being highly compact[2] and moving close to relativistic speeds. Figure 1.8 shows the different type of sources and the frequency of their gravitational waves. This frequency is related with the size and the mass of the object that emits them. The frequency band of good sensitivity for the ground-based detectors is located between $\sim$ 10 Hz and several kHz, so with these detectors we will only be able to detect the sources that emit GWs in this range.

We can divide the sources of gravitational waves that we expect to detect with a ground-based detector in four different groups: stochastic background, bursts, stellar-mass compact binary coalescences and continuous waves:

- **Stochastic background**: the stochastic background of gravitational waves comes from the superposition of a large number of unsolved gravitational wave sources of astrophysical and cosmological origin. Unsolvable sources are those which we cannot distinguish individually, either because they are too quiet or because there are simply too many occurring at once. Cosmological backgrounds are predicted to have been produced by sources that existed in the very early Universe, as for example during the inflation period (at $\sim 10^{-36}$

[2]Compacticity is measured as the ratio between the mass and the radii of an object, being 0.5 the maximum (theoretical value for a Schwarzschild black hole).

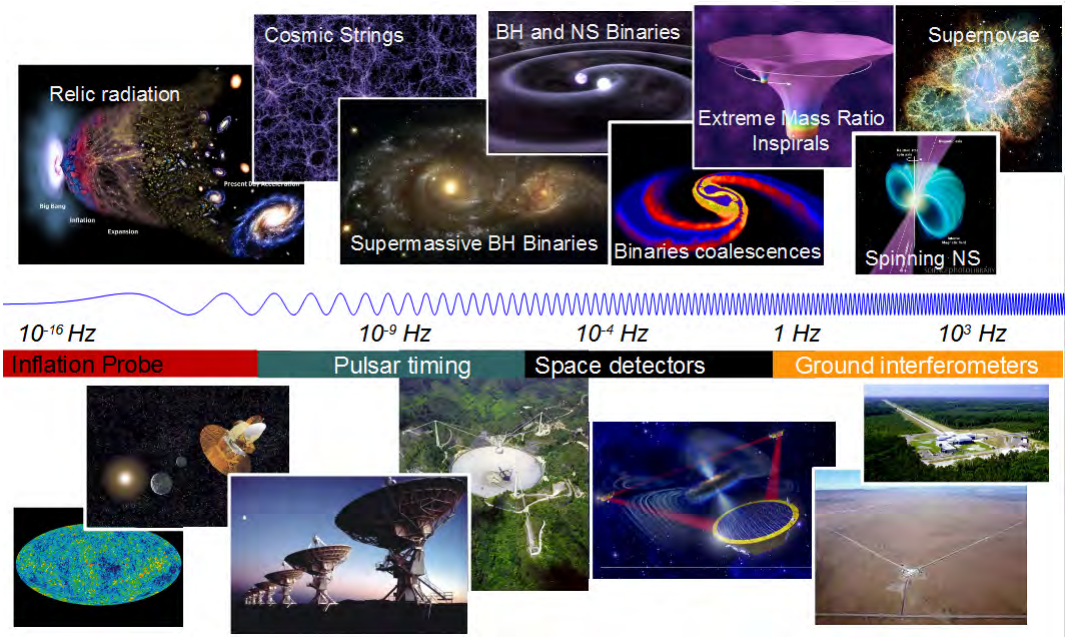

Fig. 1.8: Different sources of gravitational waves and their frequency. It also shows the instruments sensitive to each of the different frequency bands. The frequency band of good sensitivity for the ground-based detectors is approximately between 10 *and several kHz. Source: Alicia Sintes.*

seconds after the Big Bang), while astrophysical backgrounds are predicted to have been produced by systems of massive stars such as the neutron stars and black holes that we see today. The strength of the gravitational-wave background at different frequencies strongly depends on the type of sources that produce them. Thus, depending on the type of gravitational-wave background we detect, we may learn about the state of the Universe just a few moments after the Big Bang or how the Universe is evolving in more recent times.

- **Burst**: the burst signals come mainly from supernovae and gravitational collapse, but other exotic objects like cosmic strings or unknown phenomena could produce them as well. Gravitational collapse is one of the most violent events known to astronomy, and probably, the least understood source of gravitational radiation. This is because we have little direct information about what's happening in the interior of the collapse, and we cannot make trustful predictions about the radiation coming from it. These signals have a very short duration, and we don't have accurate theoretical models of the waveforms to compare.

- **Stellar-mass Compact Binary Coalescence**: the CBC is composed of gravitational waves coming from compact binary systems like a binary black hole, a binary neutron star or a black hole-neutron star binary of stellar masses. When two of these objects orbit each other in a binary system, the emission of gravitational waves will gradually carry away some of their orbital energy, forcing them to get closer together. This happens slowly at first, but as the orbit gets tighter the gravitational wave ampltiude and the frequency

become higher and the process accelerates until eventually the stars collide and merge. The gravitational waves emitted by binary mergers are not random bursts of energy, but are instead highly structured waveforms that carry a lot of information about the emitting systems: the masses of the two inspiraling objects, their spins (how fast they are rotating around their own axes), the location of the binary on the sky and its distance from Earth are all imprinted onto the signal recorded by the gravitational wave detectors. This is the type of signal that the Advanced LIGO detectors detected on September 14, 2015 (called GW150914) and on December 26, 2015 (called GW151226), becoming the first direct detections of gravitational waves.

- **Continuous gravitational waves**: these waves are almost monochromatic (their frequency changes very little) and have a very long duration. The signal amplitude is very low and it requires long observation times, up to months or even years to build up enough signal to be detectable. Continuous gravitational waves mainly come from rotating neutron stars. Besides long-duration continuous waves (CWs), neutron stars could also emit transient signals (much shorter) by different mechanisms, which could also follow the CW signal model. These signals are called transient continuous waves (tCWs).

CHAPTER 2

CONTINUOUS GRAVITATIONAL WAVES SEARCHES

This chapter contains an introduction to neutron stars and continuous gravitational wave searches. In the first section we will present a brief summary of neutron stars and its properties. In the second section, we will describe the continuous gravitational wave signal that comes from a neutron star. In the last section, we will summarise the different types of continuous wave searches.

2.1 | Neutron stars

A neutron star is the residual core that is left by a supernova of stars with masses approximately between $8M_\odot$ and $30M_\odot$, where $M_\odot$ indicates the mass of the Sun ($1,989 \times 10^{30}$ kg). They were first proposed in 1933 (one year after the discovery of the neutron) by Walter Baade and Fritz Zwicky [24]. The typical value for the mass of a neutron star is between 1 and 2 solar masses, and their size oscillates between 10 and 30 km of radii. These two properties make them the second densest object in the Universe, with a compactness ($C = M/R$) value of $C \sim 0.2$, putting them between black holes (with $C \sim 0.5$) and white dwarfs. Neutron stars are mostly composed of neutrons, as their name indicates (in figure 2.1, a more detailed description of the composition of a neutron star is shown). One of the biggest uncertainties about neutron stars is their equation of state, which at the moment is unknown. A review about the equation of state of neutron stars can be found in [21].

Neutron stars were just a theoretical object until 1967, when the first pulsar was discovered by Jocelyn Bell and Antony Hewish [22]. A pulsar is a neutron star with a fast rotational speed and an electromagnetic field emitted from its poles sufficiently strong to make the star visible to us. The emission of electromagnetic radiation by the poles and the rotation of the star makes the pulsar look like a lighthouse: when it's pointing to us, we can see it, and a moment afterwards it's gone; this pattern is repeated with a very stable frequency. In fact, this frequency (and its evolution) is so stable that pulsars are one of the most accurate clocks that exist. This is used

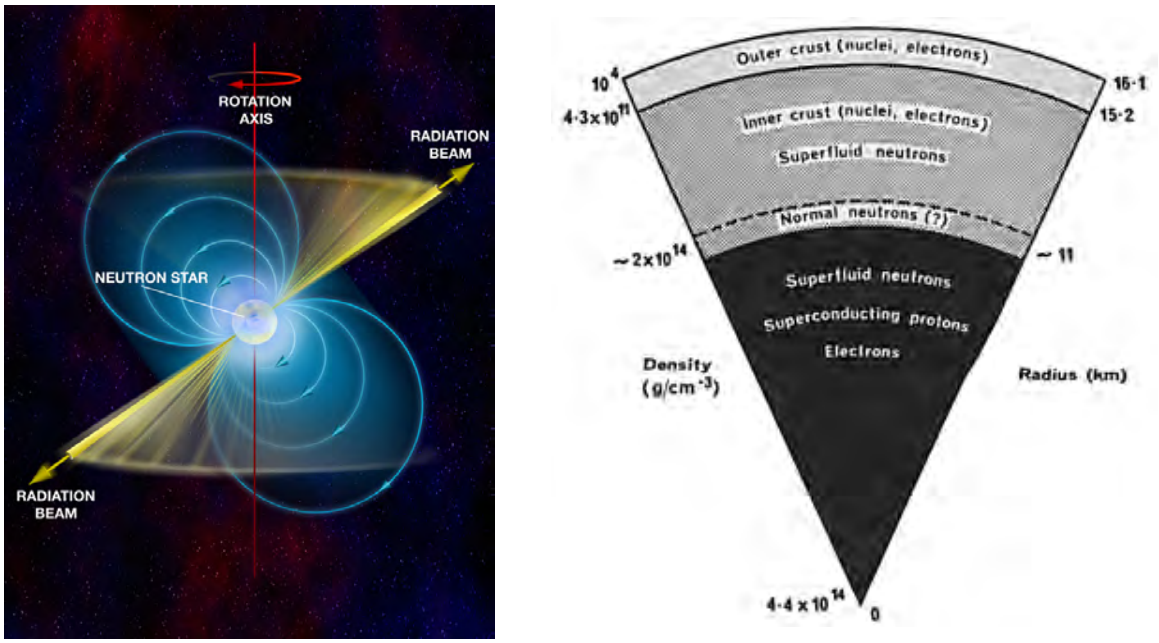

Fig. 2.1: Left panel: an artistic representation of a neutron star, showing its rotation axis, the radiation beam of the electromagnetic field and the electromagnetic field itself (the blue lines). Right panel: a slice of a neutron star showing the composition of each layer with the radius dependency. Source of left image: NRAO; source of right image: NASA (https://heasarc.gsfc.nasa.gov/docs/objects/binaries/neutron_star_structure.html).

Parameter	Rotation [Hz]	Distance [kpc]	Age [yr]	Magnetic field [G]
Maximum	716.35556	59.70	6.75×10^{10}	2.06×10^{15}
Minimum	0.08482	0.16	218	6.67×10^{7}

Table 2.1: Observational maximum and minimum of some pulsar parameters, taken from [23].

to detect gravitational waves with pulsar timing array techniques, as explained in the previous chapter [17].

In table 2.1 we can see the maximum and minimum of some properties of known pulsars. Figure 2.2 shows the derivative of the period versus the period for all known pulsars. These values are taken from the Australia Telescope National Facility, which maintains a list of all the discovered pulsars up to date and a database with all their properties [23].

Pulsars have a theoretical maximum rotational frequency, that we can know by equating the centripetal force to the gravitational force at the equator (supposing perfect spherical shape) [24]:

$$w_{max}^2 R = G\frac{M}{R^2}. \tag{2.1}$$

If $\nu_{max} = 2\pi w_{max}$, we have:

$$\nu_{max} = 2\pi\sqrt{\frac{GM}{R^3}}, \tag{2.2}$$

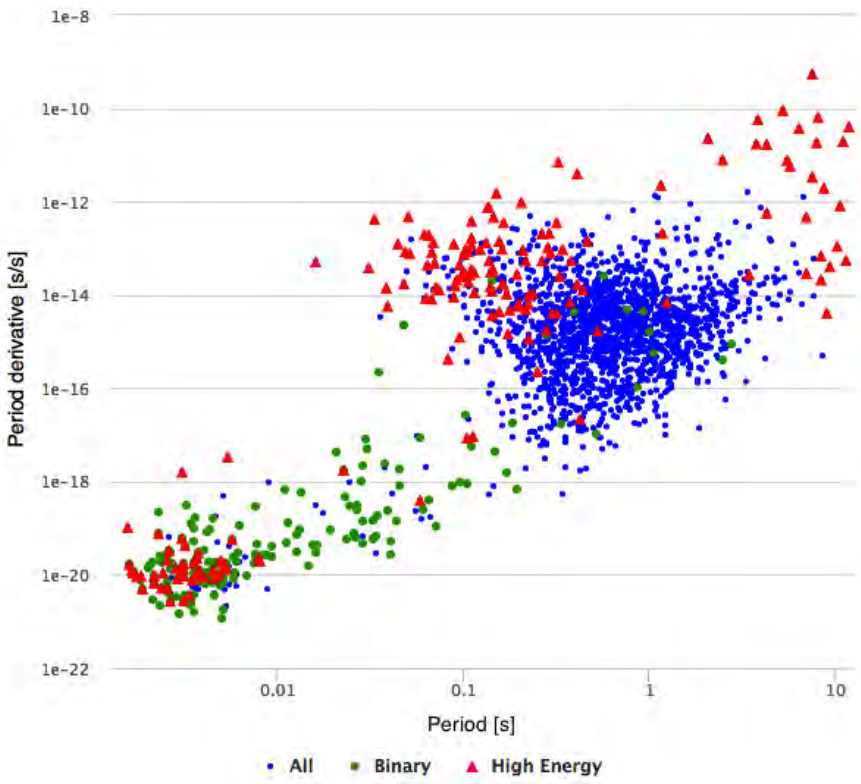

Fig. 2.2: Period and period derivative of all known pulsars.

which for a typical neutron star is $\sim 10^4$ Hz, agreeing with the experimental results.

Another important parameter of pulsars is the relation between the frequency of rotation and its derivative. This parameter is called the braking index, and can provide information about the energy loss mechanisms of pulsars, including GW emission. The spin-down of pulsars is expected to follow this equation [25]:

$$\dot{\nu} = -K\nu^n, \tag{2.3}$$

where ν is the spin frequency of the pulsar, $\dot{\nu}$ is the frequency derivative, K is a constant of proportionality related to the pulsar's moment of inertia and magnetic field structure, and n is the braking index. Taking the time derivative of equation (2.3) gives the following equation:

$$n = \frac{\nu\ddot{\nu}}{\dot{\nu}^2}, \tag{2.4}$$

where $\ddot{\nu}$ is the second-derivative of the spin frequency. A measurement of n can be made only for the youngest pulsars for which $\ddot{\nu}$ is large enough to be detectable on human timescales. Only nine pulsars have measured braking indices, with values ranging from 0.9 ± 0.2 to 3.15 ± 0.03.

There are probably around 10^8 neutron stars in the Milky Way. This is obtained by estimating the number of stars that have gone supernova in our galaxy. From these 10^8 neutron stars, we estimate that 10^5 are pulsars (with only ~ 2500 discovered), 10^7 are (unseen) dead magnetars, and approximately 10^7 are totally unknown.

There are several ways in which a spinning neutron star may produce a stream of continuous and quasi-periodic gravitational waves:

- **Unstable normal modes**: when neutron stars are young (after being born from a supernova), density waves driven by hydrodynamics and gravity may travel around the star in the opposite direction to its rotation, but dragged forward by the rotation (driven by Coriolis forces). These density waves produce gravitational waves. However, we know now that neutron star viscosity will kill these instabilities, stabilizing the star and turning off the waves, for $T > 10^{10}$ K and $T < 10^{9}$ K. This means that the instability will only operate during the first few years or months of the star's life, when the temperatures are 10^{9} K$< T < 10^{10}$ K. After this time, the unstable modes of the star will not be a good candidate for detection, due to the short-lived emission and the low amplitude of the gravitational waves [37].

- **Free precession**: when a new neutron star enters its final state, the crust crystalizes. The solid crust will assume the axisymmetric shape that centrifugal forces try to maintain. From this point, the crust has a preferred shape. One can define the neutron star deformation ellipticity ϵ_d as the residual ellipticity the star would maintain if it were slowed down to zero frequency without the crust breaking:

$$\epsilon_d \sim 7 \times 10^{-8} (\frac{\nu_{rel}}{\text{kHz}})^2, \tag{2.5}$$

  where ν_{rel} is the spin frequency for which the crust is (most) relaxed. If the star's angular momentum deviates from the symmetry axis of the star, it will precess as it rotates, with a precession angle called θ_w. The neutron star will then emit gravitational waves with an amplitude of:

$$h \sim 10^{-27} (\frac{\theta_w}{0.1 \text{ rad}})(\frac{1 \text{ kpc}}{d})(\frac{f_{rot}}{500 \text{ Hz}})^2, \tag{2.6}$$

  where d is the distance to the source, at a frequency $f_{gw} = f_{rot} + f_{prec}$, where $f_{prec} = \epsilon_d f_{rot}(I_{crust}/I)$ is orders of magnitude smaller than f_{rot}, so f_{gw} is just slightly higher than f_{rot} [38].

- **Asymmetric deformations**: the neutron star can have asymmetries on its surface, like little "mountains" or bumps. These bumps can exist thanks to some mechanisms like accretion in a binary system or the high magnetic field of the star. This asymmetry is quantified with the ellipticity parameter:

$$\epsilon = \frac{I_{xx} - I_{yy}}{I_{zz}}, \tag{2.7}$$

  where the I_{jj} are the inertia moments around the axis, being z the axis of rotation of the neutron star. If the star has this asymmetry, and it is rotating, it will emit gravitational waves at twice the rotation frequency, $f_{gw} = 2f_{rot}$, with amplitude [36]:

$$h_0 = \frac{4\pi^2 G}{c^4} \frac{I_{zz} f_{gw}^2}{d} \epsilon, \tag{2.8}$$

For a typical neutron star, with values of radius $R = 10$ km and mass $M = 1.4M_{\odot}$, the inertia moment is $I_{zz} = \frac{2}{5}MR^2 = 1.1 \times 10^{38}$ kg m^2, called the canonical moment of inertia of neutron stars. With these values, equation (2.8) is:

$$h_0 = 3.25 \times 10^{-5} \frac{f_{gw}^2}{d} \epsilon. \tag{2.9}$$

The value of ϵ is the least known parameter of equation (2.8). The highest expected value for a typical neutron star is of the order $\epsilon \sim 10^{-6}$ (higher values are not supported because of the surface strain tension that the star can maintain [26] and [27]). We can see that with astronomical distances, the value of h_0 becomes very small, being $h_0 \sim 10^{-24}$ a typical value. Upper limits for h_0 have been calculated for different types of continuous wave searches. For the Crab pulsar, we know that h_0 has to be lower than 3.4×10^{-25} (the last upper limit found [28]). This type of emission is almost monochromatic (the frequency is nearly constant), and it has a long duration: it exists as long as the source keeps rotating and an asymmetry exists.

2.2 | Signal coming from a neutron star

As we described in section 2.1, neutron stars can generate gravitational waves through various mechanisms. Independently of this, continuous gravitational waves coming from neutron stars will be nearly periodic - its frequency slows down because of the loss of rotational energy due to the emission of gravitational radiation, the emission of electromagnetic radiation, or the acceleration of particles at the atmosphere. As we said before, the amplitude of a gravitational wave at the detector follows this equation:

$$h(t) = F_+(t)h_+(t) + F_\times(t)h_\times(t), \tag{2.10}$$

where $F_\times$ and F_+ are the antenna beam patterns that we explained in section 1.3.1 (they vary with time because of the Earth motion with respect to the source). For a continuous wave signal, the terms $h_\times$ and h_+ have the form [36]:

$$h_+(t,\tau) = A_+(\tau)\cos\Phi(\tau) \quad \text{and} \quad h_\times(t,\tau) = A_\times(\tau)\sin\Phi(\tau), \tag{2.11}$$

where $\Phi(\tau)$ is the phase evolution of the gravitational wave, which for an isolated neutron star (described in terms of its proper time) is given by:

$$\Phi(t_{NS}) = \phi_0 + 2\pi \sum_{n=0}^{sd} \frac{f_{(n)}^{(NS)}}{(n+1)!} t_{NS}^{n+1}, \tag{2.12}$$

where ϕ_0 is the initial phase, $f_{(0)}^{NS}$ is the instantaneous gravitational wave frequency, $f_{(n)}^{NS}$ $(n > 0)$ are the spin-down parameters in the rest frame of the neutron star at the fiducial start time $t_{NS} = 0$, and sd is the number of spin-down parameters taken into account. In the case of a rotating triaxial-ellipsoid mass distribution (in our case, a neutron star), the functions $A_\times$ and A_+ are given by:

$$A_+ = \frac{1}{2}h_0(1 + \cos^2\iota) \quad \text{and} \quad A_\times = h_0\cos\iota, \tag{2.13}$$

where ι describes the inclination of the source's rotation axis respect to the line of sight (as can be seen in figure 1.7), and h_0 is the amplitude of the gravitational wave, which, recalling equation (2.9), is:

$$h_0 = 3.25 \times 10^{-5} \frac{f_{gw}^2}{d} \epsilon. \tag{2.14}$$

Although the emitted signal is nearly periodic (of constant frequency), the signal that we receive at the detector is modulated in amplitude (due to the antenna pattern functions) as well in frequency (due to the relative motion between the detector and the source):

- The amplitude modulation of the signal is caused by the time dependence of the antenna pattern functions. Because of Earth's rotation and orbital motion, the apparent position of the source in the sky changes, which makes the angles θ and ϕ that appear in the antenna pattern equations (1.39) change with time.
- The frequency modulation is caused by the change of relative velocity between the detector and the source, due to Earth's rotation and its motion with respect to the SSB (Solar System Barycenter), which produces a time-varying Doppler shift in the frequency. We can see an example in figure 2.3.

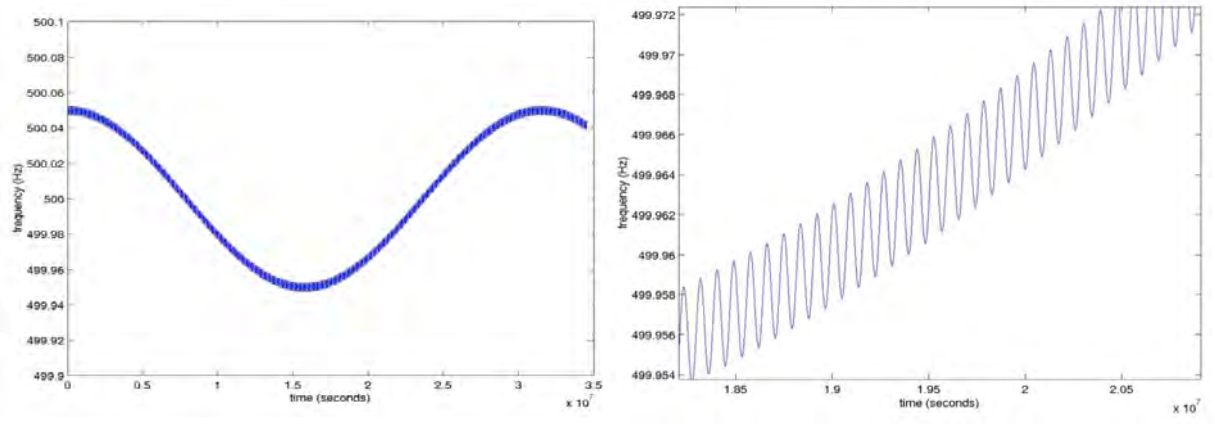

Fig. 2.3: Left panel: frequency modulation due to the change of relative velocity between the Earth and the source. Right panel: zoom of the effect of the left panel. Source: [33].

The instantaneous signal frequency in the detector frame ($2\pi f(t) = d\Phi(t)/dt$) is given to a very good approximation by the non-relativistic Doppler formula[1]:

$$f - \hat{f} = \hat{f} \frac{\vec{v}(t) \cdot \vec{n}(t)}{c}, \tag{2.15}$$

where $\vec{v}(t)$ is the detector velocity in the Solar System Barycenter (SSB) frame, $\vec{n}(t)$ is the unit-vector corresponding to the sky location of the source, and $\hat{f}$ (the frequency emitted at the

[1]Since the velocity of the Earth is approximately a factor 10^{-4} less than c, the non-relativistic formula is a good approximation.

source frame by an isolated neutron star) can be approximated by:

$$\hat{f} = f_0 + \sum_{n=1}^{s} \frac{f_{(n)}}{n!} \left(t - t_0 + \frac{\Delta\vec{r}(t) \cdot \vec{n}(t)}{c} \right)^n , \tag{2.16}$$

where t_0 is the detector time at the start of the observation, $f_{(n)}$ are the spin-down parameters measured in the SSB frame (they don't have to be equal to $f_{(n)}^{(NS)}$) and $\Delta\vec{r}(t) \equiv \vec{r}(t) - \vec{r}(t_0)$, with $\vec{r}(t)$ being the position of the detector in the SSB frame at time t. For semicoherent searches (explained in this chapter) the corrections to the time interval $t - t_0$ are negligible and we can ignore them[2], so the instantaneous frequency at the time t will be given by (if we only use a single spin-down parameter, valid for older neutron stars):

$$\hat{f} = f_0 + \dot{f}(t - t_0). \tag{2.17}$$

Equations (2.15) and (2.17) describe the time-frequency pattern produced by a continuous gravitational wave.

2.3 | Types of continuous searches

The continuous wave LIGO Scientific Collaboration (LSC) group searches for different type of continuous waves coming from neutron stars: known pulsars with well measured timing; other known or suspected isolated neutron stars with limited or no timing information; known or suspected binary neutron star systems; unknown isolated stars in any direction; and unknown binary stars in any direction. We can classify the search of continuous gravitational wave signals in two groups:

- **Targeted searches:** these searches look for gravitational waves coming from pulsars that we have detected electromagnetically. We know the frequency and its evolution (some of its derivatives), the position in the sky, and maybe some other parameters like the distance, the age, the polarisation angle, etc. For these searches, we need very precise ephemerides data for each pulsar, coming from electromagnetic observations. A complete list of known pulsars can be found in [23]. Since we know the parameters of the source, we will not have to deal with the computational problem of the wide-parameter searches. For this reason, the computational cost of the search will be low, and coherent integration of the data for all the observation time is possible.

- **Blind searches:** these searches look for gravitational waves coming from neutron stars that we have not detected electromagnetically. We have to search over an enormous space of parameters, like possible sky locations, frequencies, and frequency derivatives, etc. Since the vast majority of neutron stars that are in the Galaxy have not been discovered yet, this type of search enables us to detect with gravitational waves astronomical objects that

[2] As explained in [29], the Shapiro delay and other relativistic effects are not taken into account because their effect is very small.

we have not discovered yet. Besides of the higher computational cost of blind searches, the large number of templates also reduces the sensitivity compared to a targeted search with the same observation time and false-alarm probability, because increasing the number of templates increases the number of expected false-alarm candidates at a fixed detection threshold. Therefore the detection threshold needs to be raised to maintain the same false-alarm rate, thereby decreasing the sensitivity.

Besides these two types of searches, there are also directed searches with known sky locations but no a priori frequency information of the source. These directed searches aim to detect neutron stars that are not pulsars, like magnetars.

The computational cost depends heavily on the type of search that we want to do. Different methods exist to analyse the data: for a reduced parameter search (the expected computational cost is small), we can use a **coherent method**. Instead, for wide parameter searches (the expected computational cost is big), we don't have enough resources to use a coherent method, so we have to use a **semicoherent method** or a combination of both methods, called a hierarchical method.

Coherent methods are the most sensitive. They use information about the amplitude and the phase of the signal, integrating coherently all the data together. Due to the use of the signal phase information, these methods are not robust towards unpredictable phase variations during the observation time T_{obs} that are not included in the theoretical model of the signal. For wide parameter searches, coherent methods require a great number of templates, which rapidly increases with the observation time. For just one spin-down parameter search, this is [36]:

$$dN_p \propto T_{obs}^5 f^2 d^4\lambda, \tag{2.18}$$

where f is the frequency of the signal and $d^4\lambda$ is the differential region of the parameter space $d^4\lambda = d\Omega \times df \times d\dot{f}$ ($d\Omega$ is the solid angle in a sky region). The computing time for each template grows like $c_p \propto T_{obs}$, and the total computing time ($C_p = N_p c_p$) behaves as:

$$dC_{pc} \propto T_{obs}^6 f^2 d^4\lambda. \tag{2.19}$$

These equations have been calculated for searches that only use one spin-down ($sd = 1$ in equation (2.12)); if more spin-downs are used, the dependence of equation (2.19) with T_{obs} would be of higher order. The computational cost of (2.19) limits the total observation time that we can integrate, being a few days the maximum integration time T_{obs} - even with the best supercomputers that exist in the world. Besides from limiting the observation time, the high number of templates also decreases the sensitivity of the search. If we have more templates, the number of false positives due to noise will also increase, and this will lower the confidence level of the search. To maintain the same confidence level, we must rise the detection thresholds, and for this reason, we are diminishing the sensitivity[3]. Coherent methods are based on **matched**

[3]Incrementing the number of detectors improves the sensitivity likes incrementing T_{obs} does, but the former doesn't increment the number of templates required for the analysis.

filtering: it compares the output of the detector with the expected signal using a scalar product, like the Wiener product. When the two signals coincide, the product is higher, and viceversa. Current coherent methods used in the LIGO and Virgo collaboration are: **Bayesian time domain**, **F-statistics/G-statistics** and 5**-point vector**.

Semicoherent methods are less sensitive than the coherent ones. These methods use information about the frequency evolution of the signal, not about the phase of the signal. These methods split the total observation time T_{obs} in shorter segments of duration T_{coh}, and analyse these short segments coherently. Then, they add incoherently (not having into account the phase information) every one of these segments to obtain the final result. Because of the reduction of the coherent integration time, these methods achieve a drastic reduction of the computational time needed to perform the search (of course, the sensitivity is also reduced). Semicoherent methods can serve as a first approach to detect the signal: if any of these methods report a detection, a fully coherent method analysis would be done to improve and ensure the results. Some of the semicoherent methods that are currently used to search for continuous gravitational waves are **PowerFlux**, and the Hough transform with two different implementations called **Frequency Hough** and **Sky Hough**, which is the method we will use. A comparison between the efficiency of these methods can be found in [39]. The number of templates required for a semicoherent method are (up to first order in equation (2.17)):

$$dN_p \propto T_{obs} T_{coh}^4 f^2 d^4\lambda, \tag{2.20}$$

which for a 30 day (2592000 s) search, with a coherent time of 30 min (1800 s) at a frequency of 1000 Hz would be:

$$dN_p \propto 10^{25} d^4\lambda. \tag{2.21}$$

Following the coherent description, the computational cost would then be:

$$dC_{ps} \propto T_{obs}^2 T_{coh}^4 f^2 d^4\lambda. \tag{2.22}$$

Comparing equations (2.19) and (2.22) we get:

$$\frac{dC_{ps}}{dC_{pc}} \propto \left(\frac{T_{coh}}{T_{obs}}\right)^4. \tag{2.23}$$

Because $T_{coh} < T_{obs}$, it's obvious that the computational cost of the semicoherent methods will be much smaller. To give an example, if the observational time is equal to 30 days and the coherent time is equal to 30 min, the ratio is:

$$\frac{dC_{ps}}{dC_{pc}} \propto \left(\frac{1800}{2592000}\right)^4 = 2.33 \times 10^{-13}. \tag{2.24}$$

CHAPTER 3

HOUGH TRANSFORM

This chapter will describe the Hough transform, the method that we use to analyse LIGO data searching for continuous gravitational wave signals. The Hough transform was created by Paul Hough in 1962 [30]. The original goal of the method was "the recognition of complex patterns and more specifically a method and means for machine recognition of complex lines in photographs or other pictorial representations". The classical Hough transform was concerned with the identification of lines in a image, but later the Hough transform was extended to identifying positions of arbitrary shapes, most commonly circles or ellipses. The Hough transform as it is universally used today was invented by Richard Duda and Peter Hart in 1972, who called it a "generalized Hough transform" [31]. The method was intended to be used for particle physics in order to analyze bubble chamber pictures at CERN, but since then a lot of new implementations have been created [32].

The idea behind the method is simple: parametric shapes in an image are detected by looking for accumulation points in the parameter space. If a particular shape is present in the image, then the mapping of all of its points into the parameter space must cluster around the parameter values which correspond to that shape. We will use the Hough transform in order to look for gravitational wave patterns in the time-frequency space of the data obtained with the ground-based laser interferometers.

3.1 | Example of the Hough transform

We will show the use of the Hough transform in one of the simplest ways: detecting a line, which equation is:

$$y = ax + b, \tag{3.1}$$

where a is called the slope and b is the origin ordinate (where the line intersects the y-axis). We can look at this problem this way: given an a and a b (one point of the parameter space), we

have a line in the $x - y$ plane. The parameters a and b can be used to represent a straight line as single point (a, b) in the parameter space spanned by the two parameters.

There is a problem with a and b: they go to infinity when the line becomes vertical. We want to use another parameters that are bounded. This is accomplished by using a radial distance and an angle as parameters (ρ, θ), instead of a and b. With these new parameters, the equation of a line is now:

$$y = -\frac{\cos\theta}{\sin\theta}x + \frac{\rho}{\sin\theta}, \tag{3.2}$$

which can be rearranged this way:

$$\rho = x\cos\theta + y\sin\theta. \tag{3.3}$$

For each point (x_0, y_0) in the $x - y$ plane we can define a family of lines that go through that point, as can be seen in the left image of figure 3.1, which has three data points in it. Each line is defined by its ρ and θ value (each line is a point in the parameter space), as indicated in the tables of the left image of this figure. If we plot all the possible ρ-θ pairs for a given point we get a sinusoid type of curve (defined by equation (3.3), obtained by calculating the distance of every line to the origin for all the angles between 0 and π), like the ones in the right image of figure 3.1. We can plot this sinusoid curve for every point of our data, and we will obtain a family of curves, shown in the same image. The point where the curves intersect gives a distance and angle, which are the two parameters that we were looking for: the parameters that produced the original line.

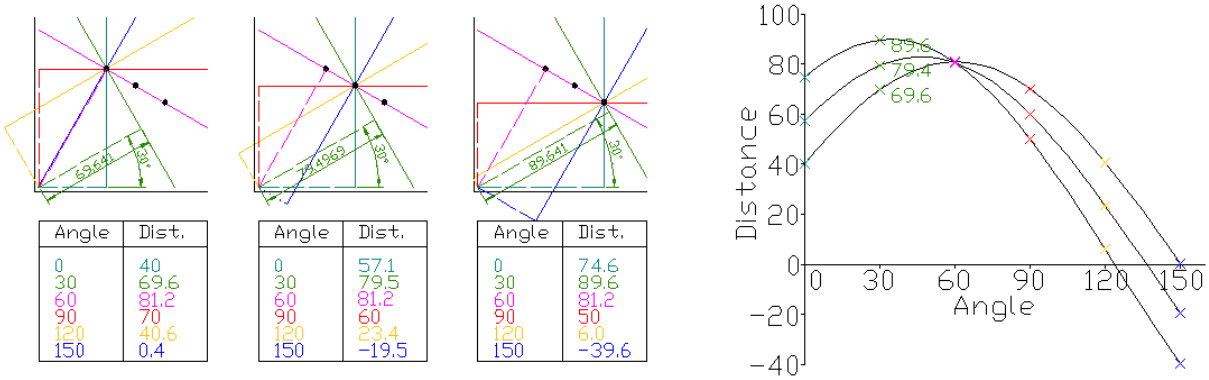

Fig. 3.1: Left image: six lines with different parameters are shown for each of the three data points. Right image: sinusoid curves of each of the three points of figure 3.1 (all angles between 0 and π). Source: https://en.wikipedia.org/wiki/Hough_transform

The Hough number count n is defined as the number of points of the line that a point of the parameter space intersects. In the case of figure 3.1, the number count for the pink is equal to 3. The number count has a maximum value: the total number of points that are used. The parameters that we will accept as our correct result will be the ones that give the highest number count n.

3.2 | The Hough transform for continuous gravitational waves searches

In the gravitational wave searches case, the problem is not so simple as detecting an analytic straight line. We have some extra problems:

- Presence of noise in the data
- Finite resolution (parameter space is discrete, not continuous)
- A lot of parameters to search (in the case of blind searches), and finite computational assets
- More data points, not just three as in the example of the previous section

These difficulties imply that we need to redefine some concepts about the Hough transform that we explained in the example of the last section. In the previous section, our parameter space was (ρ, θ), and the parametrized curve we were looking was a straight line. While using the Hough transform in the search for continuous gravitational waves, we will use a different parameter space, composed of frequency, spin-down, right ascension and declination $(f, \dot{f}, \alpha, \delta)$, and the curve we will be looking for is defined in equation (2.15), which is defined in the frequency-time plane. The other parameters of the signal (ι, ψ, h_0 and ϕ_0) do not affect the "shape" of the gravitational wave signal, so in the Hough search we are only interested in the frequency, spin-down, right ascension and declination of the source. Each point of the parameter space produces a different curve in the frequency-time plane, as those in figure 2.3. From our data and each frequency-time curve belonging to a different point in parameter space we will calculate the Hough number count n as explained later in this chapter. The Hough method is sensitive to periodic signals from any type of gravitational wave source that produces a pattern in the frequency-time plane described by equation (2.15). It is only in the case we want to estimate sensitivities or set upper limits on the amplitude of the signal (h_0) when we will assume a triaxial neutron star emitting at twice the rotational frequency.

The next steps are followed in order to implement the Hough search:

1. First of all, we break up the data - of duration T_{obs} (observation time) - in N segments of a certain duration, called T_{coh} (coherent time). We can label the different segments by $a = 0, 1, N-1$ and denote the start time of each segment by t_a (known as the time stamp of the a^{th} segment). Each segment consists of M data points, which are related to the *sampling rate* of the detector (16452 Hz for LIGO[1]). The a^{th} segment covers the time interval $[t_a, t_a + T_{coh}]$. Let $x(t)$ be he detector output which is sampled at times

[1]The sampling theorem states that discretely sampled data with sampling rate f_s can completely represent a continuous signal which only has frequency content below the Nyquist frequency ($f_{nyq} = f_s/2$). With a sampling rate of 16452 Hz, we can represent the signals of our interest without aliasing problems.

$t_j = t_a + j\Delta t$ with $j = 0, 1, ..., M-1$. Here the data segment has been subdivided into M sub-segments with the times t_a defined to be at the start of each sub-segment; this implies $\Delta t = T_{coh}/M$, which is equal to the sampling rate of the detector. We call x_j the sequence of data points obtained, where $x_j \equiv x(t_j)$.

Before calculating the discrete Fourier transform of our time series, some windowing is applied to it. Windowing means that the time series to be transformed is multiplied by a window function, which promises to produce a clearer spectral representation of the signal. So instead of x_j, we transform $x_j w_j$, where w_j are the discrete points of some window function (what we call x_j from now on is equal to $x_j w_j$). In our case, we apply the a top flat window function named Tukey. Further explanations and definitions can be found in [41] and [42].

2. The second step is to compute the Fourier transform of each data segment to obtain N SFTs. The discrete Fourier transform is defined as:

$$\tilde{x}_k = \Delta t \sum_{j=0}^{M-1} x_j e^{-2\pi i j k/M}, \tag{3.4}$$

where $k = 0, 1, ..., M-1$. For $0 \leq k \leq [M/2]$, the frequency index k corresponds to a physical frequency of $f_k = k/T_{coh}$, with [.] denoting the integer part of a given real number. The values $[M/2] < k \leq M-1$ correspond to negative frequencies given by $f_k = (k-M)/T_{coh}$. We have a number N of SFT's for each detector (N is usually a different number for each detector). As we explained in the first chapter, not all the time of observation can be used to search gravitational waves, due to disturbances and errors of the detector. For this reason, N is usually not equal to T_{obs}/T_{coh}, but instead it is a lower number. We use a factor Δt in equation (3.4), because we want $\tilde{x}_k$ to have the same units as the continuous case.

3. The next step is to whiten the data. The detector output $x(t)$ at any time t is the sum of the noise $n(t)$ and a possible gravitational wave signal $h(t)$:

$$x(t) = n(t) + h(t). \tag{3.5}$$

We suppose the noise $n(t)$ to be a stochastic process, stationary, and Gaussian with zero mean. In the continuous case, when the observation time is infinite, the single sided power spectral density (PSD) $S_n(f)$ for $f > 0$ is defined as the Fourier transform of the autocorrelation function:

$$S_n(f) = 2\int_{-\infty}^{\infty} \langle n(t)n(t+\tau)\rangle e^{-2\pi i f\tau} d\tau, \tag{3.6}$$

where $\langle ... \rangle$ denotes the ensemble average, and τ represents the time difference between two measures of $n(t)$. This equation only holds for stationary noise[2] (reference [47] explains

[2]If the noise wasn't stationary, the autocorrelation function wouldn't depend only on τ (the time difference between measures), it would depend also on the time t that the measure was done.

one possible test of this stationarity assumption). For interferometric detectors, $S_n(f)$ is a function of frequency because of the coloured nature of the noise.

It can be shown that $\langle|\hat{n}_k^2|\rangle$ (where $\hat{n}_k^2$ is the Fourier transform of the detector's noise output) is related to the PSD (power spectral density):

$$\langle|\hat{n}_k^2|\rangle \approx \frac{M\Delta t}{2} S_n(f_k) = \frac{T_{coh}}{2} S_n(f_k). \tag{3.7}$$

For many data analysis purposes, it is very useful to use whitened data. Whitening the data is normalising the power $\hat{x}_k^2$ of a frequency bin by the expected value in the case of having just noise (which is $\langle|\hat{n}_k^2|\rangle$):

$$\rho_k = \frac{|\hat{x}_k^2|}{\langle|\hat{n}_k^2|\rangle}, \tag{3.8}$$

where ρ_k is a measure of the power of the signal weighted by the noise (it is a dimensionless quantity). Using equation (3.7), equation (3.8) can be rewritten as:

$$\rho_k = \frac{2|\hat{x}_k^2|}{T_{coh} S_n(f_k)}. \tag{3.9}$$

4. The fourth step consists on creating a peak-gram of our data. After whitening, the N SFTs are digitized by setting a threshold ρ_{th} (that we call peak threshold) on the normalized power ρ_k. A frequency bin is then selected if $\rho_k > \rho_{th}$, and rejected otherwise. In this way, each SFT is replaced by a collection of zeros and ones called **peak-gram**:

$$n_k = \begin{cases} 1 & \text{if} \quad \rho_k > \rho_{th} \\ 0 & \text{if} \quad \rho_k < \rho_{th}, \end{cases} \tag{3.10}$$

as we can see in the right panel of figure 3.2. This is the simplest method of selecting frequency bins, for which the optimal choice of the peak threshold ρ_{th} will be discussed in subsection 3.4.4. The gravitational wave signal is assumed to be concentrated in a single frequency bin for each SFT, because of he choice that we have made of T_{coh}. In order to maximize the efficiency, this value should be the longest possible, but compatible with the power of the signal being concentrated in a single frequency bin for each SFT. We will discuss the limits of T_{coh} in section 3.4.

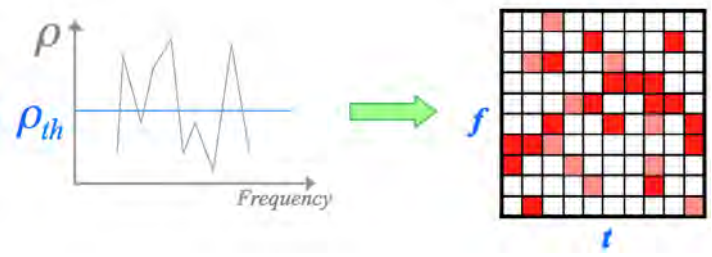

Fig. 3.2: The left plot shows the power versus the frequency; the right plot shows a peak-gram. If a frequency bin has a power greater than the threshold that we have set, it is selected (shown as the red squares in the right image). Each vertical slice (time direction) represents a different SFT, and each horizontal slice (frequency direction) represents a different frequency bin. Source: Alicia Sintes.

5. The last step consists on calculating the Hough number count n of every different combination of parameters $(f, \dot{f}, \alpha, \delta)$. The Hough transform is used to map points from the time-frequency plane of our data (understood as a sequence of peak-grams) into the space of the source parameters. Each point in parameter space corresponds to a pattern in the time-frequency plane, and the Hough number count, n, is the weighted sum of the ones and zeros (n_i^k, where the index i referes to the i^{th} SFT) of the different peak-grams along this curve. For the "weighted Hough" this sum is computed as:

$$n = \sum_{i=0}^{N} w_i^k n_i^k, \tag{3.11}$$

where n_i is either 0 or 1 (as we saw in equation (3.10)), and the weights are normalized according to:

$$\sum_{i=0}^{N} w_i = N. \tag{3.12}$$

The weights are defined by [45]:

$$w_i^k \propto \frac{(F_i^{+1/2})^2 + (F_i^{\times 1/2})^2}{S_i^k}, \tag{3.13}$$

where $F_i^{+1/2}$ and $F_i^{\times 1/2}$ are the values of the beam pattern functions at the mid point of the i^{th} SFT, and S_i^k is the value of the single-sided PSD at frequency bin k of the i^{th} SFT. When $\forall w_i = 1$, we obtain the "standard Hough". The "weighted Hough" can improve the sensitivity of the search taking into account the possible non-stationarities of the detector noise, the amplitude modulation due to the motion of the detector and it can also allow for multi-interferometer searches.

3.3 | Statistical properties of the Hough search

As described in [33], in this section we will summarise the statistical properties of the Hough search method. The frequency bins that are fed into the Hough transform are the ones whose normalised power ρ_k defined in equation (3.8) exceeds a threshold ρ_{th}. Assuming that the noise is stationary, has zero mean, and is Gaussian, from (3.8) we get:

$$2\rho_k = z_1^2 + z_2^2, \tag{3.14}$$

where

$$z_1 = \frac{\sqrt{2}\mathrm{Re}[\hat{x}_k]}{\sqrt{\langle|\hat{n}_k|^2\rangle}} \qquad \text{and} \qquad z_2 = \frac{\sqrt{2}\mathrm{Im}[\hat{x}_k]}{\sqrt{\langle|\hat{n}_k|^2\rangle}}. \tag{3.15}$$

As we said in the previous section, the detector output $\hat{x}_k$ is the sum of noise and a possible signal: $\hat{x}_k = \hat{n}_k + \hat{h}_k$. Assuming that $\mathrm{Re}[\hat{n}_k]$ and $\mathrm{Im}[\hat{n}_k]$ are independent random variables with equal variance, it is easy to show that their variance must be equal to $\langle|\hat{n}_k|^2\rangle/2$. Therefore, taking the noise to be Gaussian, it follows that the random variables z_1 and z_2 follow a Gaussian

distribution with unit variance (but nonzero mean). Thus, $2\rho_k$ must be distributed according to a noncentral χ^2 distribution with 2 degrees of freedom with non centrality parameter λ_k:

$$\lambda_k = (\mathbf{E}[z_1])^2 + (\mathbf{E}[z_2])^2 = \frac{4|\hat{h}(f_k)|^2}{T_{coh}S_n(f_k)}, \tag{3.16}$$

where $\mathbf{E}[...]$ denotes the expected value of the quantity inside [ ]. Thus, the distribution of ρ_k is:

$$p(\rho_k|\lambda_k) = 2\chi^2(2\rho_k|2\lambda_k) = \exp(-\rho_k - \frac{\lambda_k}{2})I_0(\sqrt{2\lambda_k\rho_k}), \tag{3.17}$$

where I_0 is the modified Bessel function of zeroth order. As expected, $p(\rho_k|\lambda_k)$ reduces to the exponential distribution in the absence of a signal (when $\lambda_k = 0$).

The mean and variance for this distribution are respectively:

$$\mathbf{E}[\rho_k] = 1 + \frac{\lambda_k}{2} \qquad \text{and} \qquad \sigma^2[\rho_k] = 1 + \lambda_k. \tag{3.18}$$

The probability η that a given frequency bin is selected is:

$$\eta(\rho_{th}|\lambda_k) = \int_{\rho_{th}}^{\infty} p(\rho_k|\lambda_k)d\rho_k. \tag{3.19}$$

The false alarm and false dismissal probabilities for the frequency bin selection are respectively:

$$\alpha(\rho_{th}) = \int_{\rho_{th}}^{\infty} p(\rho_k|0)d\rho_k = e^{-\rho_{th}} \tag{3.20}$$

$$\beta(\rho_{th}|\lambda_k) = 1 - \eta(\rho_{th}|\lambda_k) = \int_{0}^{\rho_{th}} p(\rho_k|\lambda_k)d\rho_k. \tag{3.21}$$

The false alarm gives the probability that a frequency bin is selected when no signal is present; the false dismissal gives the probability that a frequency bin is not selected when a signal is present. A visualisation of α and β can be seen in figure 3.3. Clearly, $\eta = \alpha$ when no signal is present and η becomes larger when the signal becomes stronger and $\eta \to 1$ when $\lambda \to \infty$.

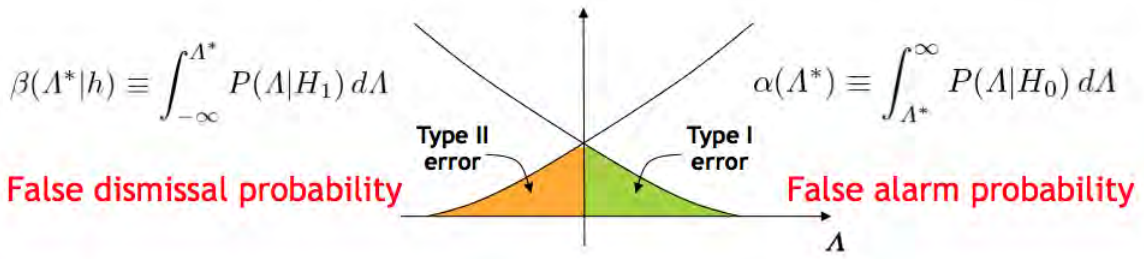

Fig. 3.3: Visualization of the false alarm (α) and false dismissal (β). The green area shows the tail of H_0 (no signal present) passing the threshold imposed (in our case it is ρ_{th}), which integrated is the false alarm probability; the orange area shows the tail of H_1 (a signal is present) passing the threshold, which integrated is the false dismissal probability. Source: Alicia Sintes.

For small λ_k, $\eta(\rho_t h|\lambda_k)$ can be expanded:

$$\eta(\rho_{th}|\lambda_k) = \alpha\left[1 + \frac{\rho_{th}}{2}\lambda_k + \mathcal{O}(\lambda_k^2)\right]. \tag{3.22}$$

This expansion will be very useful when we restrict ourselves to the case of small signals.

Starting from N SFTs, the probability distribution $p(n)$ of measuring a number count n in a pixel of a Hough map is given by:

$$p(n|\lambda_{th},\lambda) = \binom{N}{n}\eta^n(1-\eta)^{N-n}, \tag{3.23}$$

with mean $\bar{n} = N\alpha + \frac{\alpha\rho_{th}}{2}\sum_{i=1}^{N} w_i\lambda_i$ and variance $\sigma^2 = \sum_{i=1}^{N} w_i^2\eta_i(1-\eta_i)$. In the absence of a signal ($\eta = \alpha$), this distribution becomes:

$$p(n|\lambda_{th},0) = \binom{N}{n}\alpha^n(1-\alpha)^{N-n}, \tag{3.24}$$

with mean $\bar{n} = N\alpha$ and variance $\sigma^2 = \alpha(1-\alpha)\sum_{i=1}^{N} w_i^2$. Although n is a discrete variable, we can take it as a continuous variable, and we can approximate the previous binomial distribution by a Gaussian distribution (for the case of large number of SFTs N), to simplify the problem and study some analytical properties:

$$p(n|\lambda_{th},\lambda) = \frac{1}{\sqrt{2\pi\sigma^2}}\exp -(\eta - N\eta)^2/2\sigma^2. \tag{3.25}$$

Candidates for further analysis are selected by setting a threshold n_{th} on the number count. Based on this, we can redefine the false alarm and false dismissal probabilities:

$$\alpha_H(n_{th},\rho_{th},N) = \sum_{n=n_{th}}^{N} p(n|\rho_{th},0), \tag{3.26}$$

$$\beta_H(n_{th},\rho_{th},\lambda,N) = \sum_{n=0}^{n_{th}-1} p(n|\rho_{th},\lambda). \tag{3.27}$$

These two quantities determine the significance and the sensitivity of the Hough search.

Because the weights w_i vary for different sky locations, we should not compare number counts directly. Instead, we should use another detection statistic: the **significance** of a number count. The significance s (also know as critical ratio) of the observed number count n is defined as:

$$s = \frac{n - < n >}{\sigma}, \tag{3.28}$$

where $< n >$ and σ are the expected mean and standard deviation for pure noise. Values of s can be compared directly across different templates characterized by differing weight distributions. In the Gaussian approximation, the relation between the number count threshold and the false alarm probability is given by:

$$n_{th} = N\alpha + \sqrt{2\sum_{i=0}^{N-1} w_i^2\alpha(1-\alpha)}\,\mathrm{erf}^{-1}(2\alpha_H), \tag{3.29}$$

while the relation between the significance and the false alarm probability is:

$$s_{th} = \sqrt{2}\,\mathrm{erf}^{-1}(2\alpha_H). \tag{3.30}$$

We will use this threshold at the post-processing stage of our analysis.

3.4 | Setting up the Hough search parameters for continuous gravitational waves

3.4.1 | Bounds of the coherent time

The coherent time T_{coh} cannot be arbitrarily large, because we would like the signal power to be concentrated in a single frequency bin during the SFT duration (which is T_{coh}), but the signal frequency is changing in time due to the Doppler modulation and also due to the spin-down of the star. If $\dot{f}$ is the time derivative of the signal frequency at any given time, and knowing that the resolution in frequency (the "length" of a frequency bin) is $\delta f = 1/T_{coh}$, in order for the signal not to shift by more than half a frequency bin we must have $|\dot{f}|T_{coh} < (2T_{coh})^{-1}$, i.e.:

$$T_{coh} < \sqrt{\frac{1}{2|\dot{f}|_{max}}}, \tag{3.31}$$

where by $|\dot{f}|_{max}$ we mean the maximum possible value of $|\dot{f}|$ for all allowed values of the parameters. We shall assume that the Doppler modulation due to Earth's rotation is the dominant effect, over the spin-down of the star[3]. Thus we can estimate $\dot{f}$ by keeping $\hat{f}$ fixed and differentiating $\vec{v}(t)$ in equation (2.15):

$$\dot{f} \approx \frac{\hat{f}}{c}\frac{dv}{dt} \cdot n \leq \frac{\hat{f}}{c}\left|\frac{dv}{dt}\right|. \tag{3.32}$$

The important contribution to the acceleration dv/dt comes from the daily rotation of the Earth:

$$|\dot{f}|_{max} = \frac{\hat{f}}{c}\frac{v_e^2}{R_e} = \frac{\hat{f}}{c}\frac{4\pi^2 R_e}{T_e^2}, \tag{3.33}$$

where v_e is the magnitude of Earth's velocity around its axis, T_e is the length of one day and R_e is the radius of the Earth. Substituting values we get:

$$T_{coh} < \sqrt{\frac{cT_e^2}{2\hat{f}4\pi^2 R_e}} = 50\text{min} \times \sqrt{\frac{500\text{ Hz}}{\hat{f}}}. \tag{3.34}$$

As we have already pointed out, we will be using $T_{coh} = 30$ min.

3.4.2 | Bounds and resolution of spin-down parameters

We can calculate a rough estimation of the resolution of the spin-down parameters by estimating the minimum necessary slope in equation (2.17) that is needed for the frequency to change at least one bin in a total time T_{obs}. Rewriting that equation we have:

$$f - f_0 = \dot{f}(t - t_0), \tag{3.35}$$

which we can rearrange by noting that for a change in a frequency bin, $f - f_0$ is equal to δf, the resolution in frequency (which is equal to T_{coh}) and that $t - t_0$ is equal to T_{obs} if this change of one bin happens during all the observational time. Now, we can rewrite the previous equation:

$$\delta f = \dot{f} T_{obs}. \tag{3.36}$$

[3]This approximation impplies an upper bound on the value of the spin-down parameters that we can search over.

We can see that the minimum slope necessary to detect a change of one frequency bin is equal to:

$$\delta\dot{f} = \frac{\delta f}{T_{obs}} = \frac{1}{t_{coh}T_{obs}}. \tag{3.37}$$

If instead of having the only first spin-down in equation (2.17), we had only the second spin-down ($f - f_0 = \frac{1}{2}\ddot{f}(t - t_0)^2$), the minimum necessary slope would be:

$$\delta\ddot{f} = 2\frac{\delta f}{T_{obs}^2} = \frac{2}{T_{coh}T_{obs}^2}. \tag{3.38}$$

We can generalise this equation to give the resolution of the spin-down parameters at any order:

$$\delta f_{(n)} = n!\frac{\delta f}{T_{obs}^n} = n!\frac{1}{T_{coh}T_{obs}^n}. \tag{3.39}$$

As an example, we can calculate the resolution for the first spin-down parameter:

$$\delta f_{(1)} = (2.1 \times 10^{-10}\ \text{Hz/s}) \times \frac{30\ \text{days}}{T_{obs}} \cdot \frac{1800\ \text{s}}{T_{coh}}. \tag{3.40}$$

We have to choose the range of values $-f_{(n)}^{max} < f_{(n)} < f_{(n)}^{max}$ and the number sd of spin-down parameters to be searched over. Assuming equation (2.16), we get:

$$f_{(n)}^{max} = n!\frac{\hat{f}_{max}}{\tau^n}, \tag{3.41}$$

where τ is the age of the pulsar and $\hat{f}_{max}$ is the largest intrinsic frequency that we search over. We include the n^{th} spin-down parameter in our search only if the resolution defined by equation (3.39) is not too coarse compared to $f_{(n)}^{max}$:

$$\delta f_{(n)} < f_{(n)}^{max}. \tag{3.42}$$

Since $T_{obs} \ll \tau$, $f_{(n)}^{max}$ decreases with increasing n much faster than $\delta f_{(n)}$. This implies that there must exist a value sd_{max} such that equation (3.42) is satisfied for all $n \leq sd_{max}$ and is violated for all $n > sd_{max}$. Any spin-down parameter of order greater than sd_{max} does not significantly affect the result of the Hough transform. As an example, if we wish to search for pulsars whose age is at least $\tau = 40$ years, and for $\hat{f}_{max} = 1000$ Hz, we get $sd_{max} = 3$.

On the other hand, computational limitations might dictate that we can only search over, say, one spin-down parameter. This sets a lower limit on the age of the pulsar that we can search over because the second spin-down parameter must satisfy $\delta f_{(2)} > f_{(2)}^{max}$ which leads to:

$$\tau > 155\ \text{yr} \times \frac{T_{obs}}{30\ \text{days}} \cdot \left(\frac{\hat{f}_{max}}{1000\ \text{Hz}} \cdot \frac{T_{coh}}{1800\ \text{s}}\right)^{1/2}. \tag{3.43}$$

Finally, the finite length of T_{coh} itself leads to a lower bound on τ. If $f_{(n)}$ is too large, then the signal power may no longer be concentrated in a single frequency bin, and the assumption of neglecting spin-down parameters which was used to derive equation (3.34) will no longer be

valid. To be certain that the spin-down will not cause the signal to move by more than half a frequency bin, we must have $f_{(n)}^{max} T_{coh}^{n} < \frac{n!\delta f}{2}$ which implies:

$$\tau > \left(\frac{2\hat{f}_{max} T_{coh}^{n+1}}{n!} \right)^{1/n}. \tag{3.44}$$

The most stringent limit is obtained for $n = 1$:

$$\tau > 103 \text{ yr} \times \frac{\hat{f}_{max}}{1000 \text{ Hz}} \left(\frac{T_{coh}}{1800 \text{ s}} \right)^2. \tag{3.45}$$

The ranges of $\dot{f}$ are determined by the computational cost, as well as by the low probability of finding an object with $|\dot{f}|$ higher than the values searched — in other words, the ranges of $\dot{f}$ are narrow enough to complete the search in a reasonable amount of time, yet wide enough to include likely signals. All known isolated pulsars spin down more slowly than the two values of $|\dot{f}|_{max}$ used here, and as seen in the results section, the ellipticity required for higher $|\dot{f}|$ is improbably high for a source losing rotational energy primarily via gravitational radiation at low frequencies. A small number of isolated pulsars in globular clusters exhibit slight spin-up, believed to arise from acceleration in the Earth's direction: this is why we use also positive values for $\dot{f}$.

3.4.3 | Resolution of the sky grid

To find the resolution of the sky grid, let's consider the following: if we keep the values of f_0 and $\dot{f}$ constant in equation (2.15), the values of $\vec{n}(t)$ consistent with an observation $f(t)$ must satisfy that:

$$\vec{v}(t) \cdot \vec{n} = v(t) n \cos\phi \rightarrow \cos\phi = \frac{\vec{v}(t) \cdot \vec{n}}{v(t) n} = \frac{c}{v(t)} \frac{f(t) - \hat{f}(t)}{\hat{f}(t)}, \tag{3.46}$$

where in the last step we have used that $n = 1$ (unitary vector). ϕ is the angle between $\vec{n}$ and $\vec{v}(t)$. This implies that ϕ must be constant (the set of sky positions consistent with an observation $f(t)$ form a circle in the celestial sphere, centered around the vector $\vec{v}$). If the frequency of a bin is contained between $(f_k - \frac{1}{2}\delta f,\ f_k + \frac{1}{2}\delta f)$ the set of points consistent with an observation must correspond to an annulus of width $\delta\phi$ which is:

$$\delta\phi \approx \frac{c}{v} \frac{\delta f}{\hat{f} \sin\phi}. \tag{3.47}$$

We can find the lower limit of this width by setting $\phi = \pi/2$:

$$(\delta\phi)_{min} = \frac{c}{v \hat{f} T_{coh}} = 0.01 \text{ rad } \times \left(\frac{1800 \text{ s}}{T_{coh}}\right)\left(\frac{500 \text{ Hz}}{\hat{f}}\right)\left(\frac{10^{-4}}{v/c}\right). \tag{3.48}$$

We can also find the higher limit of the width by setting $\sin\phi \approx \phi \approx (\delta\phi)_{max}$:

$$(\delta\phi)_{max} = \sqrt{\frac{c}{v \hat{f} T_{coh}}} = 0.11 \text{ rad } \times \left(\frac{1800 \text{ s}}{T_{coh}}\right)^{1/2}\left(\frac{500 \text{ Hz}}{\hat{f}}\right)^{1/2}\left(\frac{10^{-4}}{v/c}\right)^{1/2}. \tag{3.49}$$

We can choose the final pixel size $\delta\theta$ of the grid to be some fraction of $(\delta\phi)_{min}$:

$$\delta\theta = \frac{1}{\frac{v}{c}\hat{f}P_f T_{coh}} \sim \frac{10^4}{fP_f T_{coh}}, \tag{3.50}$$

where P_f is the pixelfactor, a number that we can choose to make the sky grid thicker or thinner.

3.4.4 | Peak threshold

As explained in section 3.2, ρ_k (equation (3.8)) is a measure of the power of the signal weighted by the noise. After whitening, the N SFTs are digitized by setting a threshold ρ_{th} (the peak threshold) on ρ_k. The k_{th} frequency bin is then selected if $\rho_k > \rho_{th}$, and rejected otherwise.

The value that we select for ρ_{th} will affect the efficiency of our search. If we increase ρ_{th}, less frequency bins will be selected and the number count n will also decrease. This is a double-edged sword: the computational cost will decrease (the analysis will be faster), and less signals coming from noise will increase the false alarm rate. But if a real signal with low ρ_k reaches the detector, and we have set a high value of ρ_{th}, this signal will not pass the threshold and we will lose the gravitational wave event. For this reason, finding the optimal ρ_{th} is an important task.

For the standard Hough (in which the weights are not taken into account), it is possible to obtain the theoretical optimal value for ρ_{th}. We present two criteria (taken from [33]) that yield the same result for small signals, large N and for the standard Hough:

- **Maximizing the critical ratio**: we can define a random variable called the critical ratio as:

  $$\Psi = \frac{n - N\alpha}{\sqrt{N\alpha(1-\alpha)}}. \tag{3.51}$$

  This quantity is a measure of the significance of a measured value n with respect to the expected value $N\alpha$ in the absence of any signal, weighted by the expected fluctuations of the noise. In the presence of a signal, the expected value of the critical ratio is:

  $$\bar{\Psi} = \frac{N\eta - N\alpha}{\sqrt{N\alpha(1-\alpha)}}, \tag{3.52}$$

  where η and α depend on the threshold ρ_{th} according to equations (3.20) and (3.21). The criterion for choosing the threshold is to maximize $\bar{\Psi}(\eta, \alpha)$ with respect to ρ_{th}. In the case of small signals where $\eta \sim \alpha(1 + \rho_{th}\lambda/2)$, the condition is:

  $$\frac{\partial\bar{\Psi}}{\partial\rho_{th}} = 0, \tag{3.53}$$

  that leads to:

  $$\ln\alpha = 2(\alpha - 1), \tag{3.54}$$

  which yields $\rho_{th} \sim 1.6$ ($\alpha \sim 0.20$).

- **The Neyman-Pearson criterion**: in this case, we want to minimize the false dismissal rate β_H for a given value α_H^* of the false alarm rate. For weak signals, this requirement uniquely determines ρ_{th} and agrees with the previous criterion. Taking N and λ to be fixed parameters, this is the procedure:

  1. Choose a value α_H^* for the largest false alarm rate α_H that we can allow.
  2. Invert the equation $\alpha_H(\rho_{th}, N, n_{th}) \leq \alpha_H^*$ to obtain $n_{th}(\rho_{th}, N, \alpha_H^*)$.
  3. Substitue the value of n_{th} thus obtained in the expression for the false dismissal $\beta_H(n_{th}, \rho_{th}, \lambda, N)$. This gives β_H as a function of $(\rho_{th}, \lambda, N, \alpha_H^*)$.
  4. Minimize β_H as a function ρ_{th}. Let ρ_{th}^* be the value that minimizes β_H.
  5. Using $n_{th}(\rho_{th}, N, \alpha_H^*)$, obtain $n_{th}^* = n_{th}(\rho_{th}^*, N, \alpha_H^*)$.

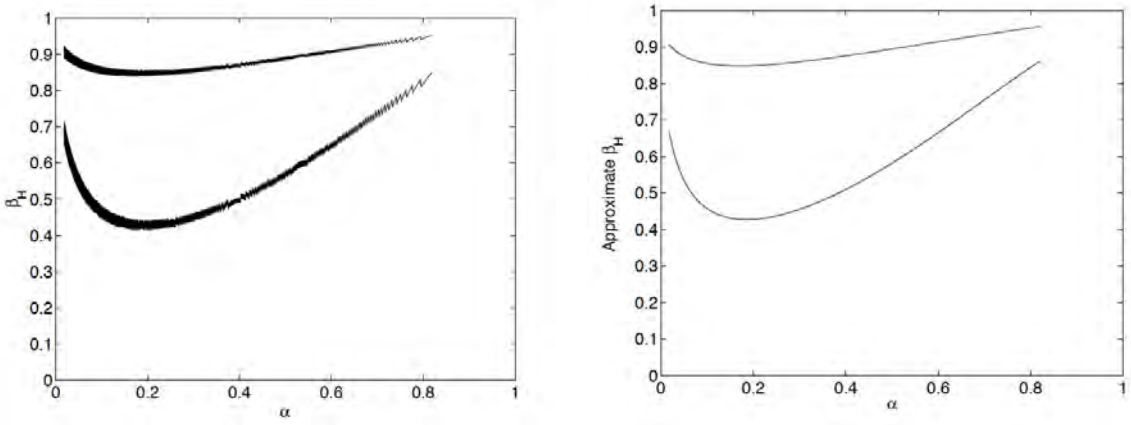

Fig. 3.4: Left panel: false dismissal rate as a function of the false alarm rate ($\alpha = e^{-\rho_{th}}$) for a non-centrality parameter $\lambda = 0.1$ (upper curve) and $\lambda = 0.2$ (lower curve), $N = 1000$ and $\alpha_H = 0.01$. The minimum of each curve occurs at $\alpha = 0.20$ approximately, corresponding to a $\rho_{th} = 1.6$ threshold. Right panel: same parameters as the left panel, used to calculate a Gaussian approximation to β_H, giving roughly the same minimum as the left panel. Source: [33].

The optimal value for ρ_{th} appears to be 1.6, but both analysis were done under several assumptions: small signal, large N and that we are using the Hough search without weights. For a real search, these approximations may not be valid. For this reason, we want to the search using other values for ρ_{th} and see how the efficiency and the computational cost for the search changes. This analysis is done in chapter 4.

3.5 | The χ^2 veto

The significance s of the Hough continuous search indicates the "importance" of a candidate in the toplists. But this value can also be high due to instrumental or environmental artefacts that are present in the data (noises explained in section 1.3). The toplists (a text file containing the parameters of each candidate and their significance value) coming out from the Hough search

may contain candidates of no astrophysical origin, but how can we distinguish them from the signals that we are searching? One of the most important features of continuous signals is that they should accumulate their significance fairly equally during all the time that we measure the signal. We can test this property with the χ^2 veto.

The χ^2 statistical distribution is used to test the goodness of fit of a given distribution to a theoretical one. The probability distribution function of a χ^2 distribution with p degrees of freedom is:

$$f(x) = \frac{1}{2^{p/2}\Gamma(p/2)} x^{p/2-1} e^{-x/2} \quad \text{for} \quad x > 0, \tag{3.55}$$

with mean $\langle x \rangle = p$ and standard deviation $\sigma = \sqrt{2p}$. In figure 3.5 we can see different probability distribution functions. It can be seen that when p is bigger, bigger values of χ^2 have more probability.

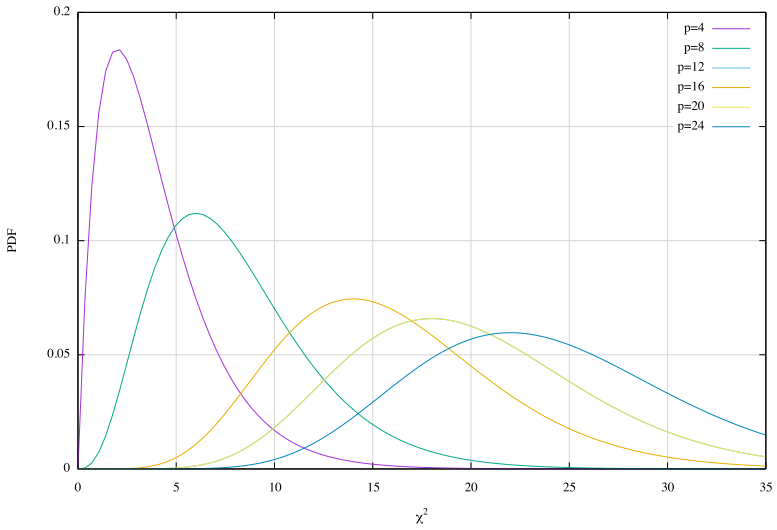

Fig. 3.5: Probability distribution function (PDF) versus χ^2 for some χ^2 distributions with different values of p.

The χ^2 test is a measure of consistency of the signal. For a continuous gravitational wave signal, we expect that the number count of the Hough transform raises linearly with time: because the signal is continuous, no segment of data should contribute more than any other segment to the total number count. For this reason, we can divide our data into p non-overlapping segments, and check if the number count of every segment is consistent with the other number counts. Each of these segments contains a number of SFTs $(N_1, N_2, ...N_p)$ such that the total sum is:

$$\sum_{j=1}^{p} N_j = N. \tag{3.56}$$

Also, for the number count, we get:

$$\sum_{j=1}^{p} n_j = n, \tag{3.57}$$

where n is the total number count for a point in the parameter space and n_j is the number count of each of the different p segments. Small values of the χ^2 test are consistent with the hypothesis that the observed significance arose from a detector output which was a linear combination of Gaussian noise and the continuous gravitational wave signal. Large values of the χ^2 test indicate either that the signal did not match the template or that the detector noise was non-Gaussian[4].

We can define the χ^2 discriminator of the Hough search (as it was done in [43]) as:

$$\chi^2(n_1, n_2, ..., n_p) = \sum_{j=1}^{p} \frac{(n_j - nN_j/N)^2}{N_j \eta(1-\eta)}, \tag{3.58}$$

that, for the weighted Hough, is:

$$\chi^2(n_1, n_2, ..., n_p) = \sum_{j=1}^{p} \frac{(n_j - \sum_{i\in I_j} w_i/N)^2}{\eta(1-\eta)\sum_{i\in I_j} w_i^2}, \tag{3.59}$$

where I_j is the set of SFTs indices for each different p chunks, and $\eta = n/N$. This corresponds to a χ^2 distribution with $p-1$ degrees of freedom. One can choose any number of p segments, but we want to keep a balance between choosing too few (we can't check if the signal accumulates properly), and too many. After fixing p, we split the SFT data in such a way that the sum of the weights in each block satisfies:

$$\sum_{i\in I_j} w_i = \frac{N}{p}. \tag{3.60}$$

The χ^2 veto will be able to remove persistent line noises. It eliminates lines that are continuous but that don't follow the Doppler pattern that we search. It works very well at removing violin modes, calibration lines and periodic narrow-band combs.

[4]We will discuss later the threshold of the χ^2 test that distinguishes a big or small value.

Part II

Experimental results

The following two chapters describe the characterization of two different aspects of the Hough all-sky search: chapter 4 will describe the characterization of the peak threshold ρ_{th} using data from the S6 science run, and chapter 5 will describe the characterization of the χ^2 veto curve using data from the O1 science run. A comparison between the duration, the best sensitivity and the number of SFTs of $T_{coh} = 30$ min of these two science runs can be seen in the following table:

Run	**Start-End date**	**Best sensitivity** $\sqrt{S_n}$ $[1/\sqrt{\mathbf{Hz}}]$	**Number of SFTs**	
			H1	**L1**
S6	Jul 8, 2009 - Oct 17, 2010	$\sim 10^{-23}$	10124	9124
O1	Sept 18, 2015 - Jan 12, 2016	$\sim 8 \times 10^{-24}$	3684	3007

CHAPTER 4

PERFORMANCE AND CHARACTERIZATION OF THE ALL-SKY HOUGH SEARCH FOR CONTINUOUS WAVES APPLIED TO THE S6 MOCK DATA CHALLENGE

As we explained in subsection 3.4.4 of the previous chapter, the optimal value for ρ_{th} (the peak threshold for the power of a frequency bin in a SFT) was proven to be 1.6 for the standard Hough (all the weights set to 1), as shown in [33]. The theoretical analysis of that section was done under several assumptions: the signal has a small amplitude, large N (number of SFTs) and that we are using the Hough search without weights. Another assumption that we made was that the noise is Gaussian and stationary. For a real search, these approximations will not always be valid, and we will use the Hough search with weights. For this reason, we want to do the search using other values for ρ_{th} and see how the detection efficiency and the computational cost of the search vary.

In this chapter we will describe the work done about the characterisation of the peak threshold ρ_{th}, which was done using the S6 Mock Data Challenge data set. We will characterize the Hough search by using the **DriveHoughMulti.c** code that is freely available [50], part of the computing libraries of LIGO: LSC Algorithm Library Applications (LALApps). DriveHoughMulti.c performs the Hough transform using as an input SFTs from the interferometers data, the frequency and the frequency band to search in the SFTs, the resolution of the sky patch, the number of spin-down values to search, the value for ρ_{th}, the pixelfactor P_f, the p for the χ^2, and two files containing the ephemeris for the Earth and the Sun. The code generates files with the loudest candidates (the ones with more significance). For each candidate, besides the significance, the code also provides its frequency, spin-down and sky position (the parameters). It also computes the χ^2 value for every candidate in the top-list.

4.1 | Mock Data Challenge data set

Mock Data Challenges (MDCs) consist on creating simulated software signals (called **injections**) that are added to real data of the detectors, in order to test the performance of the different pipelines that are used to analyse the data from the detectors. These challenges help to demonstrate that these pipelines have the appropriate sensitivity to be able to function with real data challenges, and they also serve as a mean to compare the different pipelines that are "competing" for the same targets before the science runs have started. For each pipeline, we want know the sensitivity in real data, the robustness against detector artifacts, the coverage of parameter space in frequency and spin-down, and the computational cost. The results of the MDC will guide the decision of which pipeline(s) will be treated as highest-priority in access to computing and reviewing resources. We participated in the continuous waves all-sky MDC.

This MDC search is performed over data from the S6 science run, from GPS times 931035615 - 971622272 (July 7th, 2009, 21:00:00 UTC - October 20th, 2010, 15:04:17 UTC), from the LIGO Hanford 4-km (H1) and the LIGO Livingston 4-km (L1) detectors. The continuous waves Mock Data Challenge has four stages with different objectives and types of injections. The work done in this thesis uses the stage three of the challenge, which includes 1561 open injections (all the parameters for every injection are known), scattered on a frequency range that goes from 40 to 2000 Hz. The original frames were generated on the ATLAS cluster (Albert Einstein Institute) and afterwards were moved to the CIT cluster (Caltech). The SFTs that we will use were generated for these frames also on CIT, and they contain real S6 data with the software injected signals on top of them. The software injections are generated with *lalapps_sw_inj_frames* of the LALSuite software package [51]. For the S6 science run, 9124 and 10124 SFTs of $T_{coh} = 30$ min were generated for L1 and H1 respectively.

To give an idea of some of the parameters of the injections, figures 4.1-4.4 show plots of the frequency, frequency first derivative (spin-down), sky positions, h_0 and PSD values. The spin-down values come from a randomly uniform distribution between -1×10^{-9} and -1×10^{-18} Hz/s for 95% of injections and between 10^{-18} and 10^{-13} Hz/s for 5% of injections (although the general model assumes negative spin-down values for neutron stars, some might have positive values due to large proper motions for nearby sources, or accelerations due to accretion mechanisms). We can also see that the sky positions are isotropically distributed over the sky sphere. Figure 4.4 also shows the PSD of the S6 science run for the H1 and L1 detectors. We can see that H1 had a better performance than L1. The effective noise ($\sqrt{S_n}$) is calculated using an harmonic mean averaged over S6 for the frequencies of the 1561 injections. The harmonic mean is computed, based on inverse variance weighting, by averaging together ten frequency bins to either side of the central frequency bin to compute a mean noise level, which is assumed to equal the variance.

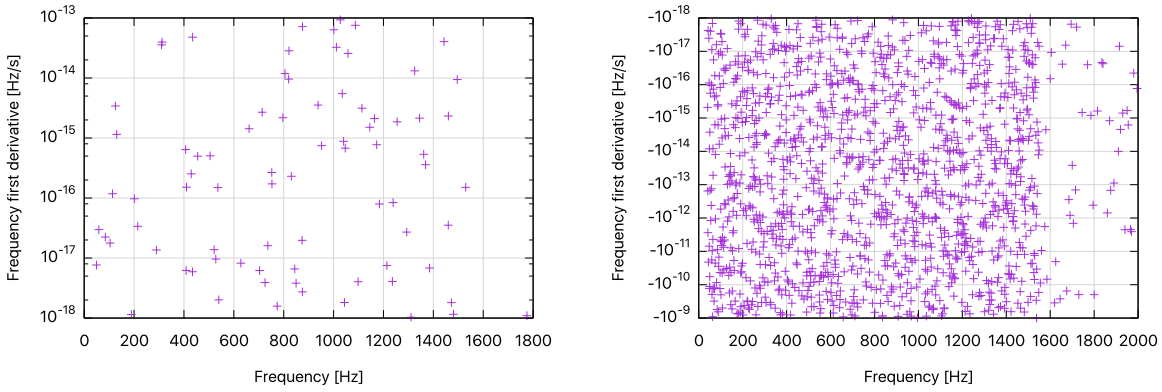

Fig. 4.1: Frequency and spindowns of the injected signals. Left image: positive values of the first frequency derivative versus the frequency values of the injections. Right image: negative values of the first frequency derivative.

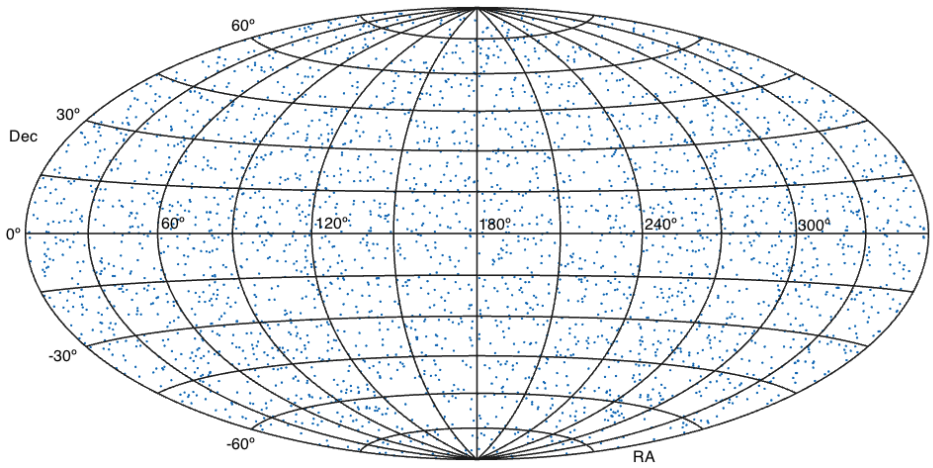

Fig. 4.2: Sky positions of the 1561 *injections.*

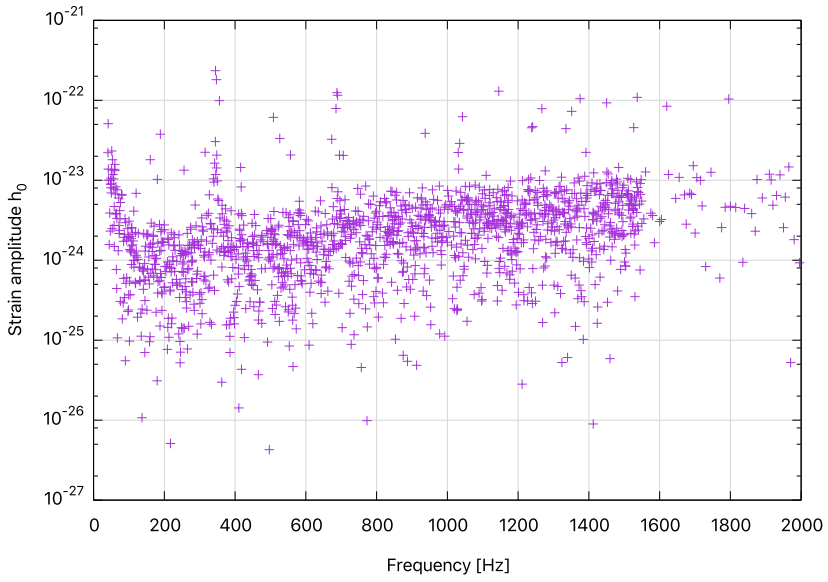

Fig. 4.3: Strain amplitude (h_0) values of the 1561 *injections versus the frequency.*

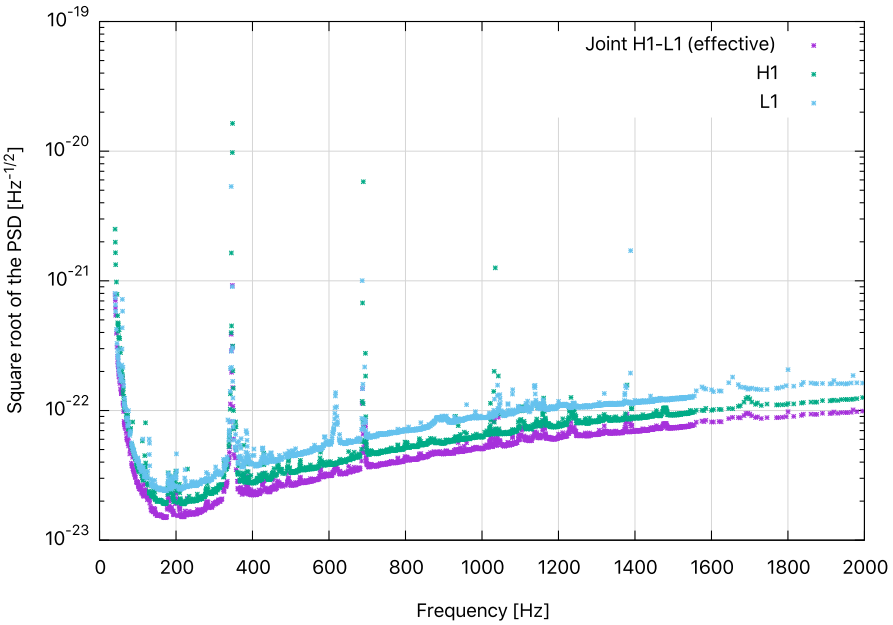

Fig. 4.4: Effective noise ($\sqrt{S_n}$) for the frequencies of the 1561 *injections. Points of H1, L1 and a combination of the two (an harmonic sum over both detectors) are shown.*

4.2 | The Hough all-sky search on the MDC data

The Hough search of the MDC data set looks for the 1561 open injections in the band 40-2000 Hz, where each search band is 0.1 Hz wide and nearly centered on the known frequency of the injection. The span of spindowns searched is given by this interval [39]:

$$[\min(-2\times10^{-9}\ \text{Hz/s}, -3\times|\dot{f}|),\ \max(2\times10^{-9}\ \text{Hz/s}, 3\times|\dot{f}|)], \tag{4.1}$$

and the search area is a square on the sky nearly centered on the injection, with a radius of:

$$R = 30^{\circ}\times\ \min(\frac{200\ \text{Hz}}{f}, 1.0). \tag{4.2}$$

Nearly centered means that the injection lies randomly in the middle 30% of a given parameter range. As we can see, the MDC search is performed over a reduced volume in parameter space around each injection. This volume is chosen to be small enough that even the most computationally expensive pipeline can participate in the MDC, and large enough so that the MDC results will accurately represent the result of a full all-sky search.

The search pipeline is schematically shown in figure 4.5, and it consists on the next steps:

1. First of all we build two data sets, called H1-L1 and L1-H1. The two sets have a mixture of SFTs from H1 and L1, but with different ordering. We follow this procedure because as can be seen in figure 4.4, the sensitivity of the H1 was better than L1 for S6. By mixing the data from the two detectors, we improve the sensitivity of the Hough search. The H1-L1 set starts with SFTs from H1 and ends with SFTs from L1. The H1 part starts

at (GPS time) 9310529494 and ends at 954929492, while the L1 part starts at 955880775 and ends at 971612930, with a total observational time $T_{obs} = 40561781$ s. The L1-H1 set starts with SFTs from L1 and ends with SFTs from H1. The L1 part starts at 931081157 and ends at 955878975, while the H1 part starts at 954938957 and ends at 971620041, with a total observational time $T_{obs} = 40540684$ s. Each data set has 9624 SFTs.

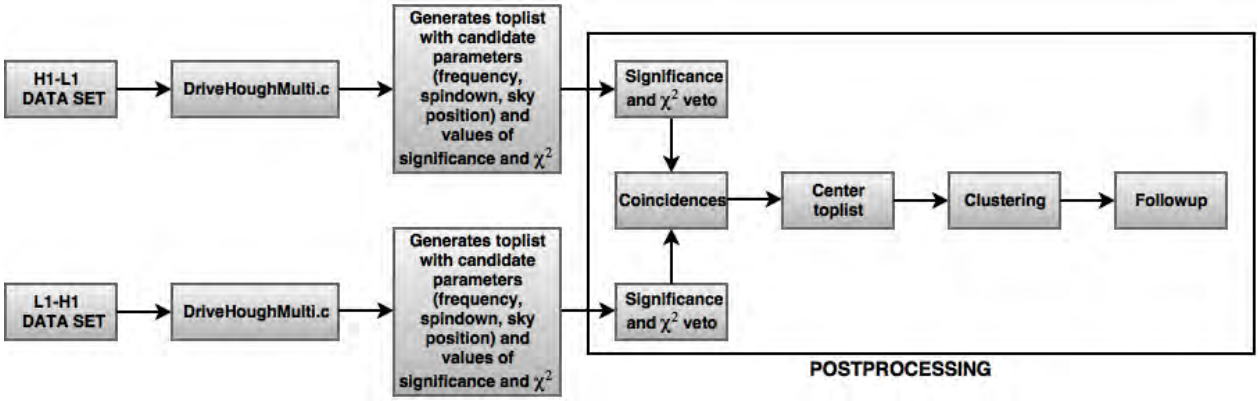

Fig. 4.5: Pipeline of the Hough all-sky search.

2. Secondly we have to run the DriveHoughMulti.c code on both data sets, using the volume in parameter space defined before. We run the code with HTCondor [40] on the Caltech LIGO cluster, using SFTs of S6 data which contain the software injected signals on top of them, producing a toplist of the 1000 most significant candidates for each detector and each injection. For this Hough MDC search, the frequency resolution is:

$$\delta f = 1/T_{coh} = \frac{1}{1800 \text{ s}} = 5.6 \times 10^{-4} \text{ Hz}, \tag{4.3}$$

while the spin-down resolution is given by:

$$\delta \dot{f} = \frac{1}{T_{coh} T_{obs}}, \tag{4.4}$$

which for the H1-L1 set is $\delta \dot{f} = 1.369652766370282 \times 10^{-11}$ Hz/s, and for the L1-H1 set is $\delta \dot{f} = 1.370365521103580 \times 10^{-11}$ Hz/s. Figure 4.6 shows a histogram of the number of spin-down values searched. The resolution of the sky grid is given by:

$$\delta\theta = \frac{1}{\frac{v}{c} f T_{coh} P_f} \approx \frac{1}{9.94 \times 10^{-5} \cdot 1800 \cdot P_f \cdot f} = \frac{1}{0.36 \cdot f}, \tag{4.5}$$

where v is the velocity[1] of the detector, which is given by $v = 2\pi AU/SID$, being $AU = 149597870700$ an astronomical unit in meters and $SID = 31558149.763545600$ a sidereal year in seconds, and P_f is the pixelfactor, which in our case is set to 2. For example, for the injection number one, the sky position (all in radians) is $\alpha = 1.886354$, $\delta = -1.356948$ (where α is the right ascension and δ is the declination), and the center of the square are

[1] This is a rough approximation to the velocity, but we only use it to calculate the sky grid resolution; for the velocity in the Doppler effect equation (2.15) (used in the number count calculation) we use an exact method that involves ephemeris.

in the sky is at $\alpha_s = 1.965067$, $\delta_s = -1.342854$. The radius of the square search area are is equal to 1.047198, and the sky resolution is equal to 0.019874. Taking into account equations (4.2) (the size of the sky patch to analyze) and (4.5) (the resolution of this sky patch), it can be seen that for $f > 200$ Hz the number of templates to analyze for each injection will be constant. After running the Hough code, we will have $1561 \times 2 = 3122$ toplists. Every toplist contains 1000 candidates (the templates with the highest value of significance).

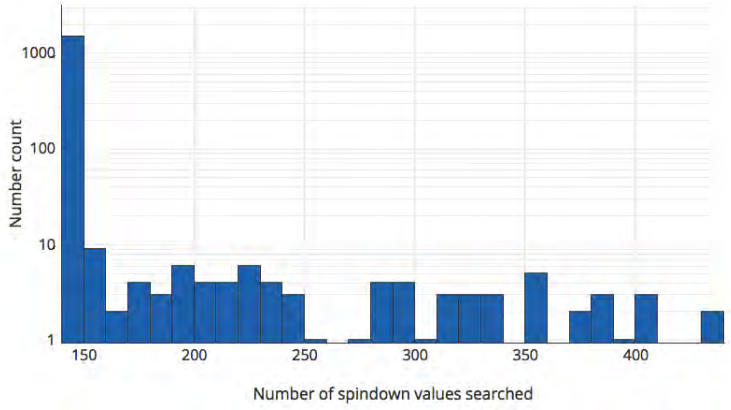

Fig. 4.6: Number count of the spin-down values searched, given by equations (4.1) and (4.4).

3. Now we have to design a procedure (called postprocessing in figure 4.5) that gives us the ability to decide if a signal is present in our results, and that returns us an estimation of the parameters (frequency, spin-down and sky position) of this signal with little error. The first step of the postprocessing is to apply the significance veto. We have to choose a minimum value for the significance, called the significance threshold s_{th}. All the candidates that have a lower value of significance than s_{th} will be vetoed. On previous analysis ([45]) this value was a function of frequency, but now we choose it to be constant. We will try different values (3, 4 and 5) for this parameter to see how the detection efficiency changes, because we don't have an exact value to choose: it is a "free" parameter of the postprocessing stage.

4. Apply the χ^2 veto. The Hough code computes a χ^2 value for every candidate in the toplist, calculated as explained in subsection 3.5. We have to compare this value to a theoretical curve obtained in a previous analysis done for the S5 search [45] (we can use it for S6 because the configuration of the detectors was very similar). This curve has some parameters that characterise the significance-χ^2 plane, dividing it in two portions. If the χ^2 value of the candidate is in the upper region, it will be vetoed, and if it's in the lower region, it will pass the veto. A more detailed explanation about this veto and its characterisation will be given in chapter 5. The S6 χ^2 veto curve is composed of two parts: one to fit mean of the χ^2 versus the significance (given by $p - 1 + A1\ s^{A2}$), and another to fit the standard deviation of the χ^2 versus the significance (given by $\sqrt{2p-2} + B1\ s^{B2}$). The second component (the std one) is multiplied by a factor called γ, which we will also

vary to see how affects the detection efficiency (this factor controls the importance of the std component). The curve is given by the following equation (we use $p = 16$):

$$\chi^2 = 15 + 0.3123\ s^{1.777} + \gamma(\sqrt{30} + 0.1713\ s^{1.621}), \tag{4.6}$$

where s is the significance. γ should at least be set to 5 in order to have a small false dismissal rate due to this veto.

5. Now we want to evaluate the coincidences between the two data sets. Before doing that, we have to translate the frequencies of one data set to the other data set. The two data sets (now called X and Y) have different reference times, so if we want to compare the parameters of both sets, we have to transform one of the two to the reference time of the other one. Because we assume the signal to have only one spin-down value, the transformation is given by the following equation:

$$f_{X\to Y} = f_X + \dot{f}_X(t_{ref_Y} - t_{ref_X}), \tag{4.7}$$

where f_X is the frequency in the set X, $\dot{f}_X$ is the first frequency derivative in the set X, and t_{ref_Y}/t_{ref_X} are the reference times in GPS of each set. We assume that the sky position and the first frequency derivative are independent of time and because of this no transformation of these parameters is needed. After translating the frequencies, we can calculate the distances between the parameters of X and Y. We define the distances for frequency (f), sky position (α for right ascension and δ for declination) and spin-down ($\dot{f}$):

$$d^f_{ij} = \frac{|f_i - f_j|}{(\delta f_X + \delta f_Y)/2} = \frac{|f_i - f_j|}{\delta f}, \tag{4.8}$$

$$d^{\dot{f}}_{ij} = \frac{|\dot{f}_i - \dot{f}_j|}{(\delta \dot{f}_X + \delta \dot{f}_Y)/2}, \tag{4.9}$$

$$d^\theta_{ij} = \frac{\arccos(\vec{n}_i \cdot \vec{n}_j)}{(\delta\theta_X + \delta\theta_Y)/2}, \tag{4.10}$$

where δf, $\delta \dot{f}$ and $\delta\theta$ are the frequency, spin-down and sky resolution respectively (with subscripts X and Y indicating the data set). These distances are calculated in bin sizes (because of the different sizes of the grid dividing all the terms in equations (4.8)-(4.9)). The distance of equation (4.10) comes from the scalar product between the two normal sky vectors, given by $\vec{n}_i = (\cos\delta_i \cos\alpha_i, \cos\delta_i \sin\alpha_i, \sin\delta_i)$. The subscript ij means the distance between the candidate i from one data set to the candidate j from the other data set. We can define two candidates to be coincident if all the distances are less than a number we choose, called coincidence window (W):

$$\begin{aligned} d^f_{ij} &< W/2 \\ d^{\dot{f}}_{ij} &< W/2 \\ d^\theta_{ij} &< W/2. \end{aligned} \tag{4.11}$$

The size of the coincidence window will control how many coincidences we get: if the coincidence window is bigger, we will have more coincidences. The value of the coincidence window is equal to half of the distance that we allow: for example, if the coincidence window is set to 6 bins, only a distance of 3 bins to every side of the candidate parameter will be valid. If we set our coincidence window to be equal to 5 bins, it will correspond to $5^4 = 625$ coincident cells in parameter space (five for every one of the four dimensions of parameters).

6. Now, we want to create a new list containing only the candidates that had coincidences. To create this new unique list, we have to generate a new center in frequency, spin-down, right ascension, declination and significance for each surviving coincident pair, defined by:

$$f_{ij}^c = \frac{f_i + f_j}{2}, \tag{4.12}$$

$$\dot{f}_{ij}^c = \frac{\dot{f}_i + \dot{f}_j}{2}. \tag{4.13}$$

$$n_i^1 = \cos\delta_i \cos\alpha_i \quad n_i^2 = \cos\delta_i \sin\alpha_i \quad n_i^3 = \sin\delta_i, \tag{4.14}$$

$$n_{ij}^k = \frac{n_i^k + n_j^k}{2} \quad \text{for } k = 1, 2, 3, \tag{4.15}$$

$$\hat{n}_{ij}^k = \frac{n_{ij}^k}{\sqrt{(n_{ij}^1)^2 + (n_{ij}^2)^2 + (n_{ij}^3)^2}} \quad \text{for } k = 1, 2, 3, \tag{4.16}$$

$$\alpha_{ij}^c = \arctan \hat{n}_{ij}^2 / \hat{n}_{ij}^1, \tag{4.17}$$

$$\delta_{ij}^c = \arcsin \hat{n}_{ij}^3, \tag{4.18}$$

$$s_{ij}^c = \frac{s_i + s_j}{2}. \tag{4.19}$$

7. When we have created the centers, we want to study the formation of clusters based on the geodesic distance between the centers in the space of parameters. A chain is defined as a group of centers that are joined to at least another center in the same chain if the distance between them is lower or equal than $R_{cluster}$ (a distance in bins, which in our case is set to 3). A center can only be a member of one chain in each of the four dimensions. We will select the two most populated (number of members) chains for each dimension, having a maximum of eight chains. A cluster is defined by the intersection of one chain of each dimension. For example, we can create a cluster with the first chain of frequency, the second chain of spin-down, the second chain of declination and the first chain of right ascension. This way, we can create different combinations of clusters. At the end, we will keep the most populated cluster. If after all these steps we have one remaining cluster, we

can calculate its follow-up center as:

$$\begin{aligned} f_{ij}^F &= \frac{\sum_{ij=1}^{N_c} f_{ij}^c s_{ij}^c}{\sum_{ij=1}^{N_c} s_{ij}^c}, \\ \dot{f}_{ij}^F &= \frac{\sum_{ij=1}^{N_c} \dot{f}_{ij}^c s_{ij}^c}{\sum_{ij=1}^{N_c} s_{ij}^c}, \\ \alpha_{ij}^F &= \frac{\sum_{ij=1}^{N_c} \alpha_{ij}^c s_{ij}^c}{\sum_{ij=1}^{N_c} s_{ij}^c}, \\ \delta_{ij}^F &= \frac{\sum_{ij=1}^{N_c} \delta_{ij}^c s_{ij}^c}{\sum_{ij=1}^{N_c} s_{ij}^c}, \end{aligned} \tag{4.20}$$

where N_c is the number of centers of the cluster. The α and δ equations are only valid because the sky region studied is very small. These equations use the values of the significances (s_{ij}^c) to weight each center, so the more significant a center is the more weight will have for the follow-up point. These will be the parameters that we recover from the signal/injection. We claim a detection if the postprocessing procedure recovers a follow-up center for the injection.

4.3 | Study of the efficiency and parameter estimation for different ρ_{th} values

As explained in the beginning of this chapter, we want to quantify how a change in ρ_{th} affects the detection efficiency. The efficiency is measured in terms of the % of injections that are detected by the search. We also want to calculate the error in parameter estimation: the distance between the injection parameters (frequency, first frequency derivative and sky position) and the parameters of the recovered candidates. For a real search, this distance tells us which region in parameter space around a candidate would need to be followed up, and in the MDC, it serves as a useful check that candidates being claimed as detections are within a reasonable distance of the injections parameters. Besides the detection efficiency and the parameter estimation, we also want to compare the computational cost of the search for every different value of ρ_{th}.

The MDC data sets will be analyzed following the procedure of the previous section using different ρ_{th} values, to see which one gives the best results. We will compare the results using values for ρ_{th} of 1.6, 1.7, 2.0, 2.2 and 2.5. $\rho_{th} = 1.6$ was the optimal value of the Hough search without weights, as explained in subsection 3.4.4; and $\rho_{th} = 2.5$ is the value that the frequency Hough search (another all-sky continuous wave search method [52] based on the Hough transform) uses. As can be seen in figure 3.4, the region between $\rho_{th} = 1.6$ and $\rho_{th} = 2.5$ is very flat, so we expect that a change of ρ_{th} in this region may improve our pipeline. For every ρ_{th} value we have repeated the postprocessing procedure using different values of the coincidence window (2, 3 and 4) and the significance threshold (3, 4 and 5). The values that we will use for these two parameters are based in previous analysis [45]. This is done in order to find the

most convenient tunning of these parameters. We could choose lower values for the significance threshold or higher values for the coincidence window to improve the efficiency, but doing this increments the error in the parameter estimation and also increases the false alarm probability. We also did the analysis changing the value of γ (of the χ^2 veto), but the results didn't change a lot, so we choose to show the plots using a constant value of $\gamma = 5$.

To compare the performance of each ρ_{th} we use the detection efficiency, which is the fraction of injections that are considered detected. The detection efficiency is measured as a function of the sensitivity depth, which is given by the division of the square root of the single sided power spectral density $\sqrt{S_n}$ and the amplitude h_0 of the signal. S_n is the harmonic sum over both detectors of the approximate harmonic mean power spectral density of the data, at the frequency of the each injection (the H1-L1 joint values of figure 4.4). The harmonic mean is computed, based on inverse variance weighting, by averaging together ten frequency bins to either side of the central frequency bin to compute a mean noise level, which is assumed to equal the variance.

Figures 4.7-4.16 show the detection efficiency versus the sensitivity depth for different values of ρ_{th} with different combinations of the significance threshold and the coincidence window. This plots show how the detection efficiency changes in function of how much bigger is the amplitude of the signal than the noise of the detector. At fixed detection efficiency, a more sensitive search will detect a weaker signal (it will have a higher sensitivity depth). In all the efficiency plots we show seven points. Each of these points represents a mean calculated between 223 injections of the 1561. The mean in sensitivity depth ($\sqrt{S_n}/h_0$) is calculated for every injection, and then we sort them with ascending order. Then, a mean of this quantity for every 223 points is calculated. Next to each efficiency plot, we also show a parameter estimation error histogram. This histogram shows the difference in bins between the follow-up centre (equation (4.20)) that has been calculated in the postprocessing stage and the original parameters of the injection. With this histogram we can see if any of the detections that we have made has a lot of error, thus being a false alarm detection. The "W" legend of the following plots gives the coincidence window used for frequency, sky position and spin-down (the window is equal for each parameter), and the "S_T" legend stands for significance threshold.

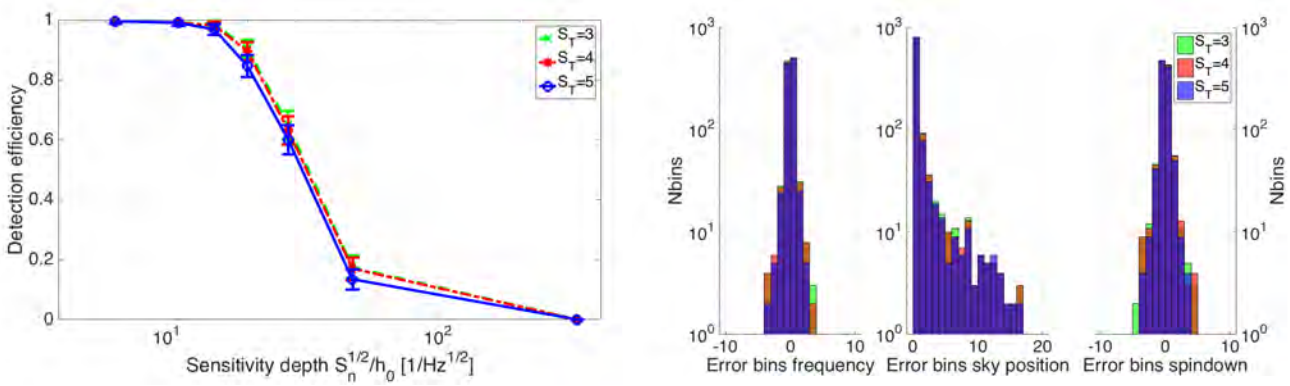

Fig. 4.7: Efficiency and error of the parameter estimation for $\rho_{th} = 1.6$, changing the significance threshold. A coincidence window of 3 is used.

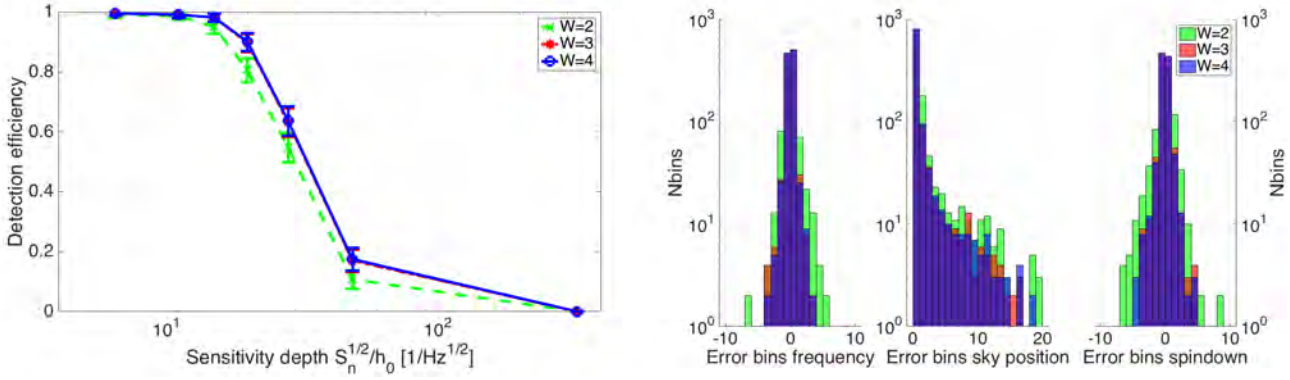

Fig. 4.8: Efficiency and error of the parameter estimation for $\rho_{th} = 1.6$, changing the coincidence window size. A significance threshold of 4 is used.

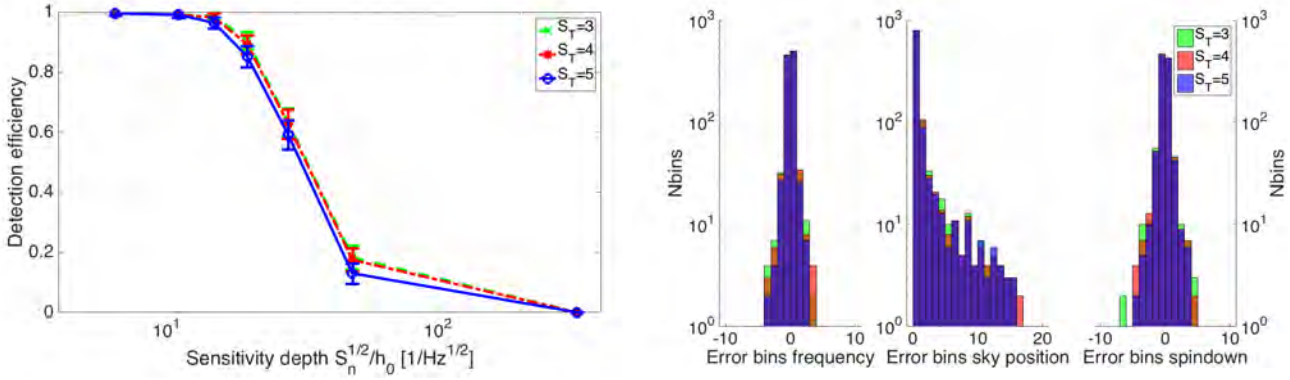

Fig. 4.9: Efficiency and error of the parameter estimation for $\rho_{th} = 1.7$, changing the significance threshold. A coincidence window of 3 is used.

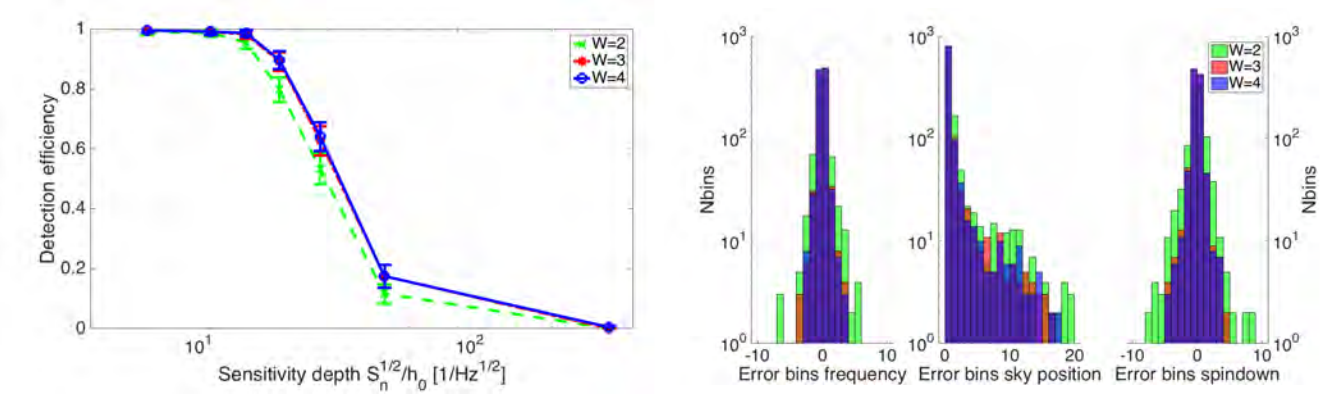

Fig. 4.10: Efficiency and error of the parameter estimation for $\rho_{th} = 1.7$, changing the coincidence window size. A significance threshold of 4 is used.

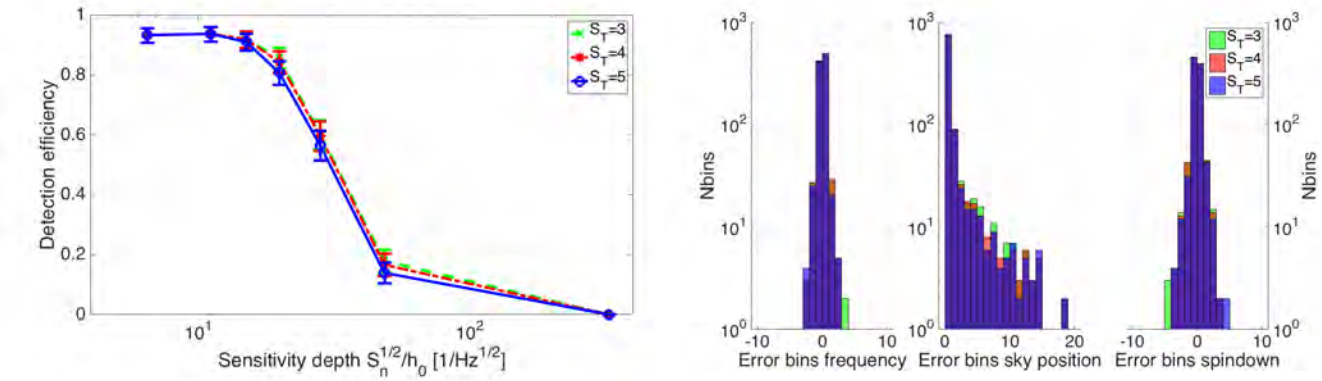

Fig. 4.11: Efficiency and error of the parameter estimation for $\rho_{th} = 2.0$, changing the significance threshold. A coincidence window of 3 is used.

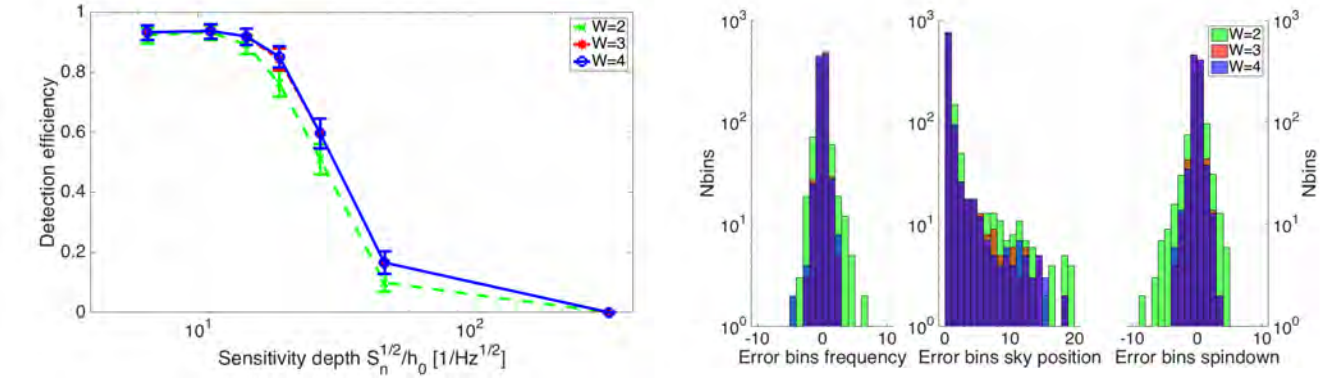

Fig. 4.12: Efficiency and error of the parameter estimation for $\rho_{th} = 2.0$, changing the coincidence window size. A significance threshold of 4 is used.

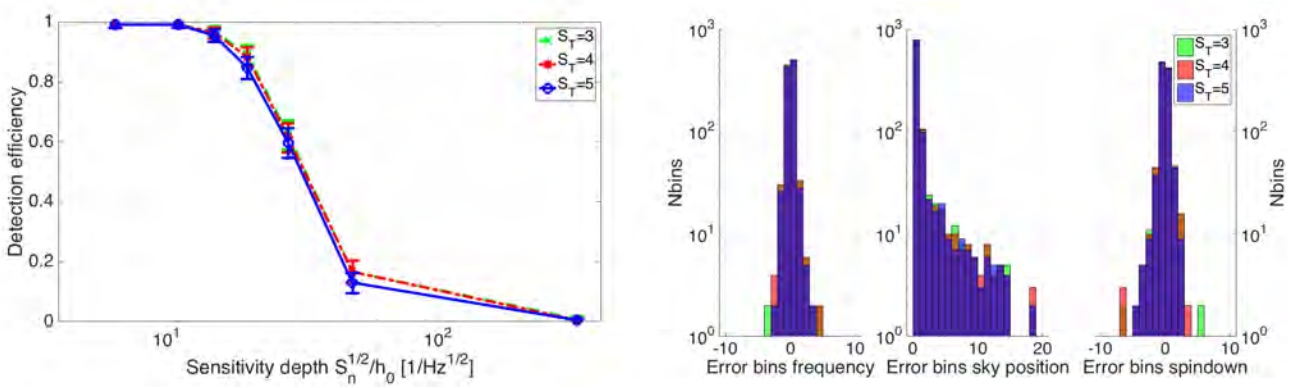

Fig. 4.13: Efficiency and error of the parameter estimation for $\rho_{th} = 2.2$, changing the significance threshold. A coincidence window of 3 is used.

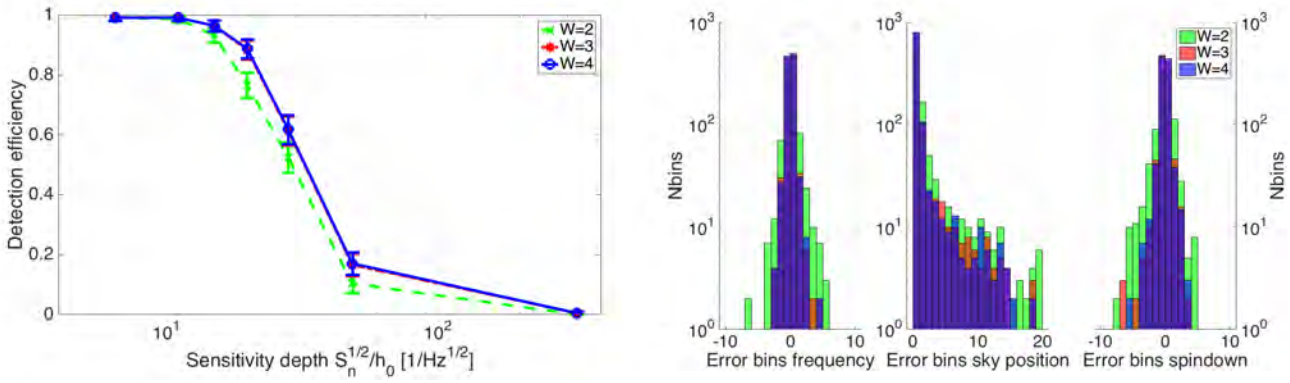

Fig. 4.14: Efficiency and error of the parameter estimation for $\rho_{th} = 2.2$, changing the coincidence window size. A significance threshold of 4 is used.

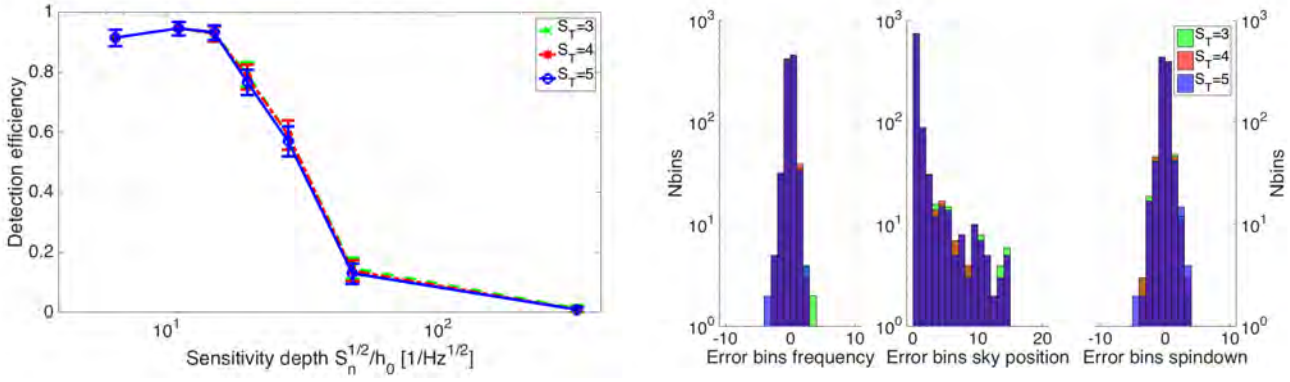

Fig. 4.15: Efficiency and error of the parameter estimation for $\rho_{th} = 2.5$, changing the significance threshold. A coincidence window of 3 is used.

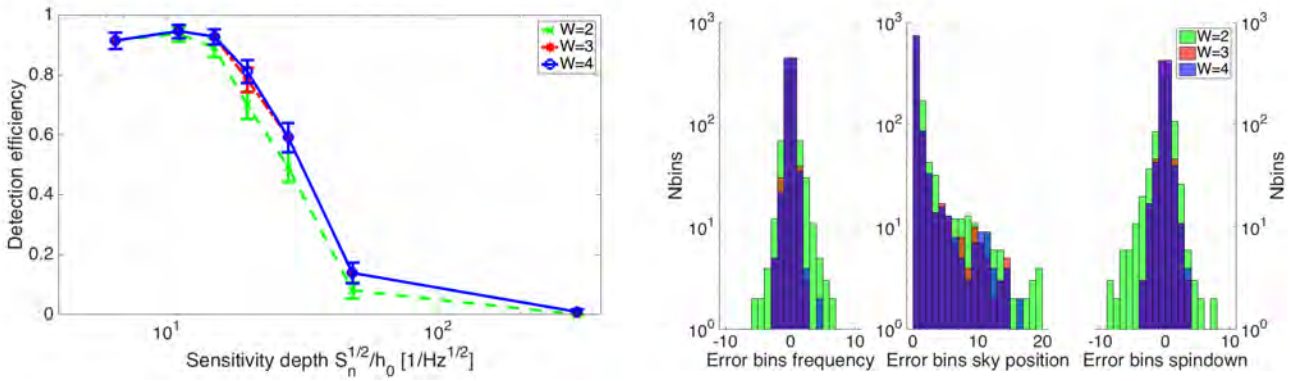

Fig. 4.16: Efficiency and error of the parameter estimation for $\rho_{th} = 2.5$, changing the coincidence window size. A significance threshold of 4 is used.

We can see the different effects that the free parameters produce. Having a bigger window of coincidence allows more coincidental candidates, for this reason the detection efficiency is higher. In a real search case, having a bigger window would raise the false alarm probability. It can also be seen that raising the significance threshold decreases the detection efficiency: less injections pass the veto. As with the coincidence window, lowering the significance veto raises the false alarm rate.

Looking at figures 4.7-4.16, and balancing the efficiency and the parameter estimation, we conclude that the best parameters to use are a coincidence window of 3 and a significance threshold of 4. To see more clearly which value of ρ_{th} is the best one, we can plot the efficiency of each ρ_{th} value using these two values of coincidence window and significance threshold. Figure 4.17 shows this plot. Table 4.1 compares the results at three different points.

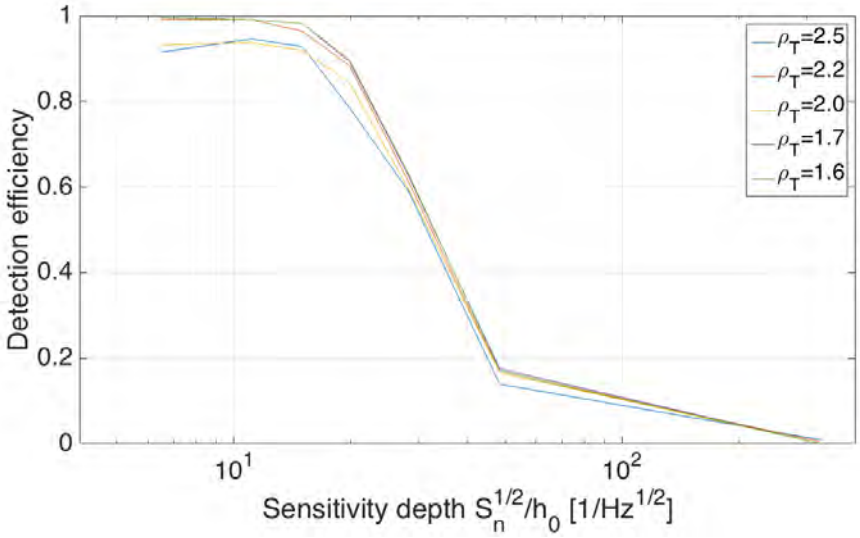

Fig. 4.17: Efficiency for the different values of ρ_{th} using a significance threshold of 4 and a coincidence window of 3.

Detection efficiency [%]		Peak threshold				
		1.6	**1.7**	**2.0**	**2.2**	**2.5**
Sensitivity	**11.0895**	0.9910	0.9910	0.9372	0.9910	0.9462
depth	**19.8621**	0.8969	0.8924	0.8430	0.8834	0.7848
$[1/\sqrt{Hz}]$	**48.3979**	0.1704	0.1749	0.1659	0.1659	0.1390

Table 4.1: Efficiency for the different values of ρ_{th} at three different points of sensitivity depth.

Clearly, the values 2.5 and 2.0 have the worst results. It seems that the best value of ρ_{th} is 1.6, but there isn't a lot of difference with the 1.7 and 2.2 results. This is compatible with figure 3.4. In the next section we will compare the computational cost of every ρ_{th}.

4.4 | Computational cost

We want to compare the computational cost for each value of ρ_{th} (by computational cost we mean the time that the Hough code takes to run). The Hough code outputs a file that contains some timestamps, indicating the progress of the code. We will extract these timestamps, and calculate the subtraction between the final and initial time, obtaining the time in seconds. This way, we will have a time value for every injection analysed.

To run the Hough code, we use the Caltech cluster and the HTCondor software. The cluster has a lot of different machines, with different processor and memory capabilities. We use **Dual Intel(R) Xeon(R) CPU E5-2670 0 @ 2.60GHz (Sandy Bridge)** processors. Figures 4.18-4.21 show the computational cost of all the injections for each ρ_{th}.

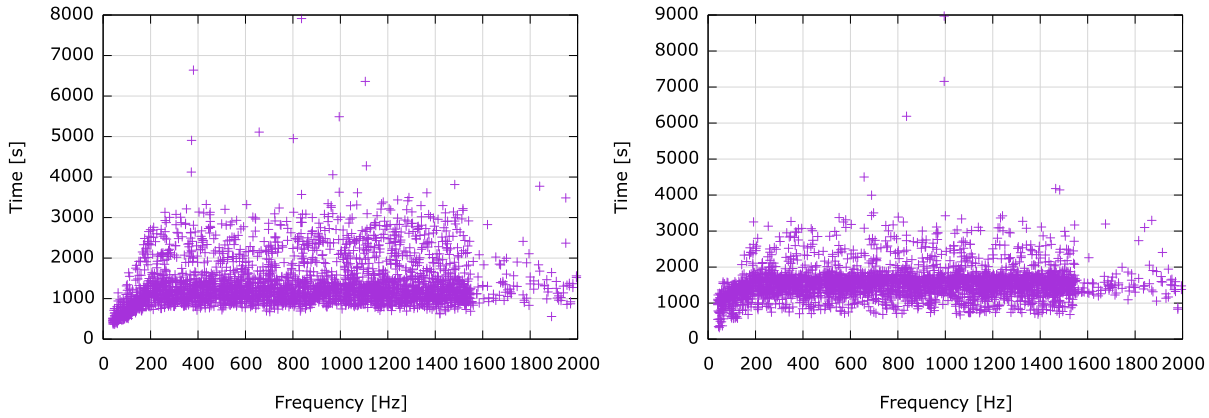

Fig. 4.18: Computational cost in seconds for every injection versus the frequency, using $\rho_{th} = 1.6$ (left) and $\rho_{th} = 1.7$ (right).

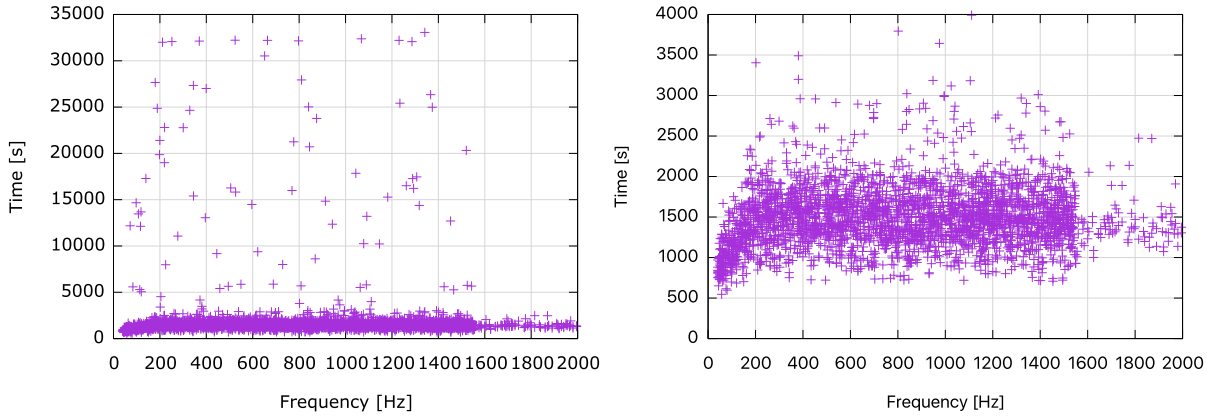

Fig. 4.19: Computational cost in seconds for every injection versus the frequency, using $\rho_{th} = 2.0$. The right plot is a zoom of the left one.

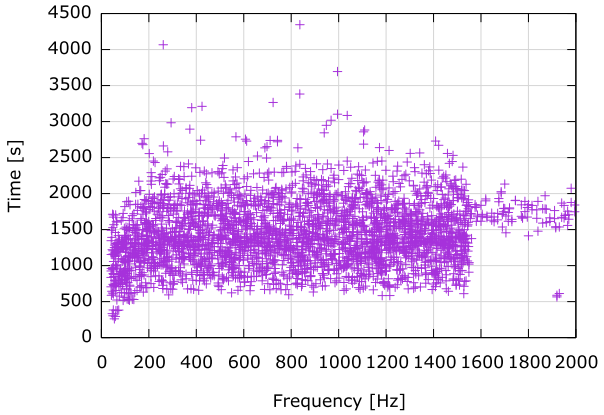

Fig. 4.20: Computational cost in seconds for every injection versus the frequency, using $\rho_{th} = 2.2$.

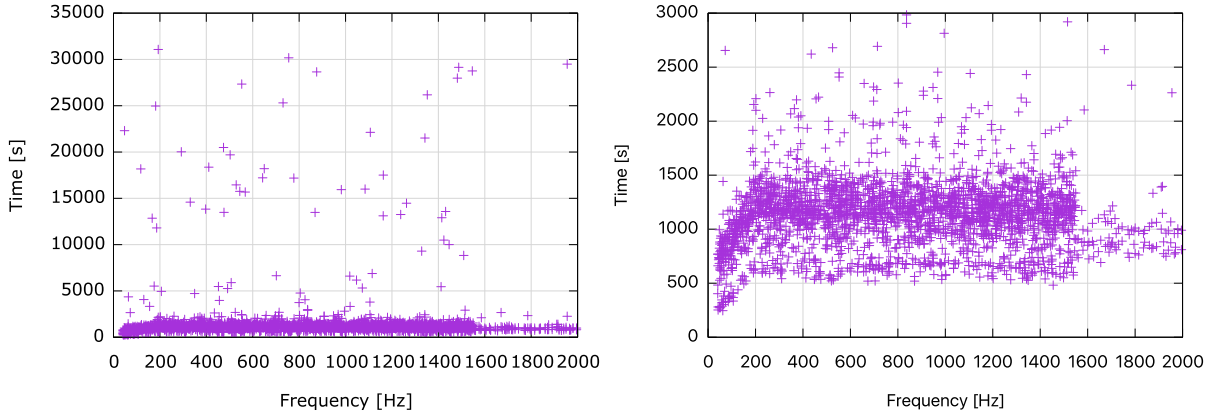

Fig. 4.21: Computational cost in seconds for every injection versus the frequency, using $\rho_{th} = 2.5$. The right plot is a zoom of the left one.

Two main features can be seen in figures 4.18-4.21. Firstly, it can be seen that the computational time for the injections with $f < 200$ Hz has a positive slope, and for $f > 200$ Hz the time stays constant. We explained earlier why this happens: the size of the sky patch becomes

smaller, and the resolution of the sky patch becomes bigger (this is governed by equations equations (4.2) and (4.5)). Secondly, for $\rho_{th} = 2.0$ and $\rho_{th} = 2.5$ we can see that some injections have very large computational times. This is due to the usage of the Caltech clusters and the HTCondor software. The computational times may vary a lot between two injections with similar frequencies and the same peak threshold, and even it may vary for the same injection calculated at two different times. As we explained before, the usage of the machines varies with time, and different machines have different memory capabilities. This explains the dispersion of some of the times. Moreover, as we saw in figure 4.6, not all the injections search the same number of spindowns. For this reason, we have to divide the times by the number of spin-down values searched, in order to normalize the times.

Having in mind the two previous features, it would be better to compare the different ρ_{th} using only the computational times of the injections with $f > 200$ Hz, and setting a maximum computational time, to avoid the disturbances caused by the cluster machines. Also, we are going to divide the time of every injection by the number of spin-down values searched. Figures 4.22-4.24 show histograms of the computational times using only the injections with $f > 200$ Hz and with a maximum 5000 seconds of computational time. Table 4.2 shows the mean and the median for each value of ρ_{th}.

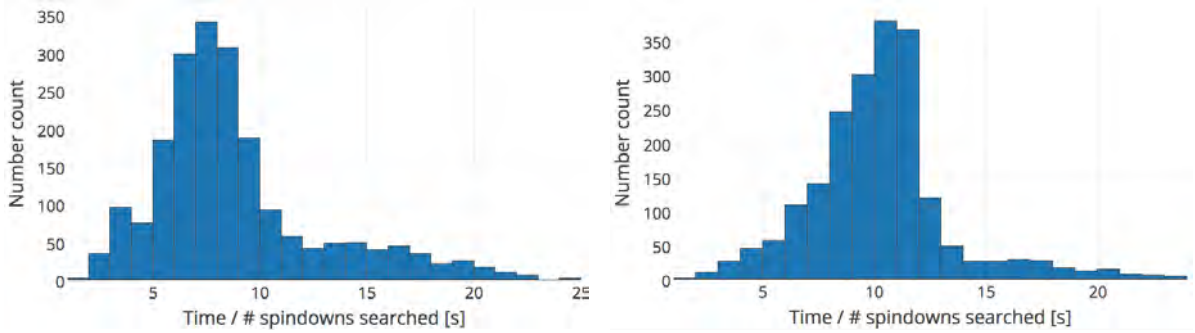

Fig. 4.22: Histograms of the computational times divided by the number of spin-down values searched for $\rho_{th} = 1.6$ (left) and $\rho_{th} = 1.7$ (right) for injections with $f > 200$ Hz.

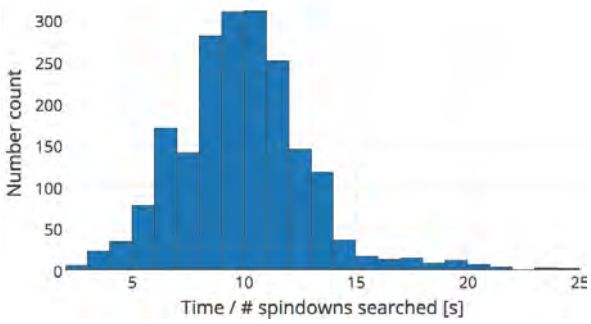

Fig. 4.23: Histogram of the computational times divided by the number of spin-down values searched for $\rho_{th} = 2.0$ for injections with $f > 200$ Hz.

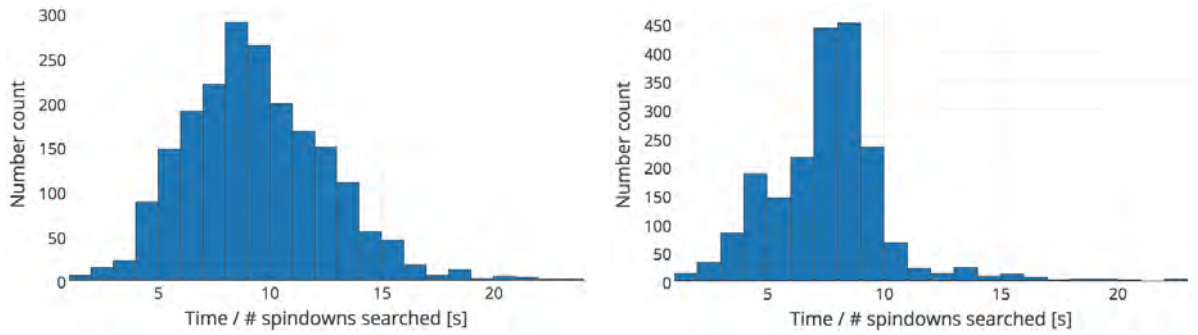

Fig. 4.24: Histograms of the computational times divided by the number of spin-down values searched for $\rho_{th} = 2.2$ *(left) and* $\rho_{th} = 2.5$ *(right) for injections with* $f > 200$ *Hz.*

	$\rho_{th} = 1.6$	$\rho_{th} = 1.7$	$\rho_{th} = 2.0$	$\rho_{th} = 2.2$	$\rho_{th} = 2.5$
Mean [s]	9.07029	10.2799	9.91043	9.49493	7.57907
Median [s]	8.09265	10.2145	9.80670	9.26155	7.67900

Table 4.2: Mean and median computational times divided by the number of spin-down values searched for the different ρ_{th} *values for the MDC S6 search, using only the injections with* $f > 200$ *Hz and a maximum computational time of* 5000 *seconds.*

As explained before, the peak threshold gives the probability that we select a bin: $p = e^{-\rho_{th}}$. If ρ_{th} is higher, the probability will be smaller, and less bins will be selected. For this reason, the computational cost should be smaller when the peak threshold is higher. Looking at table 4.2, we can see that this is followed by the mean and median values: from $\rho_{th} = 1.7$ to $\rho_{th} = 2.5$, we can see that the values are decreasing. $\rho_{th} = 1.6$ is a special case, as signaled by the double vertical bar: for this case, the Hough code was run a bit later, and the discrepancy in the pattern may be explained by the implementation of new machines in the cluster with better capabilities, and also because the computational load of the CIT cluster was reduced (the parameter estimation searches of GW150914 and GW151226 had concluded). In order to improve the results and to exactly quantify the computational cost of each ρ_{th} value, the searches should be repeated on dedicated nodes to properly benchmark the code, always using the same processor and without interference from other users.

CHAPTER 5

CALIBRATION OF THE χ^2 TEST USING LIGO O1 DATA

This chapter summarises the work done related to the χ^2 veto characterisation for the O1 science run.

The O1 science run took place between September 18, 2015 - January 12, 2016. Two detectors were active: one in Hanford, Washington, of 4 km, named H1; and another one in Livingston, Lousiana, of 4 km, named L1. Figure 5.1 shows the sensitivity of the detectors for the O1 science run. It can be seen that L1 was slightly more sensitive than H1. For this science run, 3684 SFT's for H1 and 3007 SFT's for L1 of $T_{coh} = 30$ min were produced. These SFTs are located in the Caltech cluster (CIT), available for the LSC members. As was done for the S6 MDC, all the search codes are managed using the HTCondor software available at the ATLAS and CIT clusters.

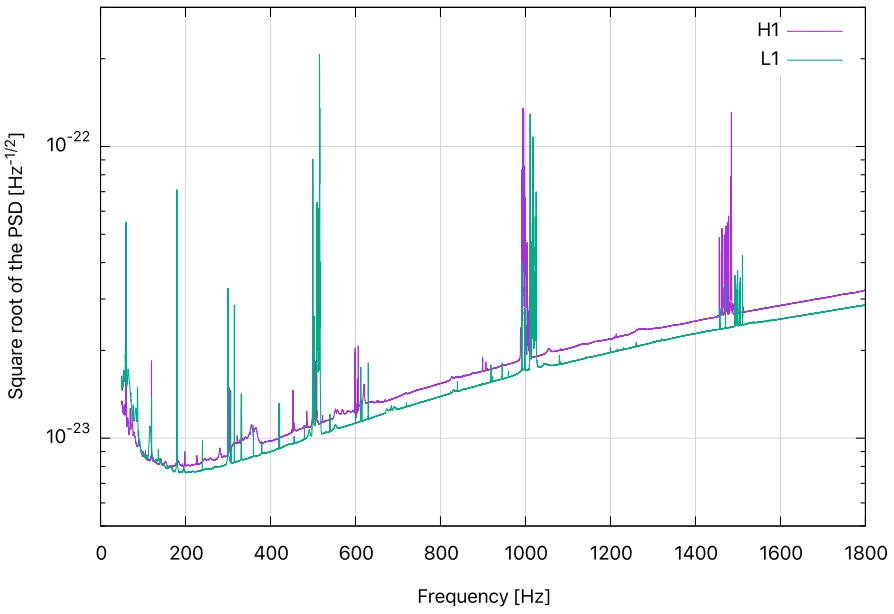

Fig. 5.1: Square root of the PSD ($\sqrt{S_n}$) for H1 and L1 during the O1 science run.

5.1 | Characterization of the significance-χ^2 plain

As explained in section 3.5, the χ^2 veto is used to remove candidates in the toplists originated by disturbances and artefacts of the detector. When we perform the search using the Hough code [50], it returns the significance and χ^2 (calculated using equation (3.59)) values for every candidate in the toplist. In the ideal case of having only Gaussian noise and a real signal with no mismatch in parameter space, the distribution of the χ^2 values of the candidates should follow a χ^2 distribution with p degrees of freedom. This is not the real case, since the noise is not Gaussian neither stationary, and the parameters of the signal usually don't agree perfectly with the parameters of the candidates from the search. For these reasons, we know that the χ^2 values depend on the significance s, and just in the case of having only noise the mean of the χ^2 is $p-1$ and the std is $\sqrt{2p-2}$.

Before we can apply the χ^2 veto, it has to be calibrated for the corresponding data set. We have to characterize and separate the values χ^2-significance that are compatible with a possible astrophysical signal from those who are not (establishing a relation between the significance and the χ^2 values). This way, we will separate the χ^2-s plane in two different regions: the upper-curve region and the lower-curve region. Then, we will be able to tell if a candidate passes the veto: if its χ^2value is in the upper-curve region, it will be eliminated. The χ^2-s plane separation will be given by an equation relating these two values, which we have to characterise by injecting fake signals in the data and analysing their behaviour (this characterization has to be performed for every different data set, meaning that the characterization that was done for S6 will not be the same as the one for O1).

To characterise the equation, we follow the next steps. First of all, we have to choose a value for p (the number of blocks in which we divide our data). We want p to be a big number, because there could be disturbances in the data only present during a short time that we want to be able to discriminate (if p is small, we don't have enough blocks to distinguish these short disturbances using equation (3.59)). We also want each of block of data to contain a big number of SFTs, so p also needs to be small. For this reasons, we don't have an exact method to choose p, so we will choose $p = 16$, a value which was used in previous analysis [45]. The value of p has to be the same that is going to be used for the search.

After selecting the value of p, we have to characterize the significance-χ^2 plane. To do this, we will use Monte Carlo software injected signals. These signals are created and injected in real data of the O1 science run using the code **MCInjectHoughMultiChi2Test.c** [49]. The code creates signals with random parameters (sky position, frequency derivative) from a given frequency band which is 0.1 Hz wide and with an h_0 value (amplitude) between h_0^{min} and h_0^{max}, two parameters that we select. These injections also have random values of $\cos\iota$, ψ and ϕ_0. The output of the code is composed of various files, one of them being the significance and χ^2 values for every combination of parameters (the results of the Hough search). These values can be

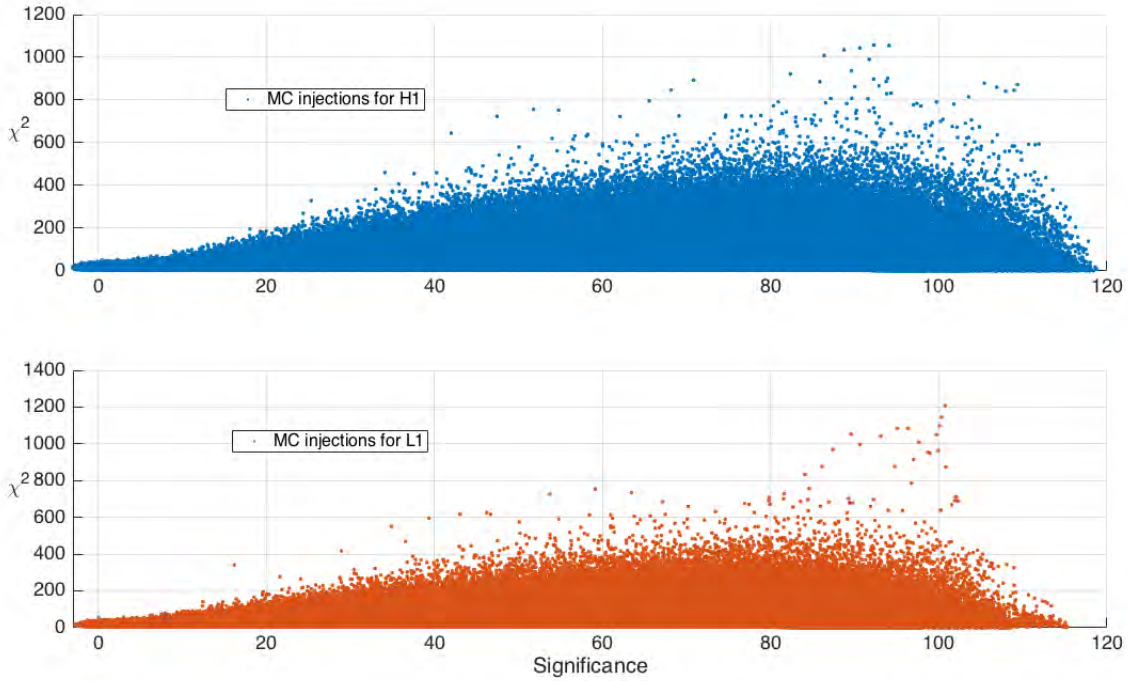

Fig. 5.2: Significance and χ^2 values of the Monte Carlo injections made with the MCInjectHoughMultiChi2Test code. The upper panel shows the results for H1; the lower panel shows the results for L1.

seen in figure 5.2. To characterize properly the significance-χ^2 plane, we have to inject signals covering all the frequencies that we will search afterwards, and with h_0 values that are related to the power spectral density of the real data, choosing h_0^{min} and h_0^{max} to approximately contain the values of the following upper limits formula [45]:

$$h_0^{95\%} = C \left(\frac{1}{\sum_{i=0}^{N-1} (S_i)^{-2}} \right)^{1/4} \sqrt{\frac{\mathcal{S}}{T_{coh}}}, \tag{5.1}$$

where C is a constant, and:

$$\mathcal{S} = \mathrm{erf}^{-1}(2\alpha_H) + \mathrm{erf}^{-1}(2\beta_H), \tag{5.2}$$

where α_H is the false alarm, β_H the false dismissal probability and S_i is the average value of the single sided power spectral noise density of the ith SFT in the corresponding frequency sub-band (more information about upper limits in [45]). We have injected 1000 signals for every different value of h_0 for every 0.1 Hz band, with 10 different values of h_0 per band (that means that we have 10000 signals for every frequency value). We choose 0.1 frequency bands that are free of known spectral disturbances, and separated enough in frequency to span the whole spectrum of interest for a real search (giving the possibility to check if the χ^2 characterization depends on frequency). We choose bands with low significance values because we want to do the injections in quiet bands, to evaluate the behaviour of the veto only due to the effect of the injected signal, without the presence of disturbances.

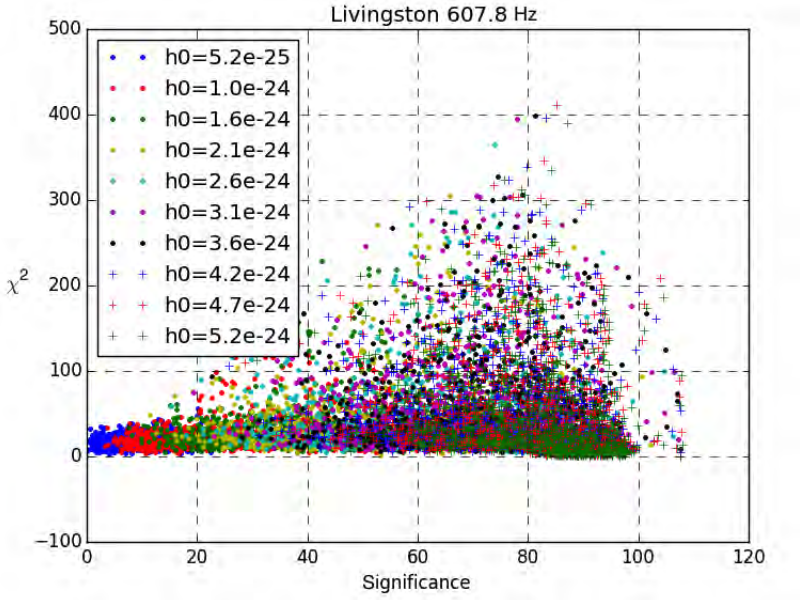

Fig. 5.3: χ^2 versus signficance for a 0.1 *frequency band. The ten different groups of h_0 can be seen. The higher h_0 values are located to the right (more significant) as was expected.*

To check that the output of the MCInjectHoughMultiChi2Test code has the expected behaviour, we can plot the χ^2 versus the significance for one 0.1 Hz band and see if the ten groups containing the ten different values of h_0 are properly plotted. To make sense, the higher the h_0 is, the higher the significance should be as well. Figure 5.3 shows this kind of plot. We can do this plot for every frequency band in the analysis.

After checking the h_0 behaviour, we want to check the χ^2 versus the significance for every big group of frequencies. We make 7 groups of frequency, listed in table 5.1. This will be useful to check if the band is a noisy one: we chose the bands by their significance, but maybe they have a bad behaviour due to instrumental artefacts and we don't want to use frequency bands contaminated with spectral artefacts for the MC injections for the χ^2 characterisation. Figures 5.4 and 5.5 show this type of plot.

We want to characterise the χ^2 curve by injecting signals in the background noise that is non-Gaussian and non-stationary, but not in those frequency bands containing the artefacts we would like to veto in a search. Those artefacts could have very small amplitudes and not be easily visible from in the spectrum, but able to produce candidates that we want to discriminate.

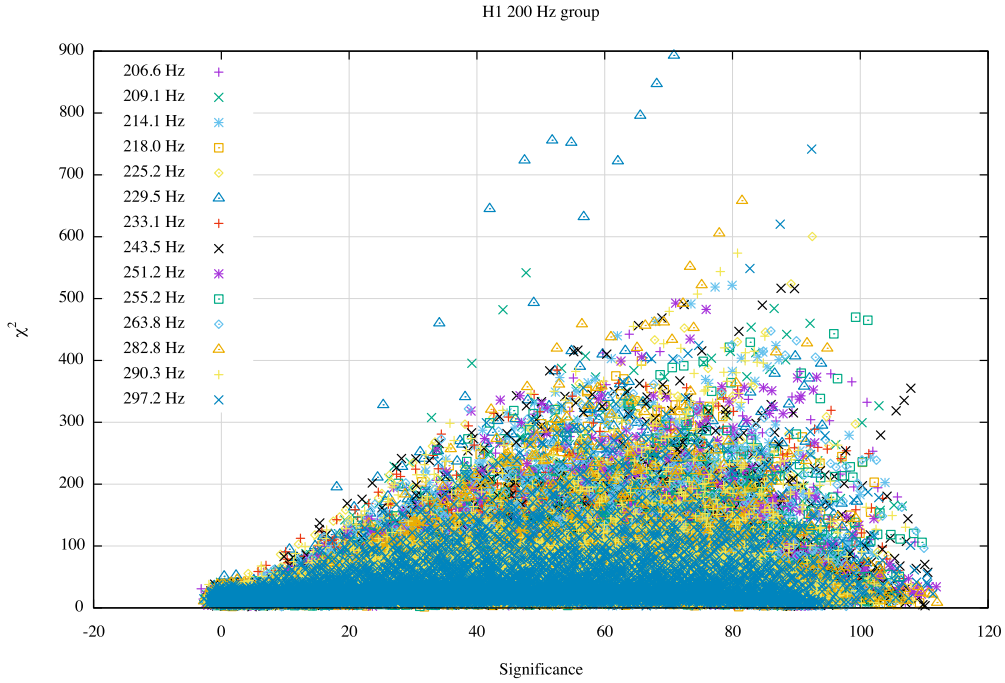

Fig. 5.4: Plot of the χ^2 versus significance for all the Hanford bands between 200-300 *Hz that we have selected to do the analysis.*

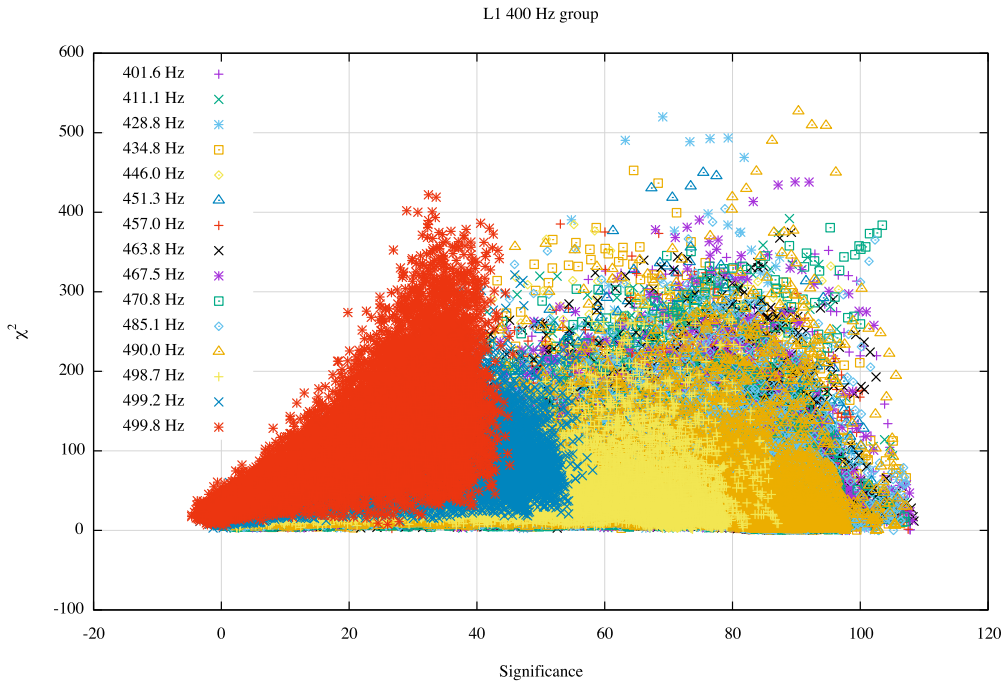

Fig. 5.5: Plot of the χ^2 versus significance for all the Livingston bands between 400-500 *Hz that we have selected to do the analysis.*

Figure 5.4 is an example of the expected behaviour: there is not any band that has an odd behaviour. Clearly, figure 5.5 is very different: we can see some bands near 500 Hz (due to

the violin modes of the detector) showing strange behaviour: they are clustered in low values of significance, not being spread like the good-behaving bands. After doing this kind of plot for all the frequency groups, we eliminated some of the bands that we used in the Monte Carlo injections, and we kept only the bands shown in table 5.1. In that table we can see that a lot more of bands have been used to do the analysis than in previous characterizations, like the one done for S5 [45]. It also can be seen that the number of bands for each detector is not symmetric: at first, the same amount of bands for each detector were selected, but after doing plots like the one in figure 5.5 some of the bands were eliminated, as explained before. All the bands remaining in table 5.1 were examined in plots of their PSD in search of outliers or strange behaviour, and none of them had any visible spikes in the spectrum.

5.2 | Characterization of the χ^2 veto curve

After doing the preliminary checks of the previous section, we want to obtain the curve that will separate the significance-χ^2 plane in two regions. We will fit the values of the χ^2 mean and the χ^2 standard deviation to a curve, like a power law or a polynomial one. To do this, first we have to sort the points obtained with the MCInjectHoughMultiChi2Test code (the ones in figure 5.2) in significance: from lower to higher. After this, we group them in sets of 1000 points (the size of the sets is a "free parameter", we will study later how it affects the results), and then we calculate the mean of the significance and the mean and standard deviation of the χ^2 of every set. Only points with the significance between 2 and 70 are used (the effect of changing the higher boundary will also be studied later), because in a real search, as explained before, a threshold on the significance is always set (usually with a value of 4), and significances greater than 70 are not expected (for real astrophysical signals). We use this grouping of points because trying to fit a curve to all the points coming out from the MCInjectHoughMultiChi2Test code would be impossible: for every 0.1 Hz band, there are 10000 points (10 h_0 values multiplied by 1000 combinations of different random parameters). To fit the groups of points, we will try different curves, which have two components: one to fit the mean of the significance versus the mean of the χ^2, and another to fit the mean of the significance versus the standard deviation of the χ^2. The first curve that we are going to try, since it was used in previous characterizations ([45]) of the χ^2 veto, is a power law:

$$\bar{\chi}^2 = p - 1 + A1\ s^{A2} + \gamma(\sqrt{2p-2} + B1\ s^{B2}), \tag{5.3}$$

where p is the number of blocks of the χ^2 veto, (A1, A2, B1, B2) are the parameters to fit (the A's from the mean, and the B's from the standard deviation), and γ is a factor that multiplies the standard deviation component. The $p-1$ for the mean represents the analytical statistical mean expected value, and the $\sqrt{2p-2}$ part represents the expected value for the χ^2 standard deviation, in the case of Gaussian noise and no mismatch between signal and template parameters as described in chapter 3. We add to these analytical parts the ones with the parameters to characterize because we know that a little mismatch between the template and the signal will

Frequency [Hz]	**H1**	**L1**
200-300	206.6, 209.1, 214.1, 218.0, 225.2, 229.5, 233.1, 243.5, 251.2, 255.2, 263.8, 282.8, 290.3, 297.2	202.0, 205.1, 208.5, 212.7, 217.9, 220.2, 227.3, 235.5, 241.1, 246.0, 253.5, 256.6, 263.2, 269.8, 273.2, 274.6, 278.4, 281.3, 283.5, 289.1, 296.3
300-400	302.5, 326.2, 332.1, 339.8, 342.9, 355.6, 358.3, 359.1, 360.8, 364.0, 367.3, 370.5, 372.9, 381.6, 384.4, 389.9, 392.3, 394.3, 399.2	301.0, 305.8, 310.8, 318.1, 321.7, 329.4, 330.9, 331.5, 333.8, 345.0, 354.3, 360.5, 364.1, 369.7, 377.1, 379.2, 387.1, 390.4
400-500	407.8, 4136, 417.5, 426.0, 438.9, 443.9, 451.3, 455.6, 463.6, 471.3, 475.2, 476.2, 477.1, 478.0, 485.8, 488.7, 489.6, 492.8, 499.1	401.6, 411.1, 428.8, 434.8, 446.0, 451.3, 457.0, 463.8, 467.5
500-600	500.9, 503.6, 507.6, 509.4, 512.2, 518.0, 526.6, 532.7, 536.0, 538.4, 541.1, 546.3, 548.3, 551.5, 559.8, 560.3, 561.6, 572.7, 576.6, 582.4, 583.2, 586.4, 595.4, 598.0	526.3, 536.0, 542.1, 558.2, 563.4, 578.5, 587.3, 590.5
600-700	605.3, 613.9, 620.1, 622.1, 626.3, 629.2, 630.6, 631.1, 636.7, 644.9, 650.0, 655.8, 660.3, 666.5, 672.5, 676.8, 692.5	607.8, 610.7, 617.8, 627.0, 638.3, 643.5, 646.5, 650.3, 653.6, 667.3, 693.0
700-800	703.1, 708.8, 711.1, 716.6, 719.2, 721.8, 725.9, 733.6, 735.2, 741.0, 744.3, 748.3, 753.0, 758.8, 766.7, 787.5	702.6, 715.9, 740.7, 747.8, 756.2, 765.6, 773.7, 798.0
800-900	808.8, 817.6, 821.5, 829.2, 836.3, 846.7, 859.8, 869.5, 885.2	802.7, 808.6, 813.5, 817.6, 821.5, 836.2, 842.7, 846.7, 848.0, 858.6, 864.6, 869.5, 878.7, 885.1, 892.6

Table 5.1: This table shows the different frequency groups in which we divided the χ^2 veto, and the frequency bands within each group. These have been selected taking into account the low significance returned by the Hough O1 search and the absence of any known instrumental lines of the detectors.

make the χ^2 values to have a dependence on significance. Another curves that we are going to try are the quadratic and cubic polynomials:

$$\bar{\chi}^2 = p - 1 + A1\ s + A2\ s^2 + A3\ s^3 + \gamma(\sqrt{2p-2} + B1\ s + B2\ s^2 + B3\ s^3), \tag{5.4}$$

where for the quadratic one we impose $A3 = B3 = 0$. The fourth curve will be a mix between a polynomial and a power law:

$$\bar{\chi}^2 = p - 1 + A1\ s + A2\ s^{A3} + \gamma(\sqrt{2p-2} + B1\ s + B2\ s^{B3}). \tag{5.5}$$

We could have used curves with more parameters, but as we will see with three parameters there is freedom enough to achieve a good fit and no more are needed.

To do the actual fitting of the curve to the points, we use the MATLAB software. This software uses a Least-Squares Fitting method to fit the curve. It also calculates some goodness of fit statistical parameters, like the SSE (Sum of Squares Due to Error) or the R^2. The SSE is defined by [53]:

$$SSE = \sum_{i=1}^{n} (y_i - \hat{y}_i)^2, \tag{5.6}$$

where y_i are the data points and $\hat{y}_i$ are the values of the curve at that points. The SST is defined as:

$$SST = \sum_{i=1}^{n} (y_i - \bar{y})^2, \tag{5.7}$$

where $\bar{y}$ is the mean of the data points. R^2 is defined as:

$$R^2 = 1 - \frac{SSE}{SST}. \tag{5.8}$$

The R^2 takes values between 0 and 1. Values closer to 1 indicate a better fit. By comparing this parameter we can see which fitting equation is the best one.

The first step is to compare the parameters (A1, A2, B1, B2) of the power law fit to check if there is a dependency on frequency. We do this by fitting a different power law curve to the sets of every 100 Hz group in table 5.1. These plots are shown in figure 5.6. It doesn't show any clear pattern, so we can say that the fitting is independent of the frequency of the bands.

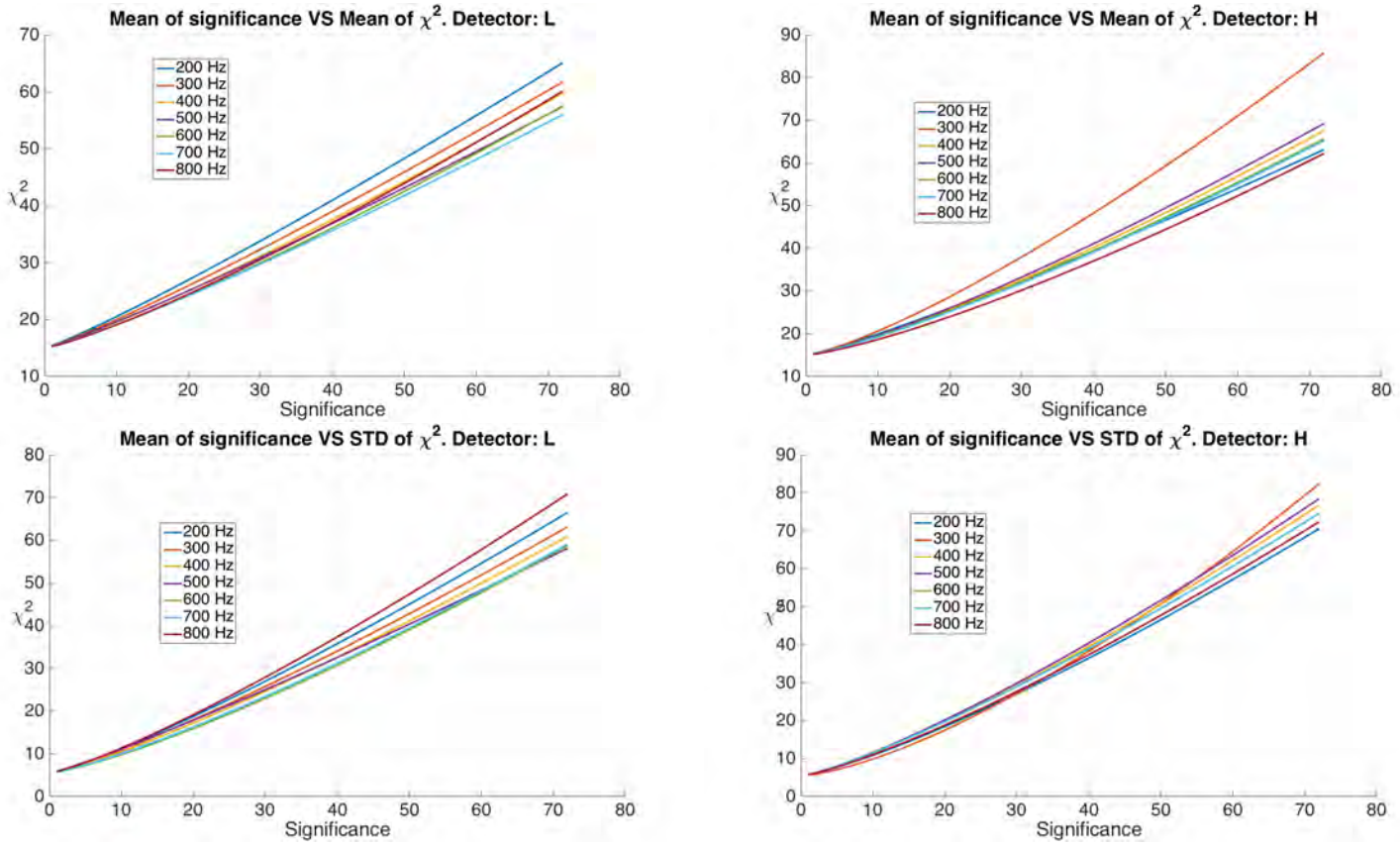

Fig. 5.6: Different fits using a power law curve for every group in table 5.1 using 1000 *points per group, with significances between* 2 *and* 70*. The upper left image shows the fit of the L1 data to the mean of the* χ^2 *values; the upper right image shows the fit of the H1 data to the mean of the* χ^2 *values; the lower left image shows the fit of the L1 data to the std of the* χ^2 *values; the lower right image shows the fit of the H1 data to the std of the* χ^2 *values.*

Now we want to check how well does the different curves of equations (5.3)-(5.5) fit the data. First, we can try to do it using the bands of only one group of 100 Hz, to see if the power law curve fits nicely to the points. Figures 5.7-5.8 show these plots. We see that the fit works well, but we want to try other curves to see if the fit can be better.

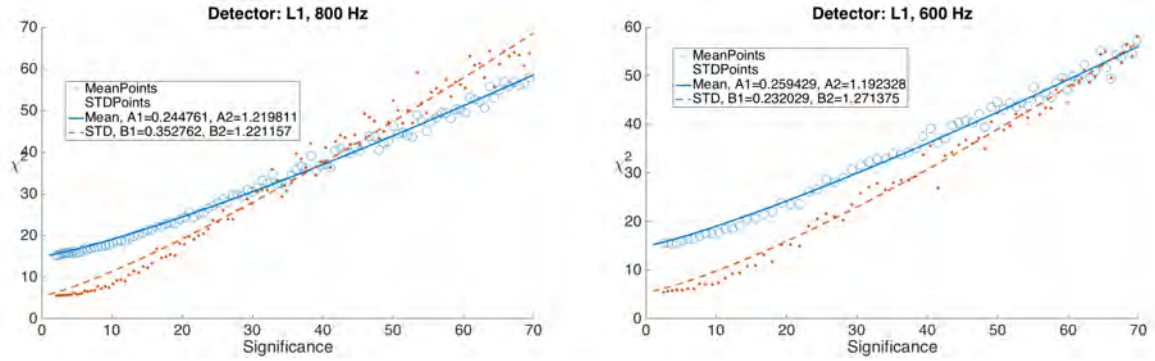

Fig. 5.7: Fits of the 800-900 *and* 600-700 *Hz groups of L1 data using* 1000 *points per group, with significances between* 2 *and* 70*. A power law curve is used.*

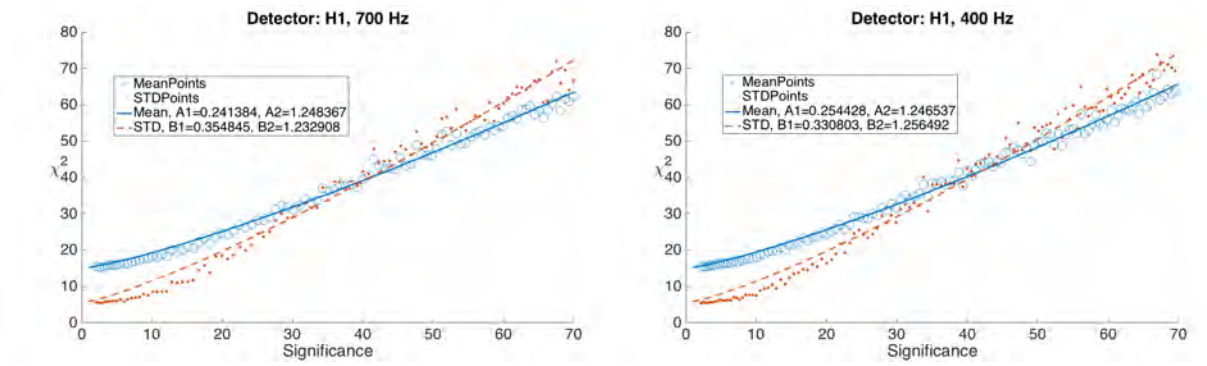

Fig. 5.8: Fits of the 700-800 *and* 400-500 *Hz groups of H1 data using* 1000 *points per group, with significances between* 2 *and* 70*. A power law curve is used.*

Since we have checked that the fitting doesn't depend on the frequency, we can join all the different bands of one detector and try to do the fitting for all of them at once. Now we will compare the different fitting curves shown in equations (5.3)-(5.5), using all the MC injections with significance between 2 and 70. For this comparison, we will make the fits only for the L1 detector. Figure 5.9 shows the different plots for the curves listed before, and table 5.2 shows the comparison between their R^2 values. One important point to have in mind is that in all these fits we have forced the value of the curves at $s = 0$. These values for the mean $(p-1)$ and for the std $(\sqrt{2p-2})$ of the χ^2 come from the analytical results assuming Gaussian noise. The fits for the curves could be better if we didn't force these values, but we are assuming that the bands analysed have no disturbances and behave like Gaussian ones.

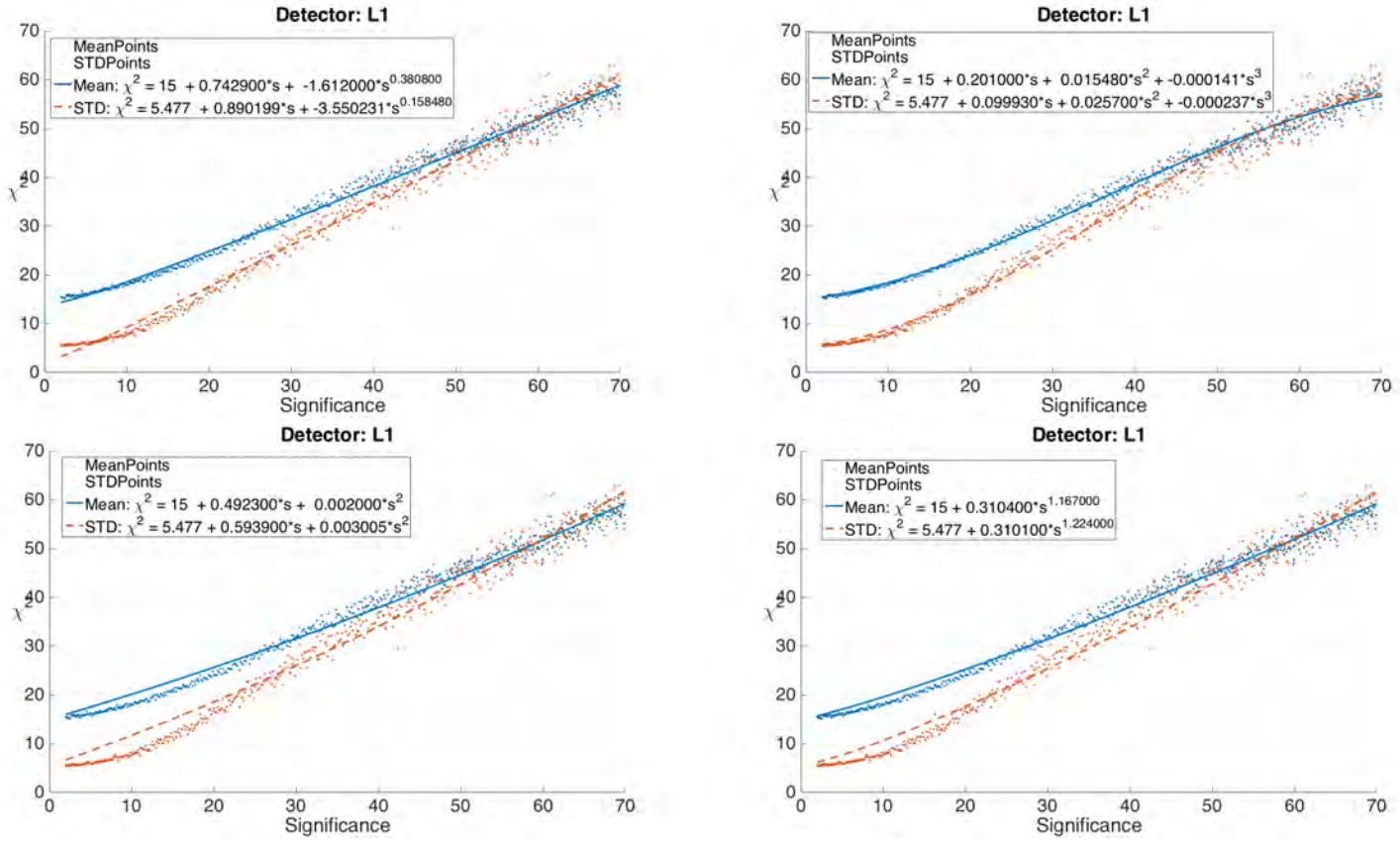

Fig. 5.9: Fits of the L1 data using 1000 *points per group, with significances between* 2 *and* 70. *Upper left panel: linear + power law curve; upper right panel: cubic polynomial curve; lower left panel: quadratic polynomial curve; lower right panel: power law curve.*

R^2	**Linear + power law**	**Cubic**	**Quadratic**	**Power law**
Mean	0.9919	0.9999	0.9871	0.9896
STD	0.9853	0.9996	0.9769	0.9805

Table 5.2: Values of the R^2 *(equation* (5.8)*) for different types of fits, using* 1000 *points per group and with significances between* 2 *and* 70.

We can clearly see that the mix between a polynomial and a power law (upper left image of figure 5.9) is the worst fit. Comparing the R^2 values for the other fits, the cubic polynomial (upper right image of figure 5.9) is the one that gives the best results. But it has two unwanted features: it uses three parameters, and we want our fitting curve to have less parameters; in addition, the third parameter is negative, which could give us problems with high values of significance (we want our curve to me monotonic in the region of low significances, because the majority of expected signals will be there). For these reasons, we discard the cubic polynomial curve.

We keep the quadratic and the power law curves. Now, we want to know if we can improve them. We can observe that the region that is more problematic to fit is the one with high

significance values. Since we are interested in having a good fit in the region between 10 and 40 of significance (the region where the real astrophysical signals should lie), we can try again to fit these two curves but using significances between 2 and 40 instead of 2 and 70. The new results are shown in figure 5.10.

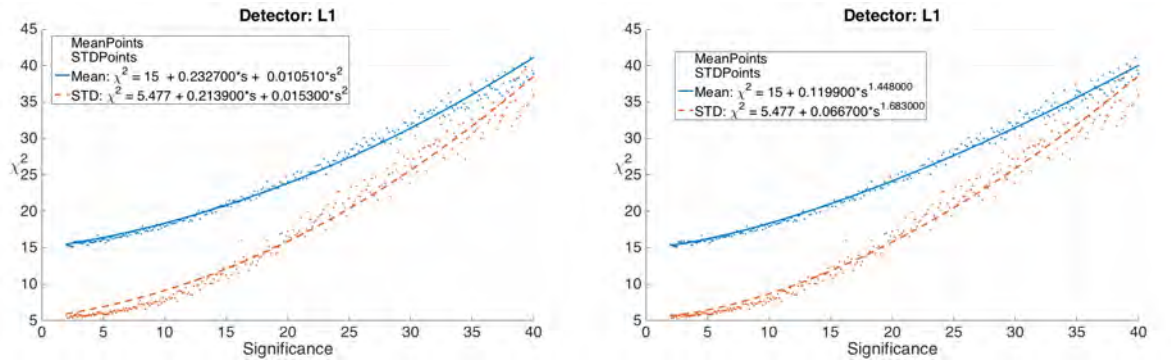

Fig. 5.10: Fit of the L1 data using 1000 *points per group, with significances between* 2 *and* 40*. A quadratic curve is used in the left image; a power law curve is used in the right image.*

R^2	**Quadratic (2 <s <40, 1000 points)**	**Power law (2 <s <40, 1000 points)**
Mean	0.9898	0.9932
STD	0.9793	0.9897

Table 5.3: Values of the R^2 (equation (5.8)) for different types of fits.

We can see that the results are much better, and table 5.3 shows the R^2 values for these new two fits, which have better values than the fits that table 5.2 showed. From now on, we will only use the power law curve, since it has the best results. We can further improve the fit by changing the number of points that every group is composed of. Instead of using 1000 points per group, we will use 2000 points to see if the fit gets better. In principle, if each group has more points, less groups should be formed, and then the fitting curve should oscillate less in the problematic zone of high significance. The new result is shown in figure 5.11.

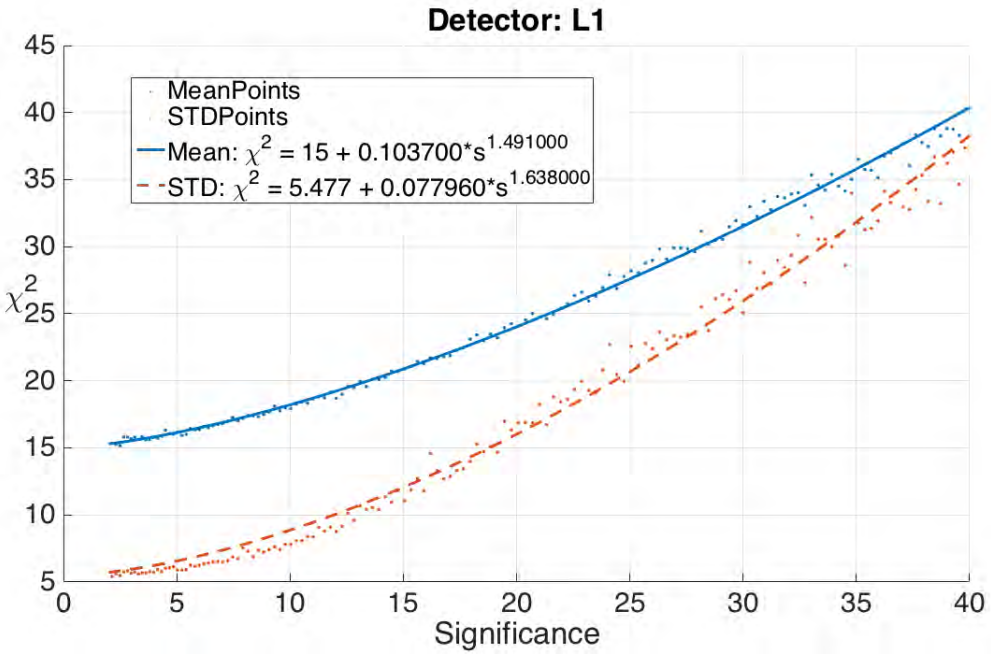

Fig. 5.11: Fit of the L1 data using 2000 *points per group, with significances between* 2 *and* 40*. A power law curve is used.*

R^2	**Power law (2 <s <40, 2000 points)**
Mean	0.9999
STD	0.9899

Table 5.4: Values of the R^2 *(equation* (5.8)*) for the power law curve using* 2000 *points per group.*

We can see in the figure and in table 5.4 that the results have improved further. From now on, we will fit between significances 2 and 40, with 2000 points per group and using a power law.

The next step is to compare the results between H1 and L1, to see if the parameters are different. In that case, the χ^2 veto in the postprocessing procedure should be different for the data of each detector. The results are shown in figures 5.12 and 5.13. Those figures show many curves with different values for the parameter γ, which is the parameter that multiplies the std component of the curve (as shown in equation (5.3)).

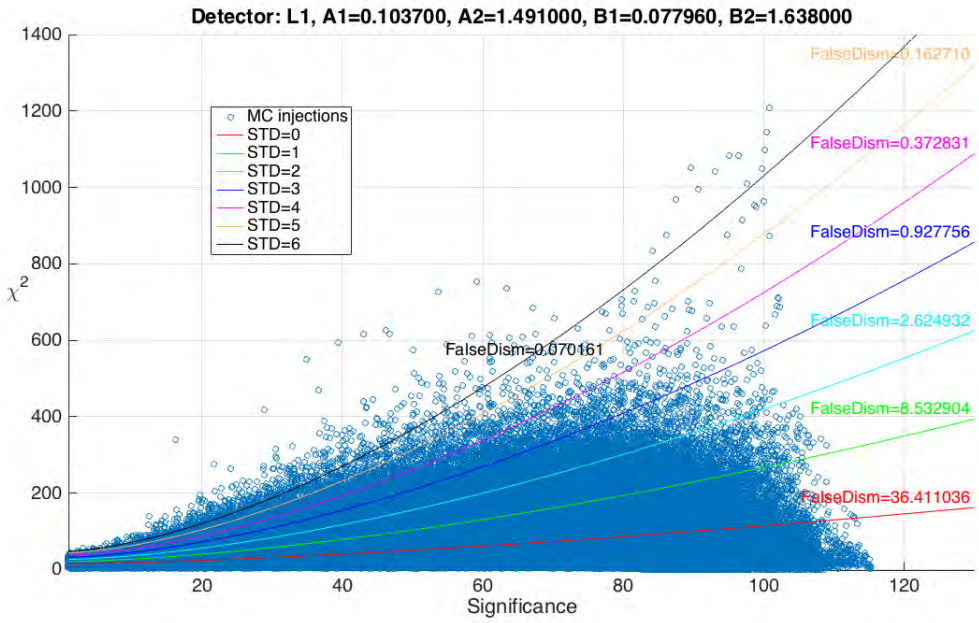

Fig. 5.12: All the Monte Carlo injections and the veto curve and parameters using data of the L1 detector. Many curves with a different value for S (equation (5.3)) are shown, with their respective false dismissal values.

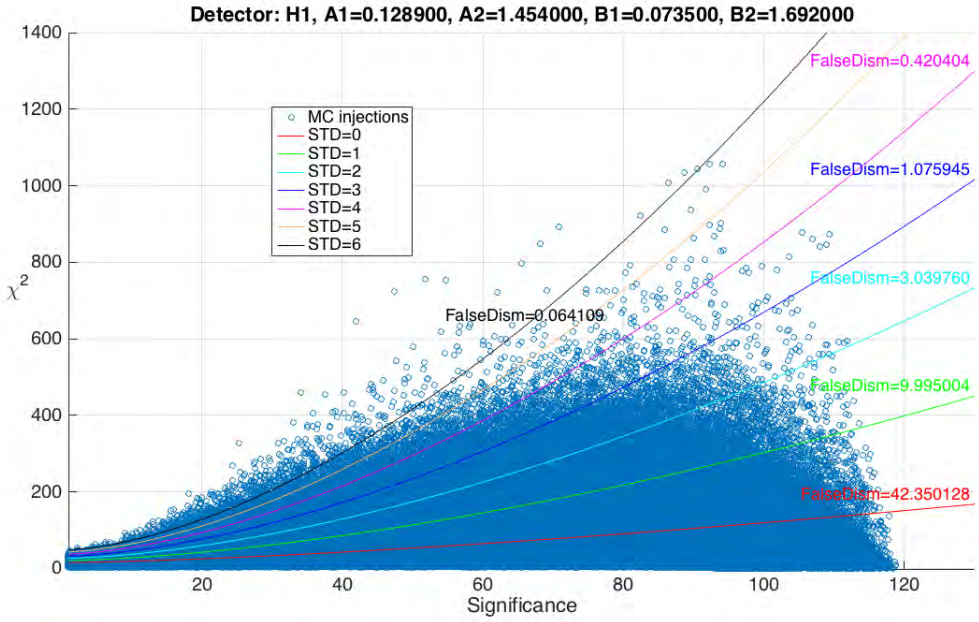

Fig. 5.13: All the Monte Carlo injections and the veto curve and parameters using data of the H1 detector. Many curves with a different value for S (equation (5.3)) are shown, with their respective false dismissal values.

Figures 5.12 and 5.13 show the results of the false dismissal value for every different curve. The false dismissal value is calculated this way: for every Monte Carlo injection (including the injections with $s > 40$), we calculate the value of the fitted curve at the same significance of the

injection, and we check if the point has a lower or a higher value than the curve. After doing this for all the Monte Carlo injections, we can divide the points which are higher than the curve by the total number of points, obtaining the false dismissal value. The false dismissal indicates how many signals we discard which in reality are true astrophysical signals. When we use the χ^2 veto in a real search, we can select the false dismissal that we want in the veto step by selecting the value for γ.

The final step is to calculate the fit curve combining the bands from both detectors. The result is shown in figure 5.14.

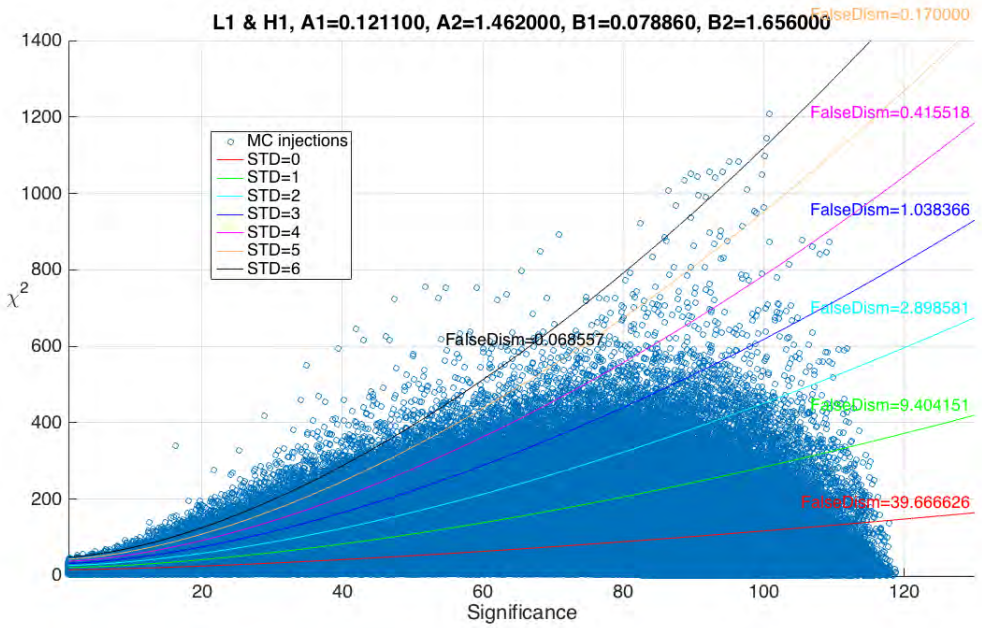

Fig. 5.14: All the Monte Carlo injections and the veto curve and parameters using data of both detectors combined. Many curves with a different value for γ (equation (5.3)) are shown, with their respective false dismissal values.

γ	**False dismissal (L1)** [%]	**False dismissal (H1)** [%]	**False dismissal (L1 & H1)** [%]
0	36.41	42.35	39.67
1	8.53	10.00	9.40
2	2.62	3.04	2.90
3	0.93	1.08	1.04
4	0.37	0.42	0.42
5	0.16	0.17	0.17
6	0.07	0.06	0.07

Table 5.5: False dismissal results for different γ values. Results are shown for L1, H1 and the combination of both.

Table 5.5 summarises the false dismissal results for every value of γ. The final parameters of the curve are summarized in table 5.6, in which we also show the veto curve obtained during Initial LIGO S5 science run. As expected, the curve has changed due to the different duration of the runs (O1 lasted about four months and S5 was approximately two years long), and because they correspond to two different detectors.

We have two options for the postprocessing procedure. If we want to use two separate fits for each detector, we will use the results from figures 5.12 and 5.13. Instead, if only one set of parameters is enough, the parameters from figure 5.14 can be used. Figure 5.15 shows a comparison between the different curves. It can be seen that the H1 & L1 curve is located between the other two.

Parameters	**A1**	**A2**	**B1**	**B2**
L1	0.1037	1.4910	0.0780	1.6380
H1	0.1289	1.4540	0.0735	1.6920
H1 & L1	0.1211	1.4620	0.0789	1.6560
S5 Results	0.3123	1.7774	0.1713	1.6214

Table 5.6: Final results of the χ^2 veto parameters for the O1 data and comparison with the results for the S5 science run [45].

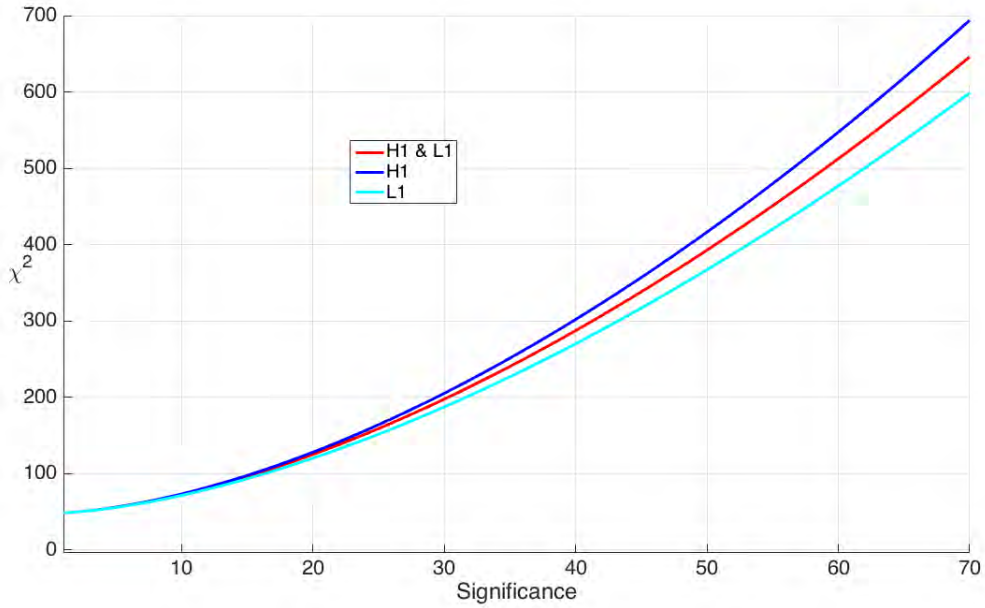

Fig. 5.15: A comparison between the final H1, L1 and H1 & L1 final curves with $\gamma = 6$.

5.3 | Example of the χ^2 veto in the O1 analysis

After calculating the parameters of the veto curve, we can test the effectivity of the χ^2 veto on O1 data. We will test the curve of the L1 detector with two different examples. First, in the frequency band of a calibration line, situated at 331.3 Hz; secondly, in the frequency band of a known pulsar hardware injection, situated at 575.163573 Hz. Figures 5.16 and 5.17 show these two examples.

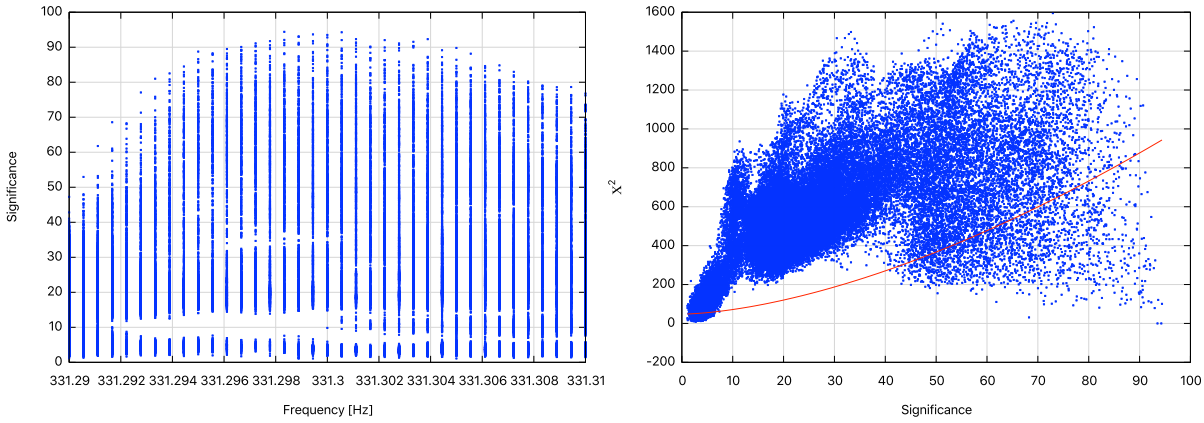

Fig. 5.16: Left image: significance versus frequency of the calibration line situated at 331.3 Hz. Right image: χ^2 versus significance of the calibration line situated at 331.3 Hz, and the veto curve with $\gamma = 6$ of the L1 detector.

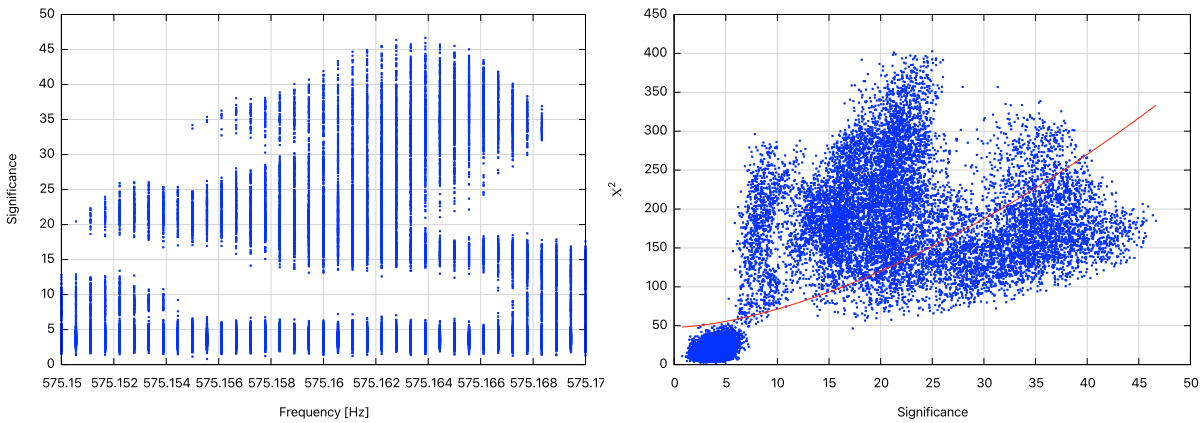

Fig. 5.17: Left image: significance versus frequency of the hardware injection situated at 575.163573 Hz. Right image: χ^2 versus significance of the hardware injection situated at 575.163573 Hz, and the veto curve with $\gamma = 6$ of the L1 detector.

It can be seen in figure 5.16 that the majority of the points are vetoed. Some points pass the veto because for some portions of the sky the Doppler effect is very small and this makes the χ^2 veto less effective, as we said in section 3.5. In figure 5.17 we can see that a lot of points pass the veto. The hardware injection is not active during all the observational time. For this reason, not all the points are in the lower-curve region. Also, for a real continuous wave signal we would have a similar plot: only one point has the exact parameters of the real signal; the

other points have some mismatch. This is why one point is the most significant one, and the other ones have lower values of s.

CHAPTER 6

CONCLUSIONS

The work of this thesis has been related to understanding continuous gravitational wave searches, and in particular the Hough all-sky search. Two different calibrations of parameters using real data have been studied:

- For the Stage 3 of the continuous waves Mock Data Challenge using data of the S6 science run, we have studied the change in the detection efficiency using different values of the peak threshold ρ_{th}. In previous theoretical studies, it was shown that the optimal value was $\rho_{th} = 1.6$, but certain assumptions were made that limited this result. We have used five different values of ρ_{th}, and we have checked that the detection efficiency is greater when we use 1.6. We also calculated the computational times of each peak threshold, but the results were a bit inconclusive due to the usage of heterogen machines. We concluded that $\rho_{th} = 1.6$ is the best value to use. One way to improve these results would be to use the exact same machine for all the different calculations. This way, we would have a more trustworthy calculation of the computational times for each ρ_{th}. We could also have done the analysis for other values of ρ_{th}, including values lower than 1.6.

- For the O1 science run, we have calibrated the parameters of the χ^2 veto curve. The χ^2 veto needs to be calibrated for every new science run, because the behaviour of the detector changes. We have tried different veto curves, and we have concluded that the best one is the power law, the same that was used in previous searches. We also have concluded that the parameters of the curve don't have a dependence on frequency, so the same parameters can be used for all the frequency bands in a search. One way to improve the parametrization of the χ^2-s curve would be to do the Monte Carlo injections in a wider and more numerous frequency band, because our results may be influenced by the bands that we have selected.

These two calibrations will help us in future searches of continuous gravitational waves.

No direct detection of a continuous wave has been made yet, but O1 analysis are still ongoing and could not be reported in this thesis. The longer observational periods and the better sensitivity of the detectors in the next science runs could make the detection of a continuous wave signal a real possibility. The O2 science run will approximately begin at the end of 2016, and will last approximately four months.

BIBLIOGRAPHY

[1] **Albert Einstein**. *On the Electrodynamics of Moving Bodies*. Annalen Phys. 17 (10): 891–921. (1905)

[2] **Albert Einstein**. *The foundation of the general theory of relativity*. Annalen Phys. 49:769-822. (1916)

[3] **Albert Einstein**. *Approximative Integration of the Field Equations of Gravitation*. Königlich Preußische Akademie der Wissenschaften (Berlin). Sitzungsberichte, 688-696. (1916)

[4] **R.A. Hulse and J.H. Taylor**. *Discovery of a pulsar in a binary system*. Astrophys. J., 195: L51-L53 (1975)

[5] **LIGO Scientific Collaboration**. *Observation of Gravitational Waves from a Binary Black Hole Merger*. Phys. Rev. Lett. 116, 061102 (2016)

[6] **Misner C.W., Thorne K.S. and Wheeler J.A.** *Gravitation*. Published by W. H. Freeman and company (1973)

[7] **Michele Maggiore**. *Gravitational Waves. Volume 1. Theory and Experiments*. Edited by Oxford University Press. ISBN: 9780198570745 (2007)

[8] **Sun Fact Sheet**. http://nssdc.gsfc.nasa.gov/planetary/factsheet/sunfact.html

[9] **Odylio Denys Aguiar**. *Past, present and future of the Resonant-Mass gravitational wave detectors*. Res. Astron. Astrophys. 11 1 (2011)

[10] **F.A.E. Pirani**. Acta Phys. Pol. Volume 15, Page 389 (1956)

[11] **Rainer Weiss**. *Electronically coupled broadband gravitational antenna*. Quarterly Progress Report, Research Laboratory of Electronics (MIT) No. 105, p.54. (1972)

[12] **LIGO Scientific Collaboration website**. http://www.ligo.org/

[13] **VIRGO website**. http://public.virgo-gw.eu/language/en/

[14] **GEO website**. http://www.geo600.org/

[15] **KAGRA website**. http://gwcenter.icrr.u-tokyo.ac.jp/en/

[16] **Einstein Telescope**. http://www.et-gw.eu/

[17] **International Pulsar Timing Array**. http://www.ipta4gw.org/

[18] **eLISA**. https://www.elisascience.org/

[19] **Saulson, P.R.**. *If light waves are stretched by gravitational waves, how can we use light as a ruler to detect gravitational waves?*. Am. J. Phys. 65, 501. (1997)

[20] **LIGO Scientific Collaboration**. *Characterization of transient noise in Advanced LIGO relevant to gravitational wave signal GW150914*. Classical and Quantum Gravity, Volume 33, Number 13 (2016)

[21] **James M. Lattimer**. *The Nuclear Equation of State and Neutron Star Masses*. Annual Review of Nuclear and Particle Science. Vol. 62: 485-515 (2012)

[22] **A. Hewish, S. J. Bell, J. D. H. Pilkington, P. F. Scott and R. A. Collins**. *Observation of a Rapidly Pulsating Radio Source*. Nature 217, 709-713 (1968)

[23] **Manchester, R. N., Hobbs, G. B., Teoh, A. and Hobbs, M.**. *The Australia Telescope National Facility Pulsar Catalogue*. The Astronomical Journal, Volume 129, Issue 4, pp. 1993-2006 (2005) http://www.atnf.csiro.au/people/pulsar/psrcat/

[24] **Bradley Carroll, Dale Ostlie**. *An introduction to modern astrophysics*. Pearson education. ISBN: 0-201-54730-9 (1995)

[25] **R. F. Archibald et alii**. *A High braking index for a pulsar*. The Astrophysical Journal Letters, Volume 819, Number 1 (2016)

[26] **C. J. Horowitz and Kai Kadau**. *Breaking Strain of Neutron Star Crust and Gravitational Waves*. Phys. Rev. Lett. 102, 191102 (2009)

[27] **Nathan K. Johnson-McDaniel and Benjamin J. Owen**. *Maximum elastic deformations of relativistic stars*. Phys. Rev. D 88, 044004 (2013)

[28] **LIGO Scientific Collaboration**. *Beating the spin-down limit on gravitational wave emission form the crab pulsar*. The Astrophysical Journal, 683: L45–L49, (2008)

[29] **Piotr Jaranowski, Andrzej Królak, and Bernard F. Schutz**. *Data analysis of gravitational-wave signals from spinning neutron stars: The signal and its detection*. Phys. Rev. D 58, 063001 (1998)

[30] **Hough**. P.V.C. U.S. Patent, (3069654), (1962)

[31] **Duda, R. O. and P. E. Hart**. *Use of the Hough Transformation to Detect Lines and Curves in Pictures*. Comm. ACM, Vol. 15, pp. 11-15 (1972)

[32] **Hart, P. E.**. *How the Hough Transform was Invented*. IEEE Signal Processing Magazine, Vol 26, Issue 6, pp 18-22 (2009)

[33] **B. Krishnan, A. Sintes, M. Pap, B. Schutz, S. Frasca, C. Palomba**. *Hough transform search for continuous gravitational waves*. Physical Review D, Volume 70, 082001 (2004)

[34] **Edited by Ciufolini I., Gorini V., Moschella U. and Fre P.**. *Gravitational Waves*. IOP. ISBN: 0-7503-0741-2 (2001)

[35] **B.S. Sathyaprakash and Bernard F. Schutz**. *Physics, Astrophysics and Cosmology with Gravitational Waves*. (2009) http://relativity.livingreviews.org/Articles/lrr-2009-2/fulltext.html

[36] **Reinhard Prix for the LIGO Scientic Collaboration**. *Gravitational Waves from Spinning Neutron Stars*. In "Neutron Stars and Pulsars", ed. W. Becker, Springer-Verlag, p 651. LIGO-P060039-v3 (2009)

[37] **Simin Mahmoodifar, Tod Strohmayer**. *Upper bounds on r-mode amplitudes from observations of low-mass X-ray binary neutron stars*. The Astrophysical Journal, Volume 773, Issue 2, article id. 140, 10 pp. (2013)

[38] **D. I. Jones, N. Andersson**. *Gravitational waves from freely precessing neutron stars*. Oxford Journals Volume 331 Issue 1 203-220. (2002)

[39] **Sinead Walsh et alii**. *A comparison of methods for the detection of gravitational waves from unknown neutron stars*. (2016)

[40] **HTCondor**. https://research.cs.wisc.edu/htcondor/

[41] **G. Heinzel, A. Rudiger and R. Schilling** *Spectrum and spectral density estimation by the Discrete Fourier transform (DFT), including a comprehensive list of window functions and some new flat-top windows*. (2002) http://pubman.mpdl.mpg.de/pubman/faces/viewItemOverviewPage.jsp?itemId=escidoc:152164

[42] **Tukey window**. http://es.mathworks.com/help/signal/ref/tukeywin.html

[43] **Llucia Sancho de la Jordana and Alicia M. Sintes**. *A χ^2 veto for continuous gravitational wave searches*. Classical and Quantum Gravity, Volume 25, Number 18 (2008)

[44] **P. Jaranowski, A. Krolak, and B. F. Schutz**. *Data analysis of gravitational-wave signals from spinning neutron stars: the signal and its detection*. Phys. Rev. D58 063001 (1998)

[45] **LIGO Scientific Collaboration**. *Application of a Hough search for continuous gravitational waves on data from the fifth LIGO science run*. Classical and Quantum Gravity, Volume 31, Number 8 (2014)

[46] **LIGO Scientific Collaboration**. *All-sky search for periodic gravitational waves in LIGO S4 data*. Phys. Rev. D 77, 022001 (2008)

[47] **Soumya D. Mohanty**. *Robust test for detecting non-stationarity in data from gravitational wave detectors*. Phys. Rev. D 61, 122002 (2002)

[48] **Jolien D. E. Creighton**. *Data analysis strategies for the detection of gravitational waves in non-Gaussian noise*. Phys. Rev. D 60, 021101(R) (1999)

[49] **Alicia Sintes, Badri Krishnan**. *MCInjectHoughMulti.c*. http://software.ligo.org/docs/lalsuite/lalapps/_m_c_inject_hough_multi_8c_source.html

[50] **Badri Krishnan, Alicia Sintes**. *DriveHoughMulti.c*. http://software.ligo.org/docs/lalsuite/lalapps/_drive_hough_multi_8c_source.html

[51] **LALApps Documentation**. http://software.ligo.org/docs/lalsuite/lalsuite/

[52] **Pia Astone, Alberto Colla, Sabrina D'Antonio, Sergio Frasca, Cristiano Palomba**. *Method for all-sky searches of continuous gravitational wave signals using the frequency-Hough transform*. Phys. Rev. D 90, 042002 (2014)

[53] **Evaluating Goodness of Fit**. http://es.mathworks.com/help/curvefit/evaluating-goodness-of-fit.html